High-Strain Actuation of Lead-Free Perovskites: Compositional Effects, Phenomenology and Mechanism

by

Andrey N. Soukhojak

Submitted to the Department of Materials Science and Engineering

in Partial Fulfillment of the requirements for the Degree of

Doctor of Philosophy in Ceramics

at the

MASSACHUSETTS INSTITUTE OF TECHNOLOGY

September 2002

Signature of Author .....
Department of Materials Science and Engineering
August 23, 2002

Certified by..... ....
Yet-Ming Chiang
Kyocera Professor of Ceramics
Thesis Supervisor

Accepted by .....
Harry L. Tuller
Professor of Ceramics and Electronic Materials
Chair, Departmental Committee on Graduate Students

High-Strain Actuation of Lead-Free Perovskites: Compositional Effects, Phenomenology and Mechanism

by

Andrey N. Soukhojak

Submitted to the Department of Materials Science and Engineering on August 23, 2002 in partial fulfillment of the requirements for the Degree of Doctor of Philosophy in Ceramics

ABSTACT

An experimental study was carried out to map the compositional dependence of electromechanical behavior and ferroelectric phase stability in the barium, zirconium-codoped sodium bismuth titanate (BNBZT) system for barium concentrations up to 18 mol.% and zirconium concentrations up to 4 mol.%. A number of polycrystalline BNBZT samples has been electromechanically tested under applied electric fields of different frequencies (0.2-47 Hz).

A novel model of electromechanical response capable of describing both dynamic and static hysteresis for pure and mixed cases of ferroelectric, antiferroelectric, ferroelastic and paraelectric behavior has been developed. Major electromechanical properties of polycrystalline BNBZT have been identified and compositionally mapped. The peak of electromechanical response (d_{33} = 400 pC/N) has been found at the composition $(Bi_{1/2}Na_{1/2})_{0.93}Ba_{0.07}Zr_{0.02}Ti_{0.98}O_3$. The compositional dependence of ferroelectric phase stability has been mapped by means of a Landau type free energy expansion. A nanodomain relaxation mechanism of frequency dependent electromechanical response of BNBZT has been suggested and is supported by optical and transmission electron microscopy.

Thesis Supervisor: Yet-Ming Chiang
Title: Kyocera Professor of Ceramics

TABLE OF CONTENTS

ACKNOWLEDGMENTS

The author wishes to thank all people who helped him through his time at MIT, especially Yet-Ming Chiang, Greg Farrey, Sossity Sheets, Haifeng Wang, Toni Centorino, Fred Wilson, Hong Cai, Ben Nunes, Garry Maskaly, Pimpa Limthongkul and Doug Moorehead.

I dedicate this work in loving memory to my mother, Valeria V. Soukhojak (1941-1995)

C h a p t e r 1

INTRODUCTION

Electromechanically active materials, i.e. materials that convert a large portion of electrical energy directly into mechanical energy and vice versa, constitute key components in many devices, such as: sonar and medical ultrasound transducers, electromechanical positioners, vibration dampeners, ultrasonic motors, MEMS, etc. The use of these devices is critical in many applications, especially in aero-astronautical and naval ones. Electromechanically active materials can be considered as a class in the family of *smart materials*, which in general can sense external conditions and with the help of external circuits generate a necessary response. Electromechanically active materials are usually categorized into *piezoelectrics* (linear strain S vs. electric field E response: $S = d\,E$) and *electrostrictors* (quadratic strain vs. electric field response: $S = M\,E^2$).

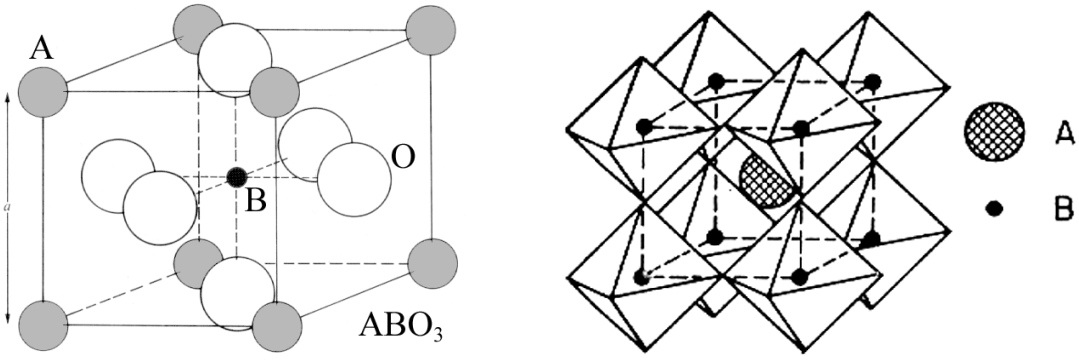

Figure 1.1. Alternative aspects of perovskite structure.

Ceramic electromechanically active materials, in particular piezoelectrics with *perovskite* structure $A^{II}B^{IV}O_3$ (Fig. 1.1), e.g. barium titanate $BaTiO_3$, have been widely used commercially since late 1940's due to their thermal stability, water resistance and good mechanical properties. Relatively recently, lead containing B-site *relaxors* with perovskite structure, e.g. $Pb(Mg_{1/3}Nb_{2/3})O_3 - PbTiO_3$ (PMN-PT) and $Pb(Zn_{1/3}Nb_{2/3})O_3 - PbTiO_3$ (PZN-PT) have attracted a lot of theoretical and practical attention because of their high-strain capability (up to 1.7%) and ease of their single crystals growth by the flux method [S.-E. Park and T.R. Shrout, *J. Appl. Phys.*, **82** [4] 1804-1811 (1997)]. The mechanism allowing these crystals to develop field-induced strains >1%

is not completely understood, but is usually associated with the presence of *polar nanoregions* (*microdomains*) that are formed due to a partial order of heterovalent cations in the B-sublattice [L.E. Cross. *Ferroelectrics*, **76** 241-67 (1997)].

It should be noted that all commercially used compositions of electromechanically active perovskites contain lead as a major component. The neurotoxicity, kidney toxicity and the damaging effects of lead on reproductive health, leading to sterility have long been recognized. Most recently, lead exposure has been linked to the development of Alzheimer's disease. Lead in the environment from consumer products and processing waste poses the greatest threat to the developing nervous system in young children. Exposure to lead is known to cause decreased intelligence, reading disabilities, and motor skill deficits in children [D. Juberg et al., "Lead and Human Health," *American Council on Science and Health*, New York, December 1997]. The toxicity of lead oxide and its high vapor pressure during processing has resulted in an increasing demand for alternative materials with reduced toxicity.

Research of lead-free perovskite structure single crystals in the $(Na_{1/2}Bi_{1/2})TiO_3 - BaTiO_3$ (NBT-BT) system (A-site relaxor) have recently shown promising electromechanical properties, such as strain up to 0.85% [Y.-M. Chiang *et al.*, *Appl. Phys. Lett.*, **73** 3683-5 (1998)]. This result shows that lead is not required to achieve high strain and that the A-site cation disorder can play a role similar to the B-site cation disorder in high-strain lead relaxors. Further development of lead-free compositions [S.A. Sheets *et al.*, *J. Appl. Phys.*, **90** 5287-95 (2001)] has revealed that single crystals in the $(Bi_{1/2}Na_{1/2})_{1-x}Ba_xZr_yTi_{1-y}O_3$ (BNBZT) have exceptionally high electrostrictive properties. Rhombohedral phase crystals exhibit piezoelectric strain coefficient d_{33} up to 1180 pC/N and strains of $S_3 = 0.3\%$ before electrical breakdown, while tetragonal phase crystals exhibit d_{33} up to 2000 pC/N and S_3 up to 0.45% strain. These crystals show the highest electrostrictive strains yet reported for an inorganic compound.

The goal of this work is a systematic study of electromechanical behavior of polycrystalline samples in the BNBZT system, analysis of compositional dependence of the electromechanical properties and understanding of mechanisms of high field-induced strain and the performance determining factors. Achieving this goal is very instrumental for efficient design of new as well as optimization of the existing smart materials.

Origin of Ferroic Phase Transitions

Historically, it appears that all ceramic electromechanically active materials undergo or are related to ferroelectric phase transitions. This fact has fundamental importance and I want to discuss the origin of ferroelectric phase transitions in the general context of ferroic phase transitions.

Ferroic phase transition is a general concept comprising the *ferromagnetic*, *ferroelectric* and *ferroelastic* phase transitions. As a result of these transitions, a material with initially higher symmetry loses some of its symmetry elements upon cooling due to the discontinuous appearance (1^{st} order transition) or continuous development (2^{nd} order transition) of a macroscopic *ferroic order parameter* of vectorial or tensorial nature: magnetization, polarization or strain. A necessary condition for the existence of a ferroic phase is the presence of at least two energetically equal orientations/configurations of the ferroic order parameter that the high symmetry phase can assume during the ferroic phase transition (multi-stability condition). The ferroic material below the critical (Curie) temperature T_C contains one or many macroscopic regions (domains). Within each domain, the orientation/configuration of the order parameter remains constant; between domains, the direction of the order parameter changes over a narrow region (domain wall).

A ferroic transition exists due to *long-range interaction* between atomic level analogs of the macroscopic order parameter (*generalized ferroic displacements*), i.e. atomic spin, atomic dipole and atomic displacement, describing a state of an atom, atomic group or a whole unit cell. This interaction is expressed as the last term in the Hamiltonian [M.E. Lines and A.M. Glass. "Principles and Applications of Ferroelectrics and Related Materials". *Oxford Univ. Press*, 1977]:

$$H = \sum_{l} \{\tfrac{1}{2}\pi_l^2 + V(\xi_l)\} - \tfrac{1}{2}\sum_{l}\sum_{l'} J_{ll'}\xi_l\xi_{l'} \qquad (1.1)$$

where l and l' are the cell numbers, π generalized momentum in kinetic energy term, ξ generalized ferroic displacement (spin, atomic dipole moment, atomic displacement), V potential energy, $J_{ll'}$ bilinear interaction coefficient. Above the critical temperature, long-range interaction is completely disrupted by thermal fluctuations, so that no macroscopic order parameter is stable and the material possesses high symmetry, i.e. exists in the *para-phase*. Below the transition temperature, the long-range interaction overcomes the thermal agitation. As a result, the atomic

spins, dipoles or displacements arrange in an ordered fashion over a macroscopic scale—material exists in a *ferro-phase*.

The perovskite structure allows both polar (ferroelectric-ferroelastic) and non-polar (purely ferroelastic) distortion mechanisms. The possibility of distortions originate from the fact that no three ions can satisfy the geometric requirement for an ideally packed structure expressed by the following equation, which is also the definition of the Goldschmidt tolerance factor *t* [V. M. Goldschmidt, *Oslo I. Mat.-Natur.*, **2** 7-12 (1926)]:

$$t = \frac{(R_A + R_O)}{\sqrt{2}(R_B + R_O)} = 1 \qquad (1.2)$$

where, R_A is the A-site cation radius, R_B is the B-site cation radius, and R_O is the oxygen anion radius (or a different anion radius). Deviations from $t = 1$ represent distortions from the ideal cubic perovskite structure. The stability range is approximately $0.75 < t < 1.06$ [R. D. Shannon, *Acta Cryst.* **A32** 751-67 (1976)]. Dependence of possible distortion of oxide perovskites on the cation sizes can be represented on the R_A-R_B map (Fig. 1.2) [Kassan-Ogly and Naish, *Acta Cryst.* **B42** 297 (1986)].

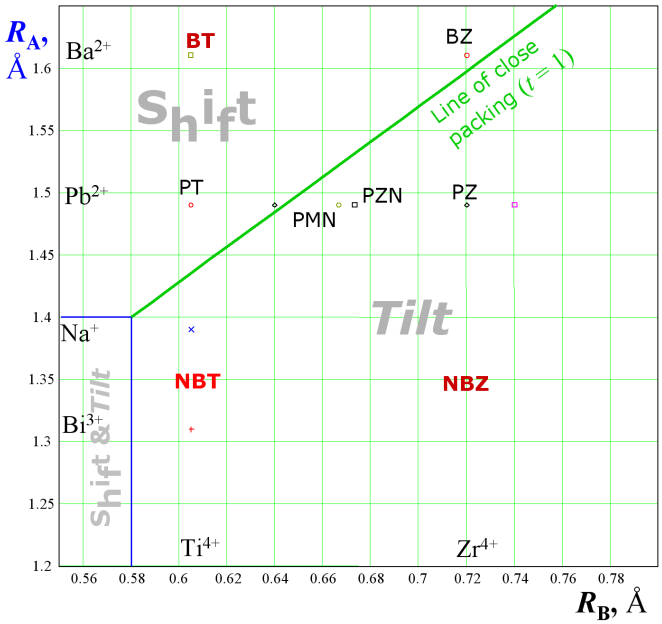

Figure 1.2. R_A-R_B map of oxide perovskites with some examples.

The simplest polar mechanism is the shift of a small B cation inside the oxygen octahedral cage along [001], [110] or [111] directions. In most of the real perovskites all ions shift from their positions in the high symmetry phase during the phase transition. The simplest non-polar mechanism is a tilt of oxygen octahedra in order to squeeze a small A cation (there are 22 possible octahedral tilt systems in perovskites, systematized by Glazer [G. Burns and A.M. Glazer. "Space Groups for Solid State Scientists". *Academic Press* (1990)]). Both polar and non-polar distortions can coexist, producing two non-zero order parameters—ferroelectric and ferroelastic.

Relaxor Ferroelectrics and Their Features

Relaxor behavior has been studied extensively in lead-based complex perovskite systems [I.W. Chen, *J. Phys. Chem. Solids*, **61** 197-208 (2000)]. Relaxor ferroelectrics are distinguished from "normal" ferroelectrics by the presence of certain key characteristics. The most distinctive characteristic is a diffuse and frequency-dependent maximum in permittivity (also known as dielectric constant) ε (T_m) and dielectric loss tan δ with temperature (Fig. 1.3). The temperatures of the permittivity and loss maxima increase with increasing frequency. Below the maximum, ε and tan δ exhibit large frequency dispersion, with ε decreasing and tan δ increasing with increasing frequency. For temperatures above the maximum, frequency dispersion is negligible.

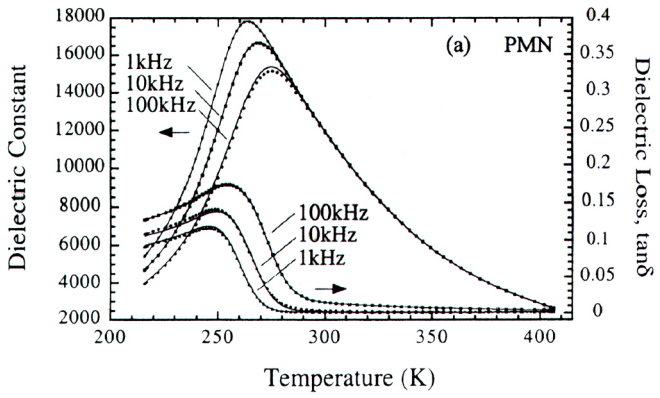

Figure 1.3. $Pb(Mg_{1/3}Nb_{2/3})O_3$: Typical Temperature Dependence of Permittivity and Dielectric Loss in Relaxor Ferroelectrics [H.T. Lin et al., *J. Am. Ceram. Soc.* **82** (10) 2698-2704 (1999)]

For the B-site cubic complex perovskite relaxor, $Pb(Mg_{1/3}Nb_{2/3})O_3$ (PMN), it is observed that T_m does *not* represent a macroscopic phase transition between ferroelectric and electrostrictive states. Rather, remanent polarization P_r exhibits a gradual decay as temperature increases with the temperature of depolarization T_d occurring well below T_m.

The characteristic relaxor dielectric behavior in B-site complex perovskites (such as PMN) is attributed to the presence of ordered nanodomains with short correlation length. These nanodomains form as the disordered B-site structure induces A-site displacement (ΔPb^{+2}), giving rise to nano-scale compositional fluctuations [Z.G. Ye, *Key Eng. Mater.*, **155-156** 81-122 (1998)].

It has been shown that cation disorder can cause the relaxor behavior [N. Setter and L.E. Cross. *J. Appl. Phys*. **51** [8] 4356-60 (1980)]. Fig. 1.4 shows how cation ordering in $Pb(Sc_{1/2}Ta_{1/2})O_3$ (PST), which occurs spontaneously during annealing, changes the dielectric response from relaxor type to classical ferroelectric one.

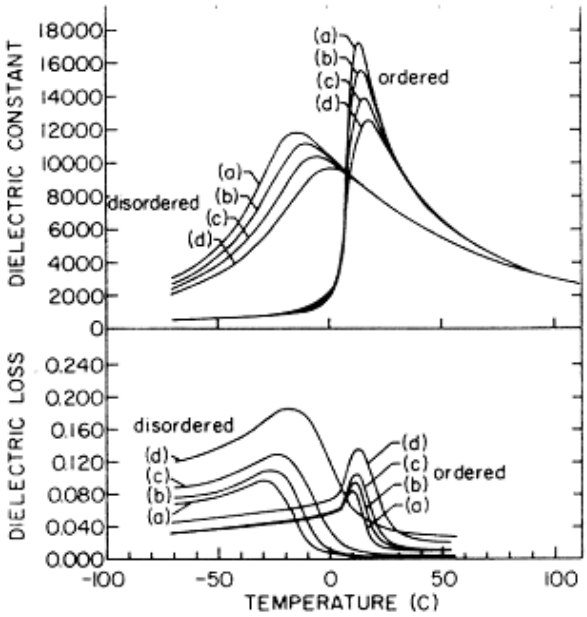

Figure 1.4. Temperature dependence of dielectric properties of 30% ordered (disordered) and 80% ordered (ordered) $Pb(Sc_{1/2}Ta_{1/2})O_3$ at 1-1000 kHz.

Range of Critical Phenomena

As mentioned above, upon cooling through the critical temperature, a ferroic material lowers its symmetry. It is generally recognized that nature prefers continuity. This is the case with the ferroic phase transitions. Around the critical temperature, the state of the material is different

from both para- and ferro-phases and combines the features of both. The thermal fluctuations still prevent the formation of macroscopic domains, but they are already small enough to allow the temporary existence of microscopic regions with a net non-zero ferroic order parameter. Therefore, we can consider a ferroic phase transition as the gradual growth of the size and lifetime of the ferroic domains from the atomic scale (where the concept of domain loses its meaning) and ~10^{-13} s to macro-scale and geological time scales. This transition occurs in a temperature range (*Ginsburg range*) where the thermal fluctuations substantially affect the material state and the classical Landau free energy expansion fails to correctly predict some of the properties.

Classically, the para-phase approaching the ferroic phase transition temperature T_C exhibits Curie-Weiss behavior—the susceptibility diverges as $C/(T–T_C)$, where C is the Curie constant.

Factors Disrupting Long-Range Interaction

Beside thermal fluctuations, one can think of structural/compositional fluctuations or defects that play a similar role in disrupting long-range interaction ($J_{ll?}$ in Eqn. 1.1). For example, (1) the antiphase boundaries or disordered matrix that separate ordered regions in a chemically ordered complex compound or (2) Kanzig domains of spinodally decomposed material obviously disrupt the periodicity of ferroic generalized displacements. These structural/compositional fluctuations can limit the size of the ferroic domains by their own characteristic size (possibly several nanometers). However when pushed to the limit, full disorder with no ordered regions creates a mean-field situation with atomic scale of the fluctuations and classical behavior of the properties (i.e. either para-phase or ferro-phase behavior). Fully ordered state will also render a classical behavior. For example, complex lead perovskites show relaxor behavior only if coherence length of the B-site cation ordering is about 10 nm [C.A. Randall et al. *Ferroelectrics Letters*, **11** [5] 103-6 (1990)]. When this length is either >100 nm or close to atomic size, these materials exhibit classical ferroelectric and antiferroelectric behavior.

Another disrupting factor is the particle surface. It is well known that when the particle size/film thickness decreases, the ferromagnetic and ferroelectric properties vanish: the hysteresis loop closes down to a curve characteristic for paramagnetic/paraelectric. Normally a ferromagnetic material when dispersed into superfine particles exhibits *superparamagnetic* properties, such as no

remanent magnetization and exponential relaxation of the field-induced magnetization over time. L.E. Cross coined the term s*uperparaelectricity* (ferroelectric analog of superparamagnetism) to explain broad frequency dependent maximum of permittivity vs. temperature and no remanent polarization, e.g. lead relaxor systems [L.E. Cross. *Ferroelectrics*, **76** 241-67 (1997)].

Coupling of Systems

The main function of electromechanically active materials can be easily analyzed with the use of the concept of a material *system* [T.D. Ikeda, "Fundamentals of piezoelectricity", *Oxford University Press* (1990)]. Two systems in electromechanically active materials that are of interest are the electric system (system of mobile charges) and the elastic system (system of attracting/repulsing atoms). Obviously, the systems interact because in ionic crystals atoms are charged. The interaction is manifested as non-diagonal terms in the *matrix of compliances,* connecting fields (electric field vector *E* and stress tensor *T*) and responses (electric displacement vector *D* and strain tensor *S*) linearly (in the simplest case):

$$\begin{bmatrix} D \\ S \end{bmatrix} = \begin{bmatrix} \varepsilon^T & d \\ d & s^E \end{bmatrix} \begin{bmatrix} E & T \end{bmatrix} \tag{1.3}$$

I do not consider the electrostrictor response separately, because an electrostrictive material under bias field can be used as a piezoelectric. Performance of an electromechanically active materials is measured as a piezoelectric strain coefficient *d* (3^{rd} rank tensor) which can be expressed in terms of principal compliances and coupling coefficients *k*, e.g. for longitudinal (subscript "33") actuation we have

$$d_{33} = k_{33}\sqrt{\varepsilon_{33}^T s_{33}^E} \tag{1.4}$$

Equation 1.4 shows that there are at least three parameters that should be maximized to obtain the best piezoelectric response: principal compliances of the electric and elastic systems and coupling between the systems. The coupling coefficient for perovskite piezoelectrics usually varies between 0.2 and 0.9 whereas principal compliances can vary by orders of magnitude because of the anomaly around the critical temperature.

Structure of NBT and Its Phase Transitions

Sodium bismuth titanate was selected as the base composition in this work due to its promise as the best lead-free piezoelectric. Unlike lead-containing compositions, it can easily be grown in single crystal form because it melts congruently. It is also stiffer. Higher stiffness produces higher actuation authority—a characteristic required for high-force actuation.

Ferroelectricity in complex perovskite sodium bismuth titanate $(Na_{1/2}Bi_{1/2})TiO_3$ (NBT) was discovered by Smolenskii *et al.* [G.A. Smolenskii et al. *Sov. Phys. - Solid State* **2** [11] 2651-2654 (1961)]. Virtually all publications on NBT stress the peculiar nature of its phase transitions as a possible cause of the broad frequency dependent permittivity vs. temperature maximum, which is not directly related to any single phase transition. Summarizing previously published data, Siny *et al.* point out three reversible phase transitions in solid NBT that occur upon cooling: (1) cubic to tetragonal ferroelastic phase at ~520°C, (2) tetragonal ferroelastic to rhombohedral ferroelastic phase at ~260-300°C, and (3) rhombohedral ferroelastic to rhombohedral ferroelectric phase at ~200°C [I.G. Siny, *Phys. Rev.* **B51** 5659-65 (1995)].

Previous studies have resulted in conflicting views regarding the presence of a superlattice in NBT and its origin. In general, there are three possible mechanisms of superlattice formation in complex perovskites: (1) chemical ordering of the species; (2) antiparallel displacement of ions; (3) octahedral tilt. The rocksalt type ordering of sodium and bismuth cations on the A-sublattice seems reasonable due to different charges of the cations and simulated XRD pattern for this type of ordering shows noticeable superlattice peaks. However, powder XRD does not reveal any traces of the superlattice. In undoped NBT, Park *et al.* [S.-E. Park, *J. Am. Ceram. Soc.* **77** [10] 2641-47 (1994)] have observed weak superlattice single crystal XRD reflections of (h+? k+? l+?) type and attributed them to the chemical ordering of Na^+ and Bi^{3+} ions, whereas Vakhrushev *et al.* (Fig. 1.5) have shown a hysteretic sequence of superlattices on heating/cooling and attributed it to different octahedral tilts. Vakhrushev *et al.* contend that NBT has three structural instability points in the Brillouin zone: two non-polar M_3 and R_{25}, responsible for the tilt superlattices (single-axis in-phase tilt, $a^0a^0c^+$ in Glazer notation, and three-axis equivalent anti-phase tilt, $a^-a^-a^-$ in Glazer notation, respectively) and one polar Γ_{15}, responsible for spontaneous polarization.

The most recent neutron diffraction studies of NBT [G.O. Jones and P.A. Thomas, *Acta Cryst.* **B58**, 168-178 (2002)] have revealed the following sequence of phase transitions during cooling: cubic (above 540°C), tetragonal (400-500°C), rhombohedral (below 255°C) with large coexistence temperature regions between the above specified ones. The tetragonal phase, space group *P*4*bm*, possesses an unusual combination of in-phase, $a^0a^0c^+$ octahedral tilt and antiparallel displacements of A- and B-cations along the polar axis (pseudocubic [001]). The rhombohedral phase, space group *R*3*c*, has been found to exhibit antiphase, $a^-a^-a^-$ octahedral tilt and parallel displacements of A- and B-cations along the 3-fold axis (pseudocubic [111]). The antiparallel displacement in the tetragonal phase caused very little spontaneous polarization, therefore the tetragonal phase can be characterized as strongly ferroelastic and weakly ferroelectric. The parallel displacement in the rhombohedral phase creates a well-pronounced ferroelectricity in NBT at room temperature. It also has been found that the cation displacements and octahedral tilts are not precisely correlated and behave like weakly coupled distortional degrees of freedom. Thus the rhombohedral phase becomes polar at about 50°C lower than the temperature at which it replaces the tetragonal phase completely. Last, but not least, the neutron diffraction results of Jones and Thomas have demonstrated that NBT possesses no long range Na-Bi cation order.

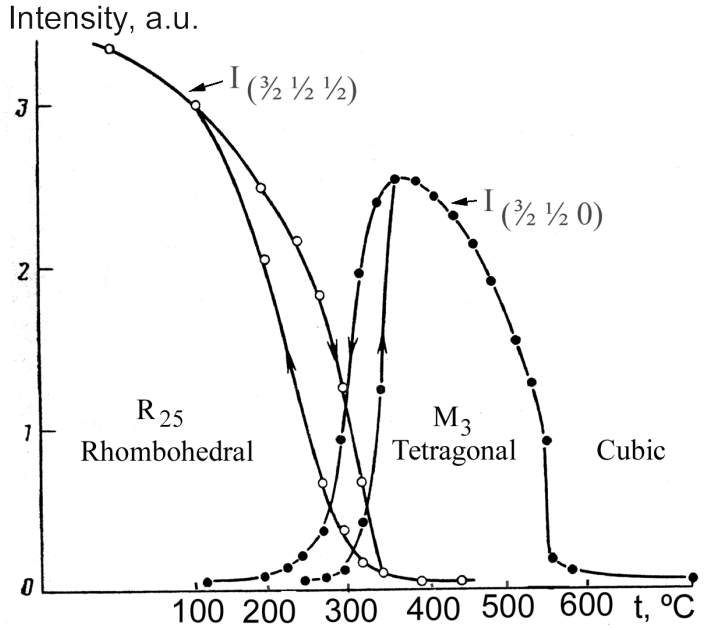

Figure 1.5. Intensities of octahedral tilt superlattice reflections vs. temperature – neutron diffraction data for single crystal NBT [S.B. Vakhrushev, *Ferroelectrics* **63** [1-4] 153-60 (1985)].

Pure (undoped) NBT exhibits quite low piezoelectric properties (d_{33} of about 120 pC/N) and is very hard to pole due to its high coercive field. Doping NBT with barium titanate (BT, space group *P*4*mm*) can enhance piezoelectric response due to the presence of the *morphotropic phase boundary* (MPB). According to Takenaka *et al*. (see Fig. 1.6), the ferroelectric distortion in NBT-BT system has rhombohedral symmetry for BT concentrations <6% and tetragonal symmetry for BT concentrations >6%. Fig. 1.7 gives a graphic schematic of the MPB between ferroelectric rhombohedral and tetragonal phases. Takenaka considers the intermediate phase between ferroelectric and paraelectric to be an antiferroelectric (AF) one, which agrees to an extent with the recent results of Jones and Thomas. What is common in their views is that the intermediate phase is distorted and has low, if any, spontaneous polarization. What is different is that in an AF phase there is an antiparallel displacement of the same ions, whereas the tetragonal phase of NBT exhibits antiparallel displacement of A- and B-cations, i.e. within each sublattice the displacements are parallel.

The most promising from electromechanical performance prospective is the tricritical point between rhombohedral, tetragonal and intermediate phases. At this point, the system is frustrated to the maximum in its choice of the distortional symmetry out of available three types. This frustration should flatten the free energy vs. polarization profile and increase the electromechanical response.

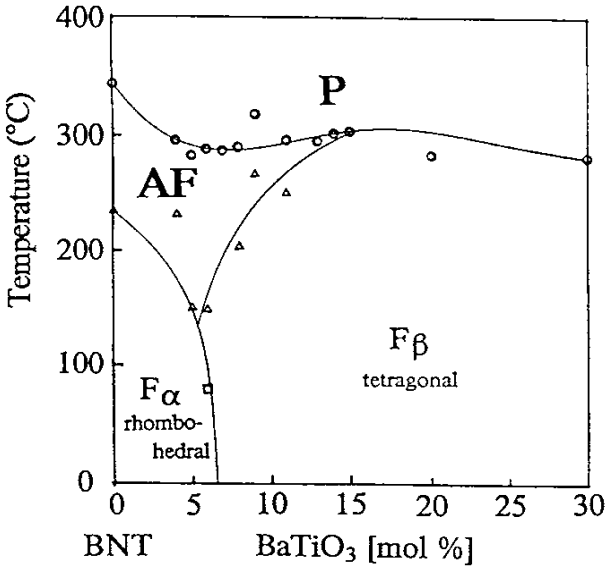

Figure 1.6. Phase diagram of Ba-doped sodium bismuth titanate (BNT–$Na_{1/2}Bi_{1/2}TiO_3$, F–ferroelectric phase, AF–antiferroelectric phase, P–paraelectric phase) [T. Takenaka, *Jpn. J. Appl. Phys*. **30** 2236 (1991)]

The tricritical point similar to the described one can also be obtained if one replaces temperature with concentration of another component. Then it will be a triple point on a quasi-ternary system phase diagram. Zirconium ion has been picked to imitate the effect of temperature since it has been known to suppress ferroelectricity in perovskites due to its larger size, e.g. in the $PbZrO_3 - PbTiO_3$ (PZT) system [G.A. Rossetti, *J. Solid State Chem.* **144** (1) 188-194 (1999)]. This concludes the presentation of our rationale for selecting $(Bi_{1/2}Na_{1/2})TiO_3 - BaTiO_3 - (Bi_{1/2}Na_{1/2})ZrO_3$ or, in a condensed form, $(Bi_{1/2}Na_{1/2})_{1-x}Ba_xZr_yTi_{1-y}O_3$ (BNBZT) system as the subject of this research. The polycrystalline form was selected due to its ease of processing and compositional control.

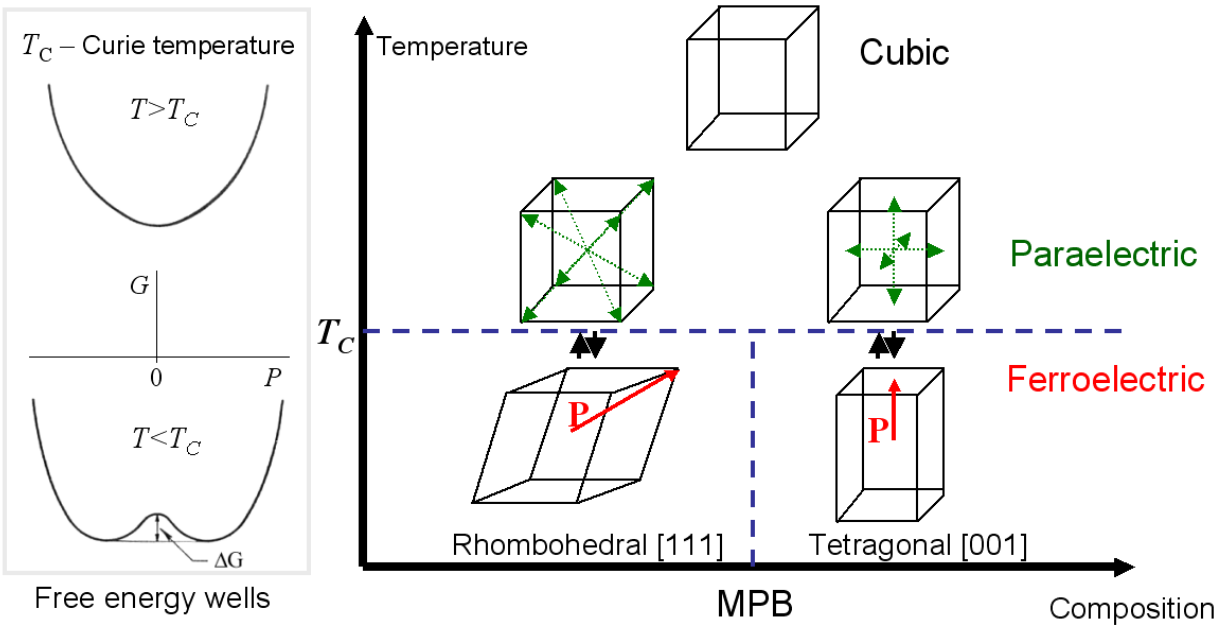

Figure 1.7. Schematic of the rhombohedral-tetragonal morphotropic phase boundary (MPB). On the left: free energy vs. polarization profiles for the paraelectric phase (top curve) and ferroelectric phase (bottom curve). Dashed arrows show possible directions for the spontaneous polarization (solid arrows) to realize.

Chapter 2

EXPERIMENTAL PROCEDURE

Based on the considerations outlined in the previous chapter, a set of stoichiometric compositions $(Na_{1/2}Bi_{1/2})_{1-x}Ba_x(Ti_{1-y}Zr_y)O_3$ were identified and prepared for which Ba^{2+} and Zr^{4+} substitute on the A- and B-sites, respectively. This composition system will be referred to as a BNBZT solid solution and *x* and *y* will be called % Ba and % Zr, respectively.

Polycrystalline Powder Preparation

High purity (>99 % purity), ultra-fine grain size ($\leq$1 µm) starting powders of Na_2CO_3, Bi_2O_3, $BaCO_3$, TiO_2, and ZrO_2 were mixed in 15, 20, or 25 g sized batches according to the intended stoichiometric composition of the sintered pellets (Fig. 2.1). Powder batches are intuitively designated "z*y*b*x*" where *x* and *y* are % Ba and % Zr in BNBZT system respectively: z1b6.5, z1b7, z2b6.5, z2b7, z2b14, z3b4, z3b6, z3b14, z3b15, z3b18, z4b7, z4b12, z4b16, z4b18.

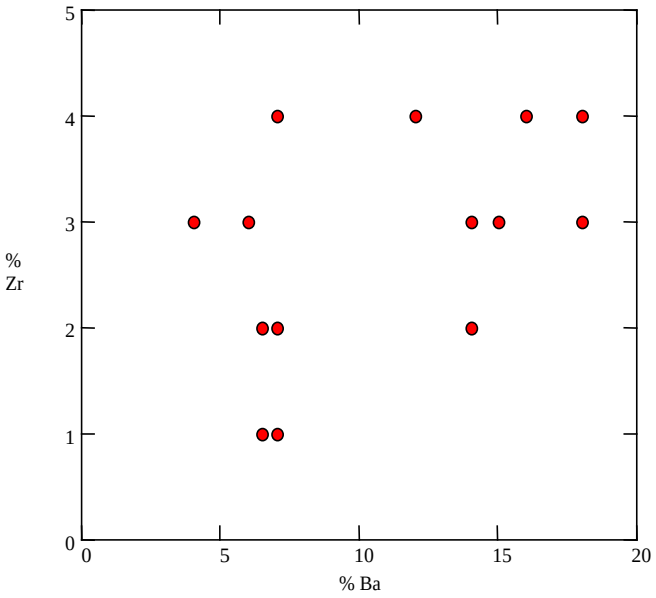

Figure 2.1. BNBZT compositions studied in this work

The electromechanical test samples were prepared by H. Cai, MIT except for the underlined compositions, which were prepared by S.A. Sheets [MS Thesis, MIT 2000]. The author contributed in the selection of compositions and the development of the sample preparation procedure. The pellets z2b14, z3b15, z3b18 and z4b16 were pressed, sintered, polished and electroded by the author. The mixed powders were formed into slurries of a creamy consistency by the addition of ethanol (15 – 20 ml for 20 g batch, ~ 45 ml for 100 g crystal growth batch). Slurries were ball-milled with cylindrical (1/4"-radius ended) zirconia media on a roller mill for 20 hours. After milling, slurries were rinsed with ethanol into a glass dish and set in a hood to dry under a heat lamp (12 hours). Once dried, the soft, yellowish precursor powders were ground with a zirconia mortar and pestle, transferred to a covered alumina crucible and calcined in air at 800?C for 3 hours. A *Thermolyne 47900* series box furnace was used for the first calcination, set to heat at a rate of 100?C/hr and cool, unpowered, to room temperature. After the first calcination, the now ivory-colored powders were highly agglomerated, but easily crumbled. After grinding vigorously with a zirconia mortar and pestle, the powders were calcined again in air at 1000?C for 20 hours. A *Thermolyne 46100* series high temperature furnace with $MoSi_2$ heating elements was used for this second calcination, heating to 1000?C and cooling to 800?C at 100?C/hr. Cooling below 800?C proceeded at an unpowered rate to room temperature. After the second calcination, powders were white and highly agglomerated, but soft. They easily crumbled when ground in a zirconia mortar. X-ray powder diffraction (Rigaku Bragg-Brentano X-ray diffractometer with 18 kW generator, copper rotating anode) confirmed single-phase perovskite with trace amounts of foreign phases (<1% relative peak intensity).

Dense polycrystalline samples were prepared for electromechanical characterization from all of the above listed powder batches. Between 0.8 and 1 g of powder was weighed out and ground in a zirconia mortar. To promote dense packing, powder particles were coated with a polymer binder, polyvinyl alcohol (PVA), before pressing. Approximately 0.5 ml of 5 wt% PVA solution in water was added to the ground powders, just enough to coat all the grains. The binder was mixed thoroughly into the powder with a pestle and the resulting paste was allowed to dry, grinding occasionally until a hardened, granular consistency was achieved. The coated powder was then pressed through a 500 µm mesh nylon screen. This produced evenly sized granules that

flowed smoothly and packed densely. The coated granules were poured into a 1/2" die that had been lubricated with a thin layer of oleic acid. Samples were pressed in a manual hydraulic press by slowly increasing pressure, holding 15 s every 30 MPa until a maximum of 100 MPa was reached. The maximum pressure was held for 30 s before gradual releasing. Pressing resulted in a highly consolidated green body with disc geometry. The disc edges were sanded with 15μm-grit silicon carbide paper in order to remove edge contamination from the steel die. Green body discs were placed on a layer of platinum foil within an alumina dish. The dish was fitted with an alumina lid with a hole in the center, in order to allow efficient lubricant and binder burnout yet minimize bismuth loss during sintering. Discs were sintered in air at 1200?C for 4 hours in a *Thermolyne 46100* series high temperature furnace with a heating rate of 100?/hr to maximum temperature and a controlled cooling rate of 100?/hr to 800?C. The sintered discs were approximately 10 mm in diameter with thickness between 1-2 mm and had near-full density (> 95%) determined by examination of polished cross-sections under optical microscope with ? 500 magnification.

Single Crystal Growth

Single crystals in the BNBZT system were grown by G.W. Farrey (Zr-free compositions) [MS Thesis, MIT 2000] and S.A. Sheets [MS Thesis, MIT 2000] using the self-flux method. The author contributed to the development of the crystal growing schedule, *in-situ* melting observation in particular [S.A. Sheets, MS Thesis, MIT 2000]. The author performed cutting, polishing, thinning, optical and transmission electron microscopy. High purity (>99 % purity) starting powders of Na_2CO_3, Bi_2O_3, $BaCO_3$, TiO_2, and ZrO_2 were mixed in 100 g sized batches according to intended nominal stoichiometric compositions with the addition of a self-flux composed of 20 wt% excess each of Na_2CO_3 and Bi_2O_3.

Powder preparation followed the same procedure through the first calcination at 800?C as described in the previous section for polycrystalline samples. After the first calcination, powders were ground in a zirconia mortar and transferred to a 100 ml covered platinum crucible. The platinum crucible was fitted inside a larger, covered alumina crucible. The powders were treated according to the schedule: R.T.→1350?C @ 100?/hr, hold 5 hours, 1350?C → 1260?C @ 100?/hr, hold 1 hour, 1260?C → 1000?C @ 1.5?/hr, 1000?C → R.T. @ 50?/hr that typically yielded intergrown crystals

set within solidified flux. Weight loss was less than 1% for all crystal growths, indicating that bismuth loss due to volatilization was not significant. Crystals were mechanically separated from the crucible and the flux. Intergrown crystals would be separated either with a *Well* diamond wire saw or broken apart with a hammer.

Sample Preparation

Sintered polycrystalline pellet-shaped bodies were mounted with crystal bond on a *South Bay Technology* tripod holder and polished using diamond abrasive film from 30 µm to 1 µm grit. Polished disc geometry averaged ~ 10 mm in diameter, and thickness below 2 mm. The dimensions (diameter and thickness) of the disk shaped samples were measured with a digital micrometer (5 µm error margin) and averaged over 4 measurements on each sample. The relative thickness variation was below 7 %. Samples were ultrasonically cleaned in three acetone baths. Touch up cleaning when necessary was performed by wiping sample surfaces with a cotton-tipped applicator soaked in ethanol. Single crystal plates of a desired crystallographic orientation were first cut from oriented (using easily detectable <001> faces) larger crystals with a *Well* diamond wire saw and then polished in the same manner as the polycrystalline samples. Fig. 2.2 shows the appearance of the samples after polishing.

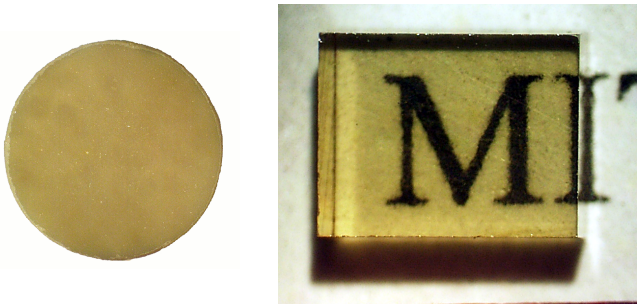

Polycrystalline Disc (o 10 mm) Single Crystal Plate (3x4 mm)

Figure 2.2. BNBZT samples after polishing

The single crystal plates for transmission electron microscopy were thinned using an Ar-ion mill. We used a *Topcon/Akashi 002B* High Resolution TEM (HREM) with double tilt sample holder and a *JEOL-200CX* TEM equipped with a high temperature single tilt stage.

Composition Analysis by Electron Microprobe

Achievement of target compositions in the BNBZT samples within the measurement error was confirmed by quantitative chemical analysis of both polycrystals and single crystals using the *JEOL JXA-733* Electron Probe Microanalyzer (EPMA). Clean samples were sputter coated with carbon before being loaded into the EPMA to prevent charging. The samples were analyzed for elements Na, Bi, Ba, Ti, and Zr using the following standards: $NaAlSi_3O_8$, $Bi_4Ge_3O_{12}$, $BaSO_4$, TiO_2, $ZrSiO_4$. One set of samples was also analyzed for Hf using pure element as standard in order to assess the degree of hafnium contamination from the zirconia starting powders. Hafnium contamination was determined negligible in all samples tested. The current (10 nA), voltage (15 kV) and take-off angle (40?) were kept constant during the measurements. Oxygen was not analyzed. Based on the light color of the samples, no oxygen vacancies were assumed and compositions were normalized to 3 oxygen atoms per formula unit (ABO_3).

Sample Electroding

Prior to electromechanical measurements, both flat surfaces of each sample were electroded. Gold electrodes of ~ 1 μm thickness were sputtered for 300 seconds at 40 mA and 0.08 mbar Ar pressure on sample surfaces with a *Pelco SC-7 Auto Sputter* coater. The distance between the sample and gold target was approximately 4 cm. Scotch tape was used to protect the side surfaces of the samples from being covered with gold. The electrodes on samples were annealed in air at 475?C for 1 hour in order to bond the electrode to the surface and increase the strength of the electrodes.

Electromechanical Characterization

Room temperature electric field induced strain and polarization of BNBZT polycrystalline samples were simultaneously measured by the author during application of 0.2, 1, 10, 22 and 47 Hz sinusoidal fields and 1 MPa constant prestress using a custom design electromechanical test rig (Fig. 2.3).

The rig prototype was designed and built by the author (G.R. Maskaly, MIT assisted with the manufacture); the final version was designed by B.P. Nunes [MS Thesis, MIT 2001] (the author advised on the final design). The rig is unique in its capability to simultaneously measure electric field induced strain and polarization of samples immersed in silicone oil under a constant compressive loads up to 20 kN and voltages up to 10 kV without strain gauges attached to the sides of the sample. The absence of strain gauges allows samples with any thickness below 12 mm to be tested (the smallest available strain gauges require at least 4 mm thick samples, with which application of high electric fields is problematic due to the voltage limit of the amplifier).

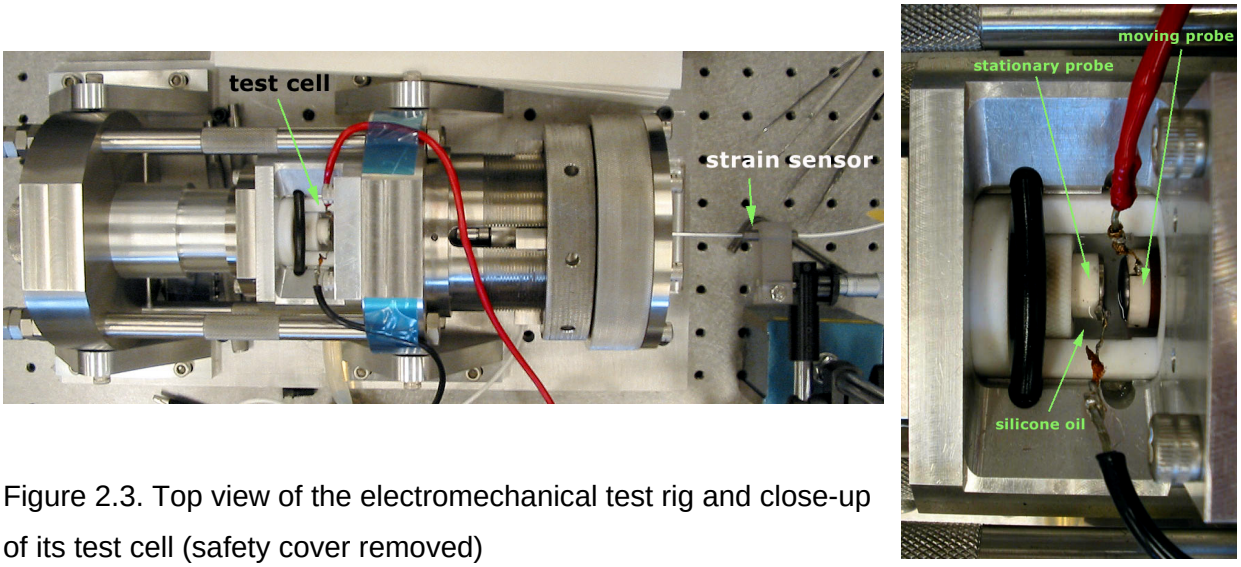

Figure 2.3. Top view of the electromechanical test rig and close-up of its test cell (safety cover removed)

The oil is required to prevent electric arcing through air. An electroded sample of plate or disk shape is immersed into silicone oil contained in the Teflon bath, placed between the probes and secured by adjusting the position of the stationary probe by rotation of the adjustment bolt (left part of the rig). Prestress (1 MPa for all samples) is adjusted with a spring loaded by the rotation of the prestress nut (knurled disk with holes on the right) and pushing on the moving probe, held by two flexes to confine its movement to one axis (perpendicular to the sample electroded surfaces). The prestress was necessary to prevent gaps between the sample and the probes. The right end of the moving probe is connected to frictionless *nano-DVRT* strain sensor by *Microstrain Inc.* having the range of 100 µm, resolution of 25 nm, and response time of 3 ms. Both probes have stainless

steel caps insulated from the ground and connected to the polarization measurement system with two high voltage cables shown on Fig 2.3.

The polarization was measured with a virtual ground circuitry *Precision Workstation* by *Radiant Technologies Inc*. The system includes a PC, a multi-channel digitizing board, high voltage interface and ±10 kV high voltage amplifier. The ±10 V analog output from the strain sensor is fed to the external sensor channel of the digitizing board and is recorded simultaneously with the polarization data by the control-and-acquisition software. The latter saves data in a table form: applied field, polarization and strain versus time. The standard test included three cycles of sinusoidal bipolar $E = E_m \sin(2\pi f t)$ or unipolar $E = E_m [1 + \sin(2\pi f t)]/2$ field, where E_m is the maximum applied field, f is frequency and t is time. The lower limit of the frequency (0.2 Hz) of the applied field was determined from the maximum period of acquisition whereas the higher limit (47 Hz) was determined by the current capacity of the high voltage amplifier and the capacitance of the samples. For samples with large capacitance, the 47 Hz output voltage profile was automatically scaled down by the measurement system to keep the output current under the capacity. Only the third cycle (300 measurement points) was recorded to omit transient phenomena and analyze the attractor trajectory in the field-polarization-strain space.

Previous measurements of BNBZT poly- and single crystals [S.A. Sheets, MS Thesis, MIT 2001] have been performed using a different strain and polarization measurement system (*Zygo* laser velocimeter and *Trek* high voltage amplifier connected to a *National Instruments* multichannel board run by *LabView* software). Although strain measurements were adequate (the only significant demerit was substantial drift of baseline at low frequencies due to integration of noise contained in the velocity data from the laser interferometer), the polarization measurements had inferior reproducibility due to a random magnitude and random sign phase shift between strain and polarization measurements produced by the acquisition hardware and/or software. In addition, the current signal from the *Trek* amplifier, which was used to obtain polarization by the integration in time, contained substantial high-frequency narrow band (~100 kHz) noise that could not be eliminated by oversampling. As we show in this work, in the studied range of composition in the BNBZT system polarization is the primary order parameter, field induced strain being completely coupled to it. Therefore, in order to obtain a reliable measurement of polarization and clarify the

character of phases of BNBZT at different compositions and fields it was necessary to remeasure a number of samples that have been measured by S.A. Sheets.

Compositional Maps

Since the studied compositions vary in both Ba and Zr concentrations it is necessary to use maps of properties to represent their compositional dependencies in an easy to perceive form. The maps were constructed from the tables of experimental data using *Mathcad 2000* software by *MathSoft, Inc.* We used 20x20 interpolation mesh to plot the contour lines. It has been found that the pattern of the contour lines does not qualitatively change when the resolution of the mesh is above 7x7. This fact shows that the maps in this work are not mesh-specific but rather objectively represent the observed trends in properties. However, the precision of the compositional maps is not uniform: their predictive power in the regions far from the experimental points is significantly limited.

Chapter 3

OBSERVED ELECTROMECHANICAL BEHAVIOR

The recorded electromechanical behavior is presented as four sets of curves:

bipolar polarization P	unipolar polarization P
bipolar strain S	unipolar strain S

All curves are plotted vs. electric field. Each set consists of curves representing all tested frequencies. It should be noted that although all the above plots are non-linear and hysteretic, the plots of strain vs. polarization squared displaying how well the electrostriction relation $S = Q P^2$ holds are practically linear, hysteresis free and overlap for all tested frequencies. These plots are not presented here since they can be expressed for each sample by the single value of electrostrictive coefficient Q, which is compositionally mapped at the end of this chapter. The frequency dependences for all samples are monotonic: a response to a higher frequency is always lower due to relaxation phenomena. This fact helps to identify curves on the plots.

Some samples exhibited leakage current. As a result, their unipolar polarization loops are not closed by the amount proportional to the leaked charge. The latter increases with decreasing frequency.

Since the samples cover a 2D map of concentrations, the plots are represented in the order of increasing Zr concentration and then Ba concentration as the secondary order criterion.

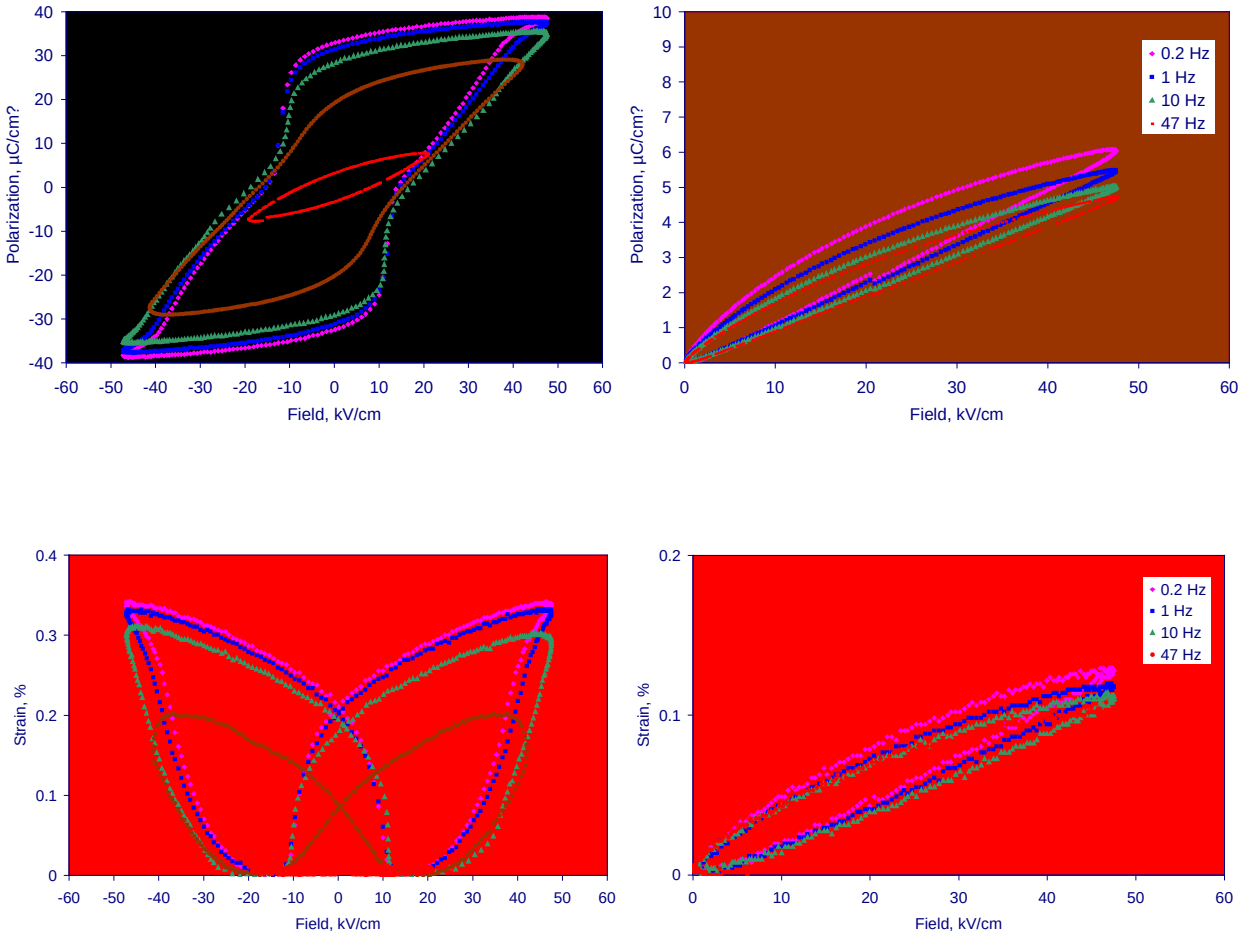

Figure 3.1. Electromechanical behavior of z1b6.5

The z1b6.5 sample shows high strain and high hysteresis. The shape of the hysteresis loop is “a pinched loop”—a sign of a field induced phase transition. Note four inflection points on the bipolar polarization loops.

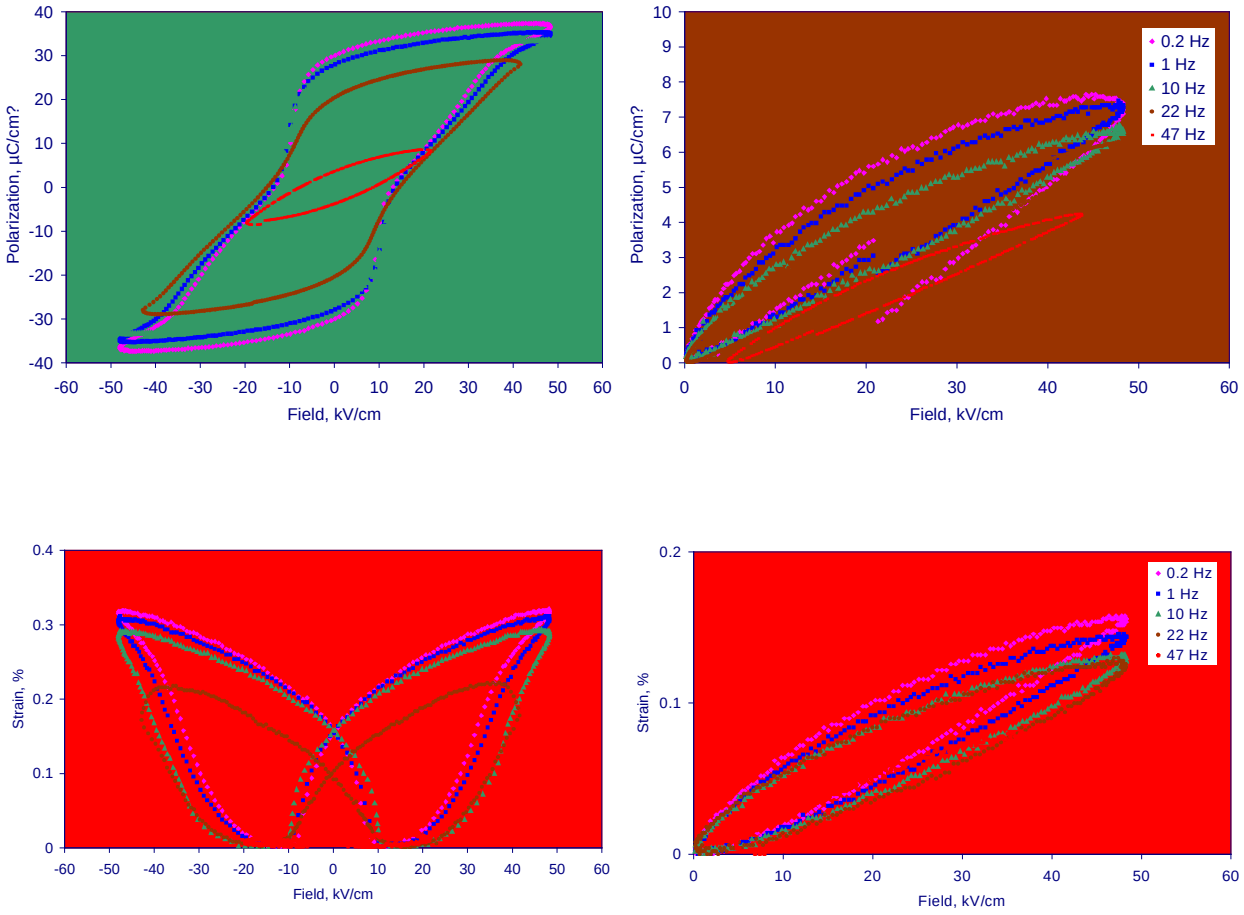

Figure 3.2. Electromechanical behavior of z1b7

The z1b7 sample shows high strain and high hysteresis. The shape of the hysteresis loop is "a pinched loop"—a sign of a field induced phase transition. Note four inflection points on the bipolar polarization loops.

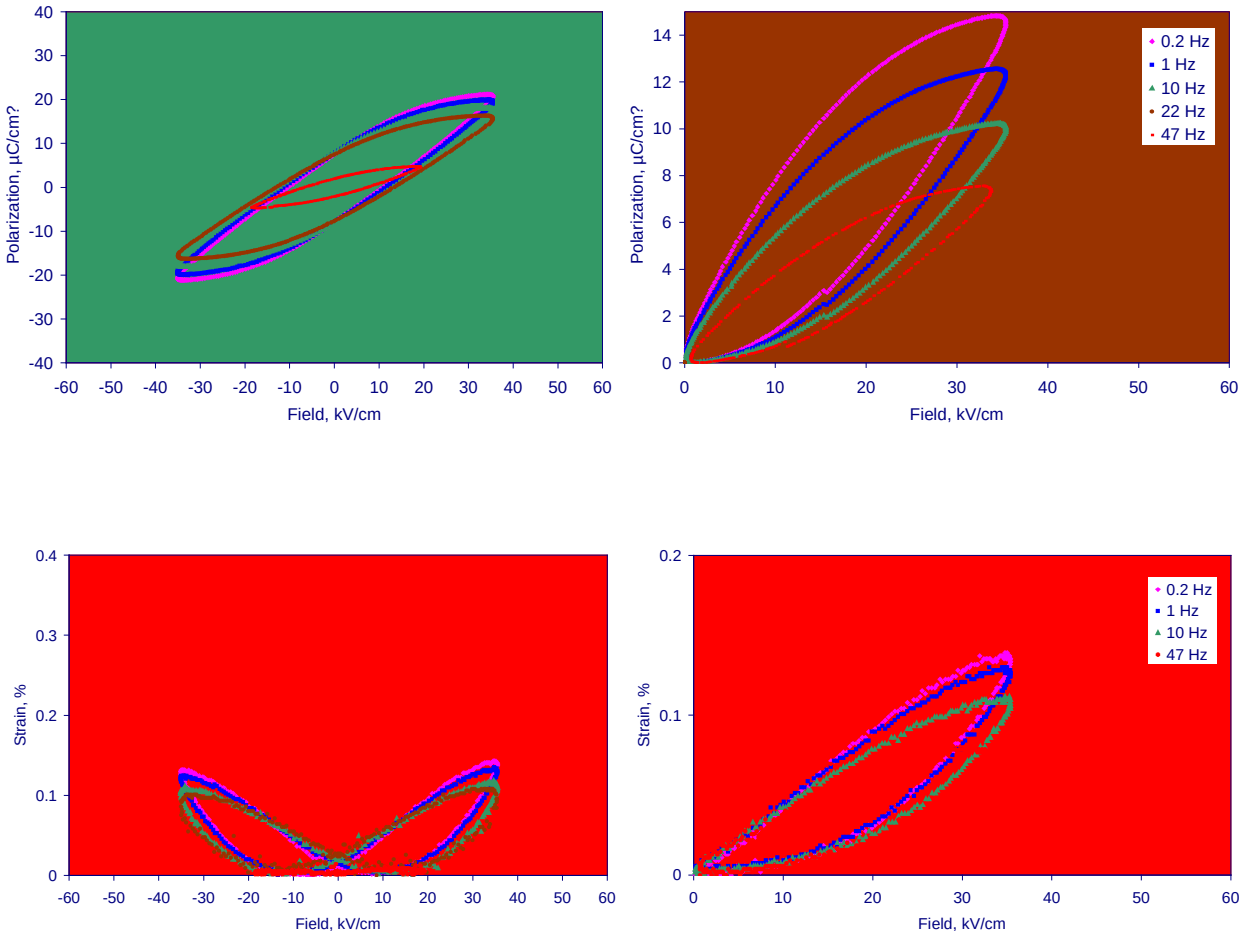

Figure 3.3. Electromechanical behavior of z2b6.5

The z2b6.5 sample was too thick to apply high field and reach the saturation of polarization. The next sample with almost the same composition provides the missing information.

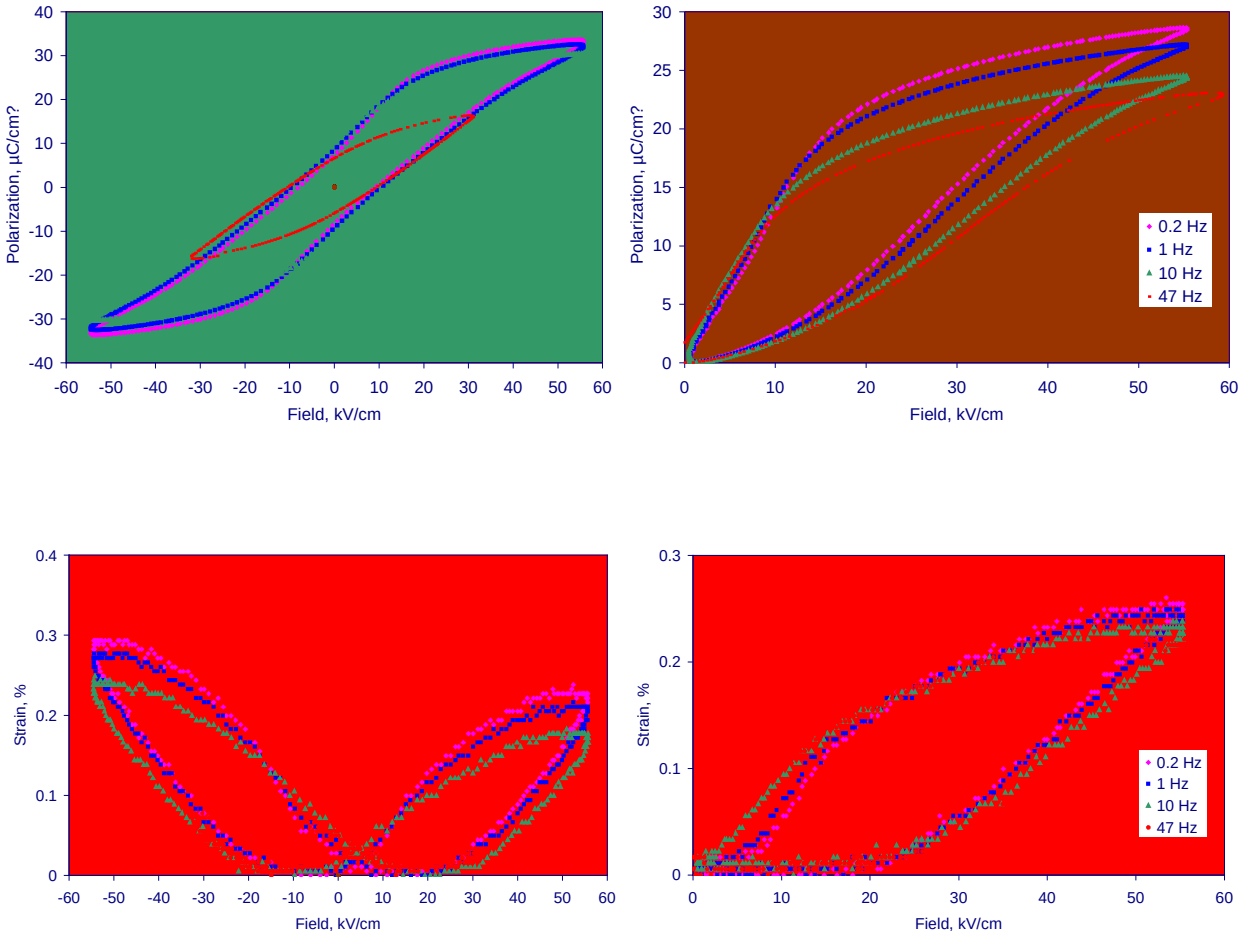

Figure 3.4. Electromechanical behavior of z2b7

The z2b7 sample shows high strain and high hysteresis. The shape of the hysteresis loop is "a pinched loop"—a sign of a field induced phase transition. Note four inflection points on the bipolar polarization loops. The unipolar loops are extremely hysteretic: the high field phase disappears completely when the field goes back to zero. Bias in the bipolar strain is not uncommon. It reflects certain built-in gradients of composition and/or stress in the sample due to some asymmetry of processing conditions: heat treatment and polishing.

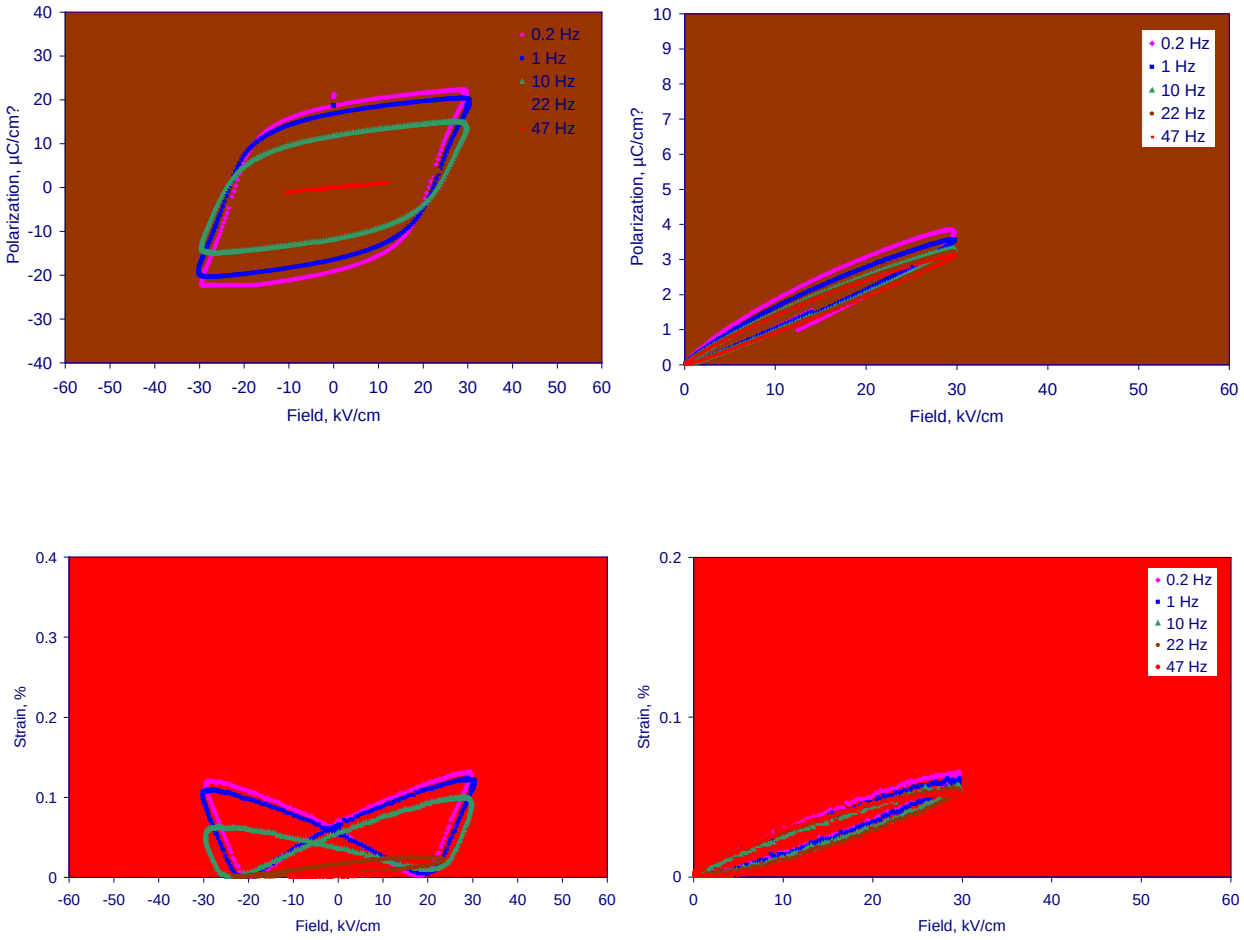

Figure 3.5. Electromechanical behavior of z2b14

The z2b14 sample exhibits classical ferroelectric behavior. Note two inflection points on the bipolar polarization loops. The unipolar plots show little hysteresis since the domain state realized at high fields does not switch until the field is reversed and its magnitude is above the coercive field. Strains and polarizations are moderate.

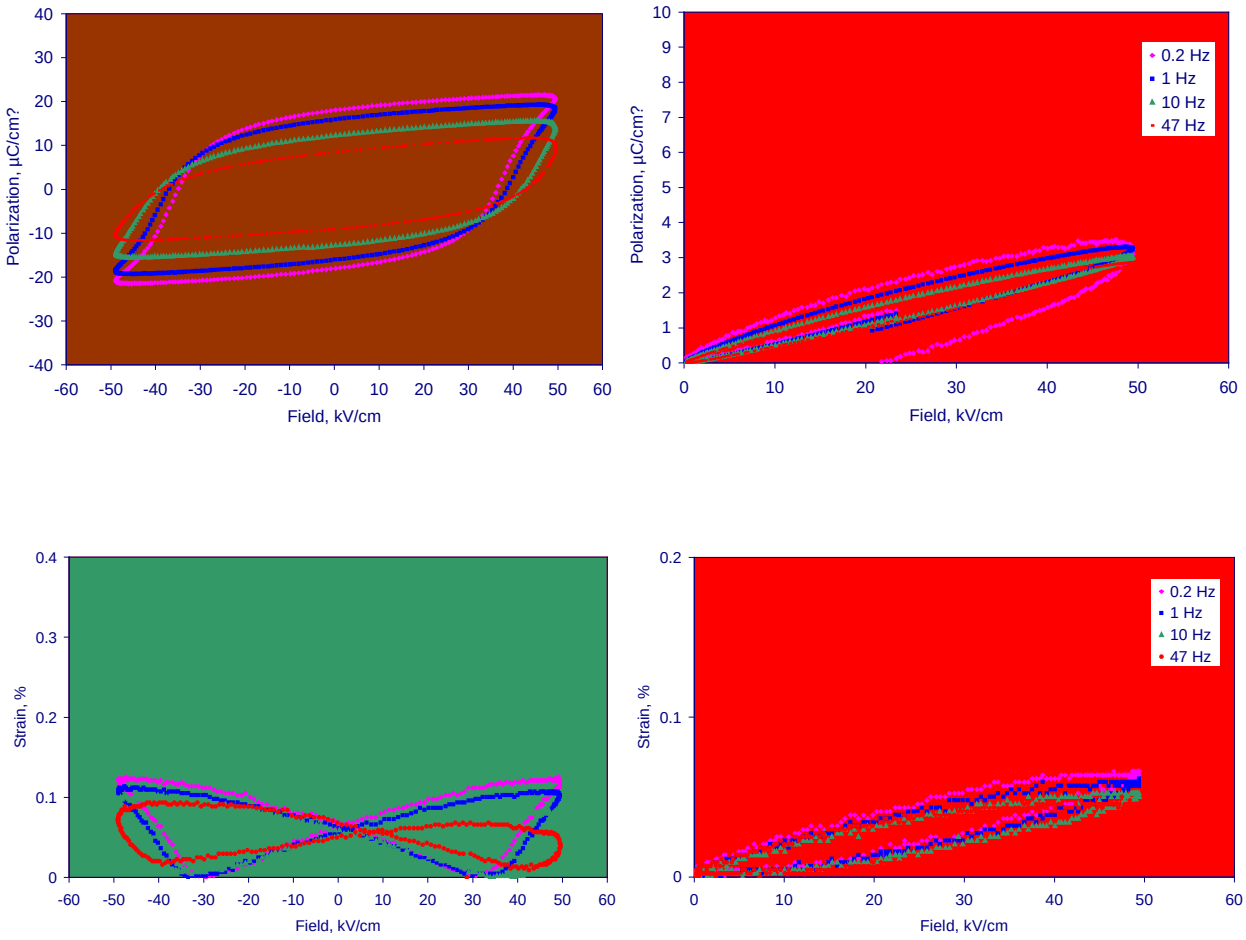

Figure 3.6. Electromechanical behavior of z3b4

The z3b4 sample exhibits classical ferroelectric behavior. Note two inflection points on the bipolar polarization loops. The unipolar plots show little hysteresis since the domain state realized at high fields does not switch until the field is reversed and its magnitude is above the coercive field. Strains and polarizations are relatively low.

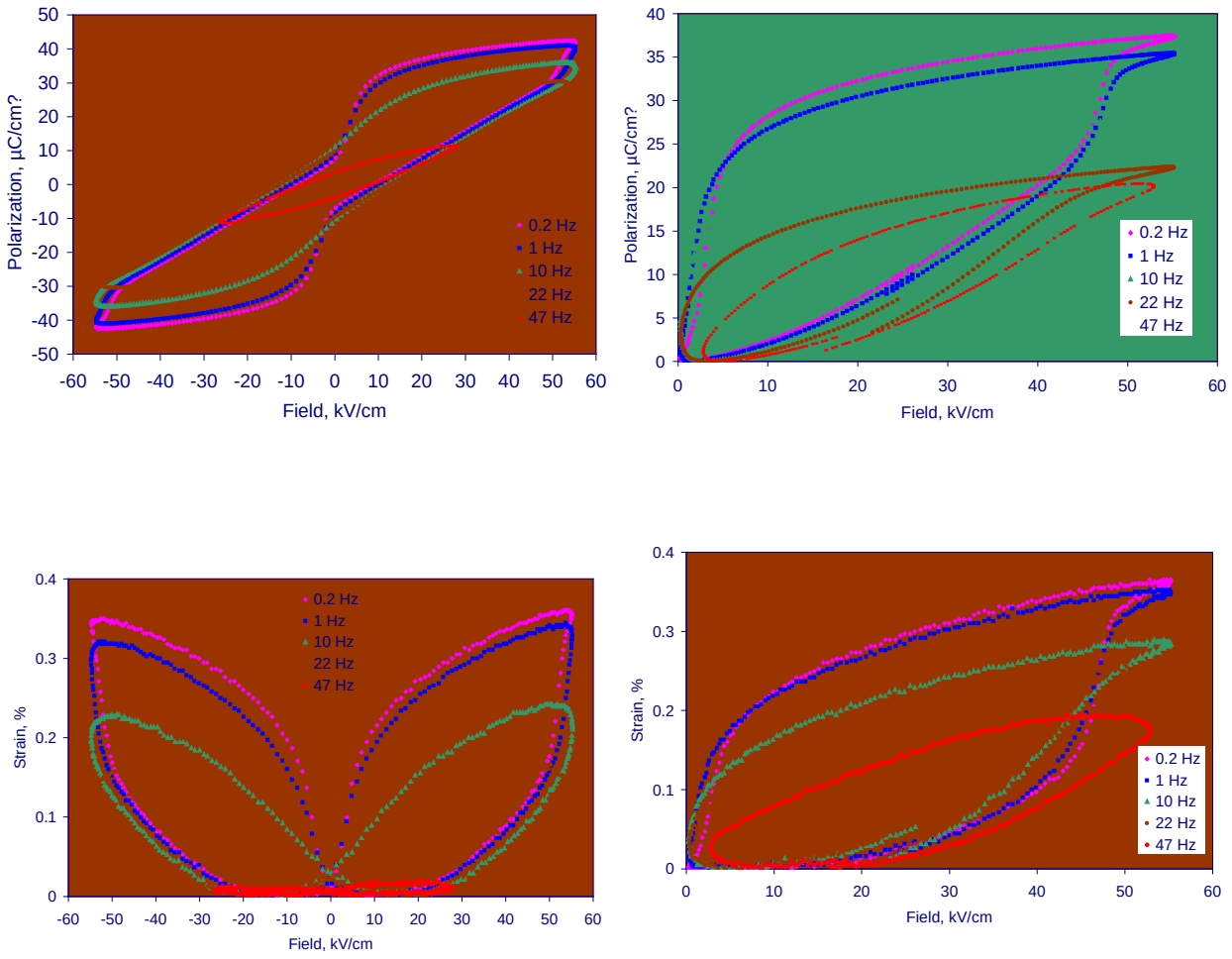

Figure 3.7. Electromechanical behavior of z3b6

The z3b6 sample exhibits very high strain and high hysteresis. The shape of the hysteresis loop is “a pinched loop”—a sign of a field induced phase transition. Note four inflection points on the bipolar polarization loops. The unipolar loops are extremely hysteretic: the high field phase disappears completely when the field goes back to zero.

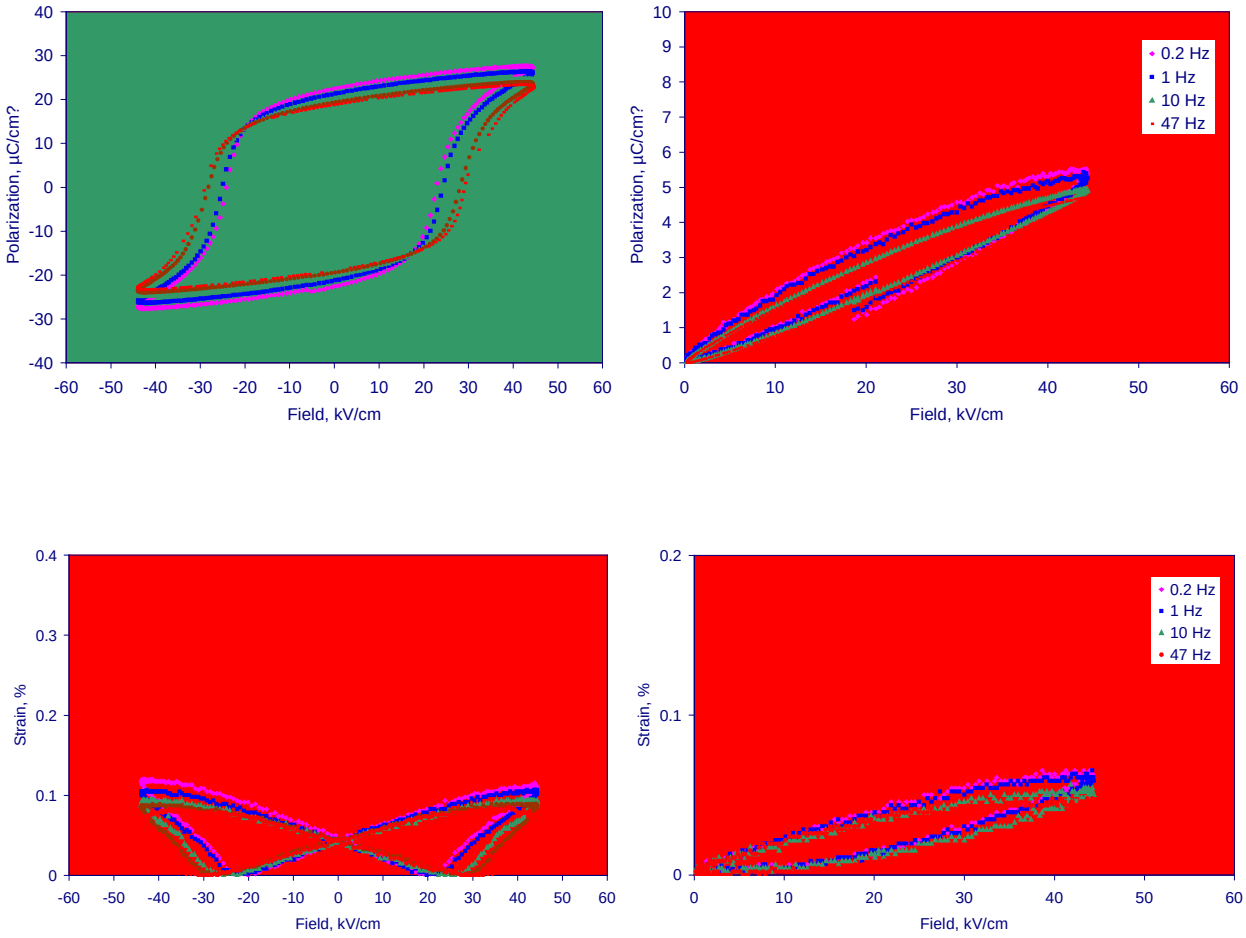

Figure 3.8. Electromechanical behavior of z3b14

The z3b14 sample exhibits classical ferroelectric behavior. Note two inflection points on the bipolar polarization loops. The unipolar plots show little hysteresis since the domain state realized at high fields does not switch until the field is reversed and its magnitude is above the coercive field. Strains and polarizations are moderate. It should be noted that the z3b14 sample in this work exhibited lower strain and higher coercivity than its counterpart in S.A. Sheets' work [MS Thesis, MIT 2000]. The difference can be attributed to slightly different concentrations of bismuth due to not fully controlled bismuth loss during firing and shows very high sensitivity of the electromechanical response to the composition and nonstoichiometry in particular.

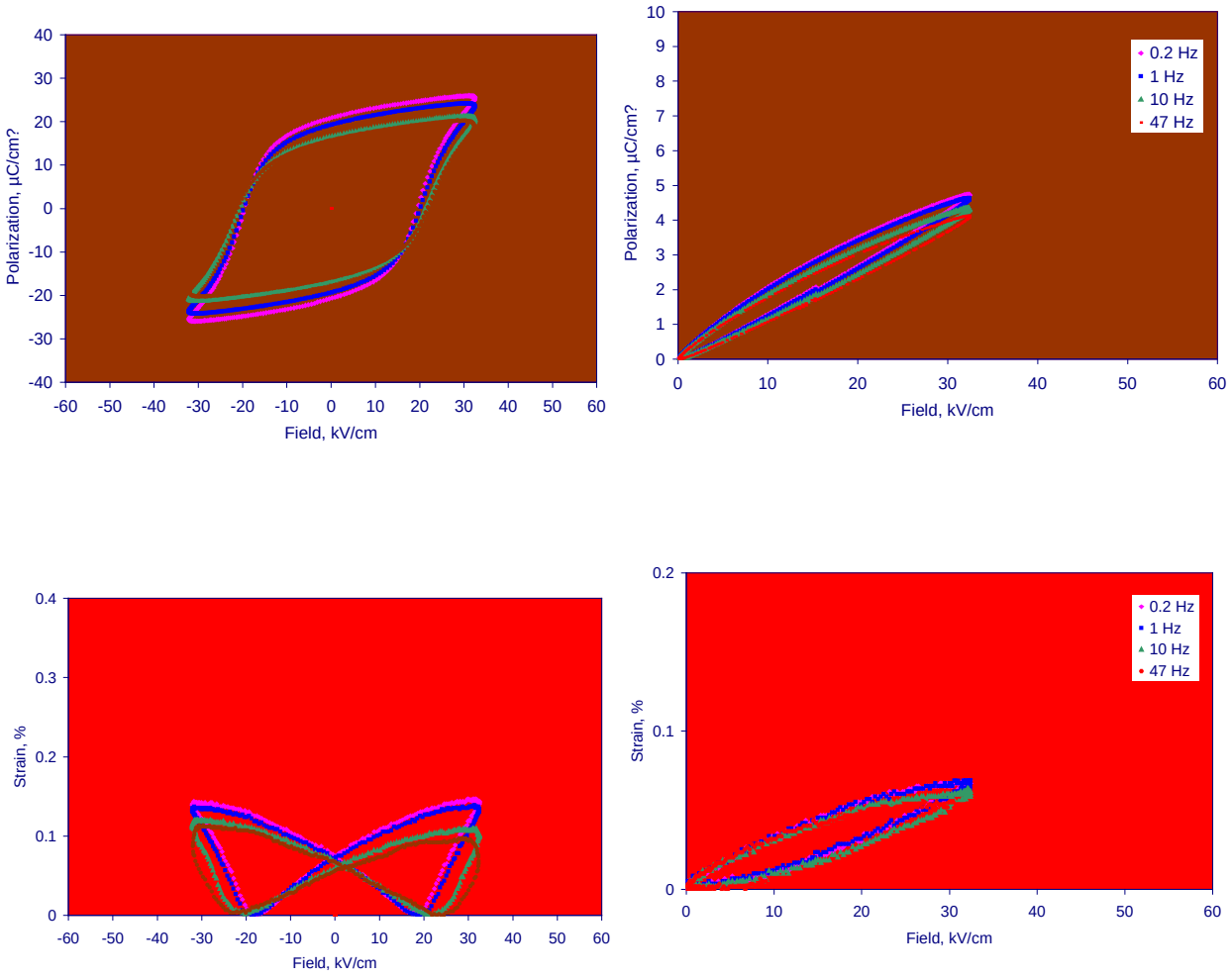

Figure 3.9. Electromechanical behavior of z3b15

The z3b15 sample exhibits classical ferroelectric behavior. Note two inflection points on the bipolar polarization loops. The unipolar plots show little hysteresis since the domain state realized at high fields does not switch until the field is reversed and its magnitude is above the coercive field. Strains and polarizations are moderate.

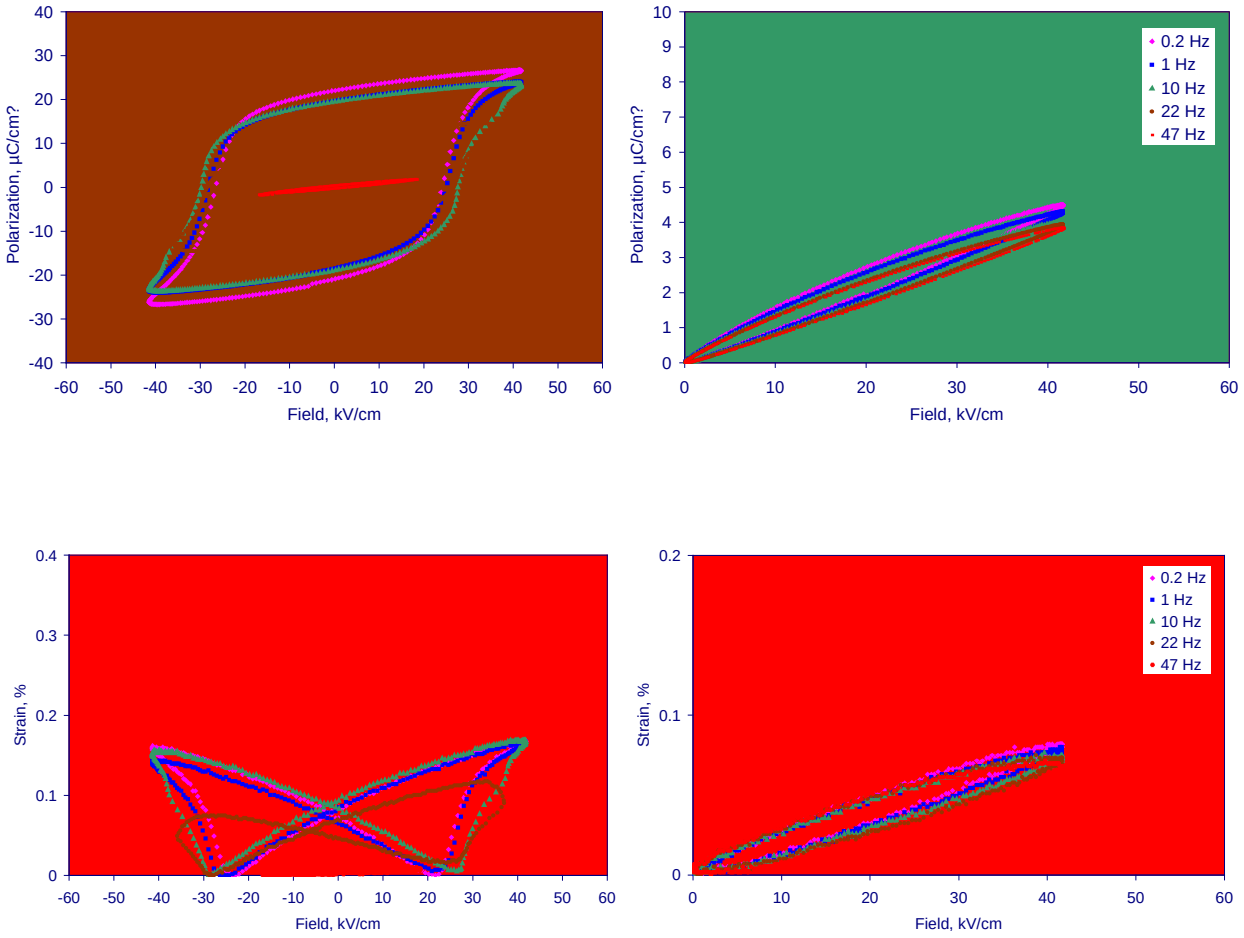

Figure 3.10. Electromechanical behavior of z3b18

The z3b15 sample exhibits classical ferroelectric behavior. Note two inflection points on the bipolar polarization loops for 0.2 and 1 Hz. The 10 Hz plots exhibit a little kink at about ±38 kV/cm. It is a singular phenomenon and it will not be analyzed. The unipolar plots show little hysteresis since the domain state realized at high fields does not switch until the field is reversed and its magnitude is above the coercive field. Strains and polarizations are moderate.

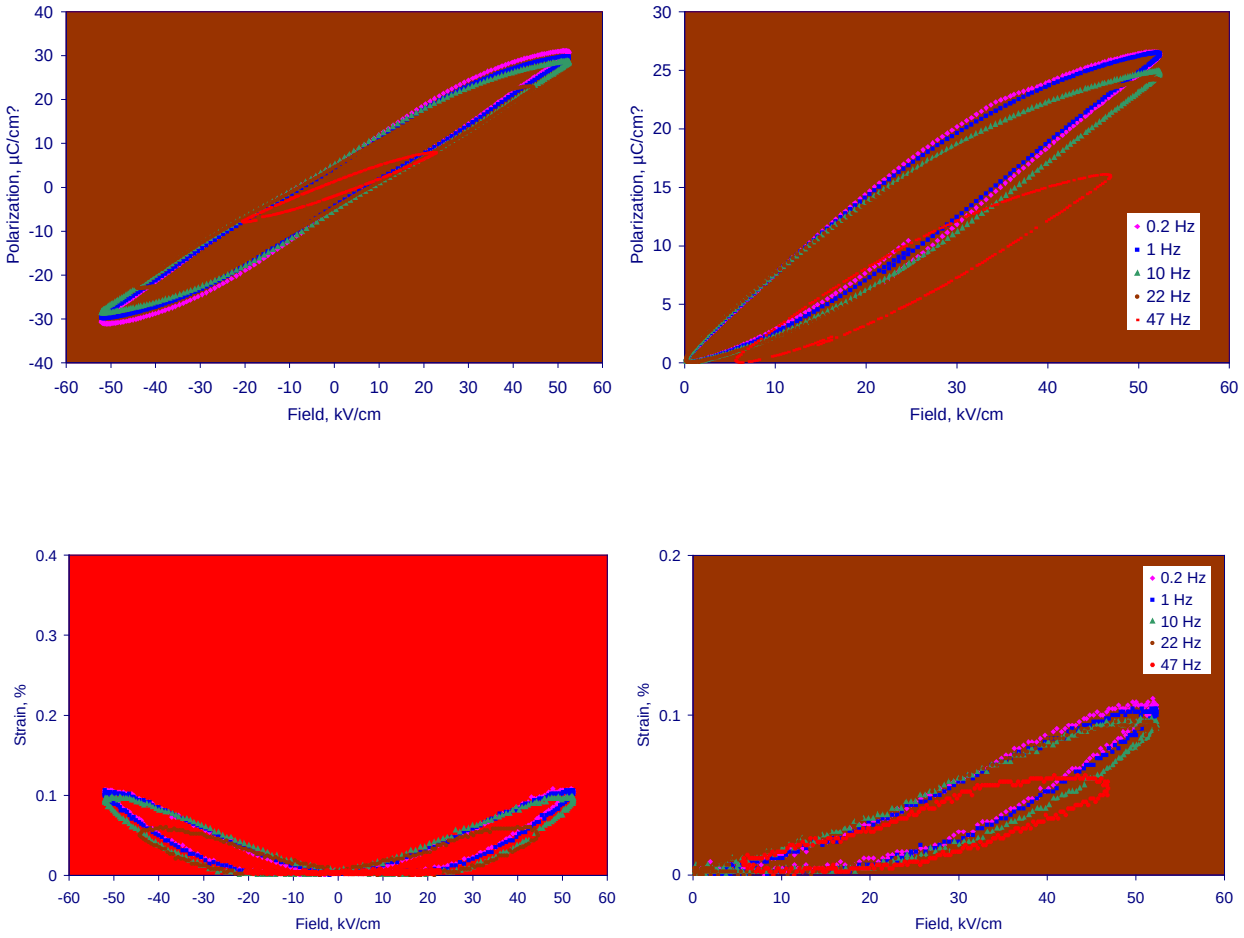

Figure 3.11. Electromechanical behavior of z4b7

The z4b7 sample exhibits substantial strain and hysteresis. The shape of the hysteresis loop is “a pinched loop”—a sign of a field induced phase transition. Note four inflection points on the bipolar polarization loops.

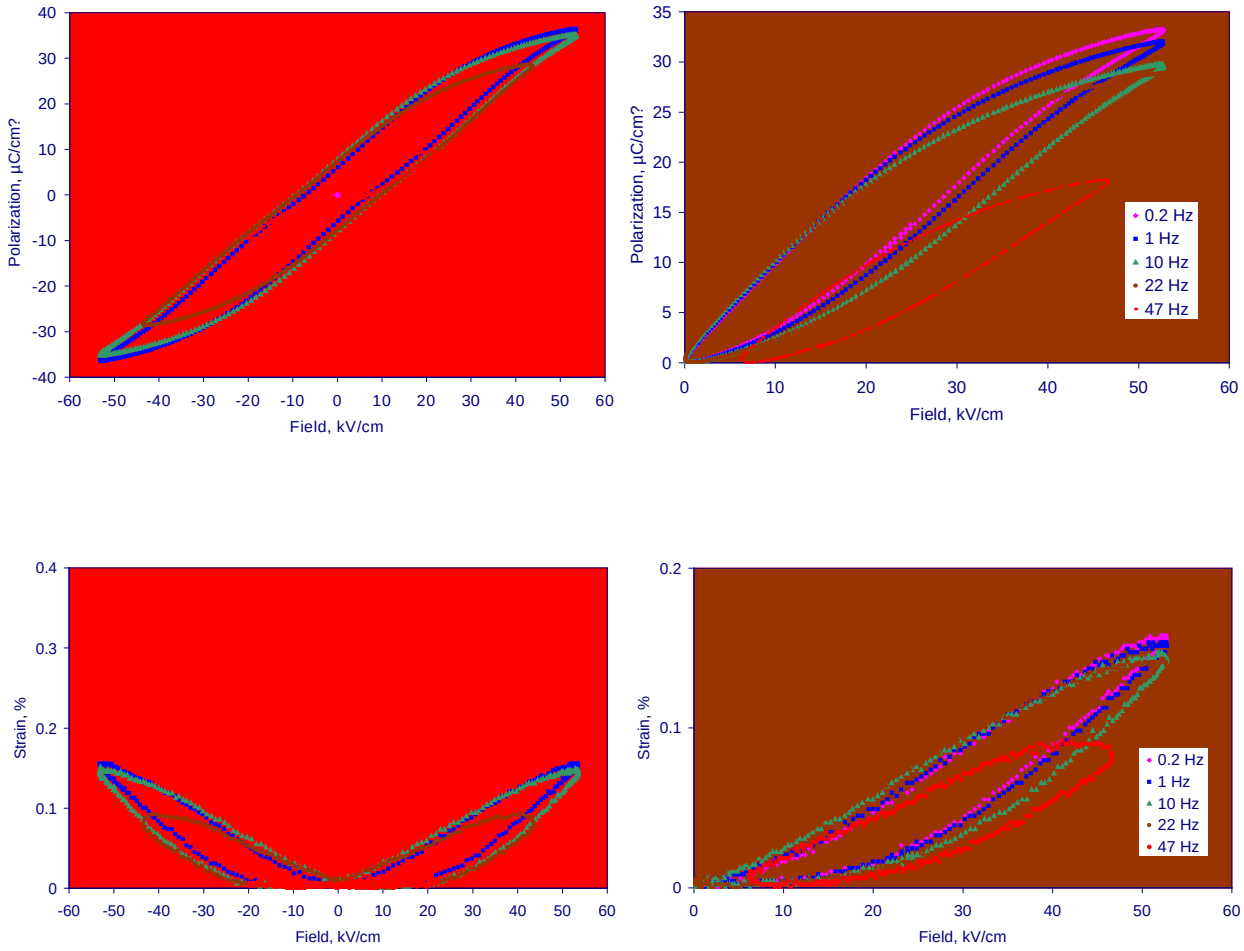

Figure 3.12. Electromechanical behavior of z4b12

The z4b12 sample exhibits substantial strain and hysteresis. The shape of the hysteresis loop is “a pinched loop”—a sign of a field induced phase transition. Note four inflection points on the bipolar polarization loops.

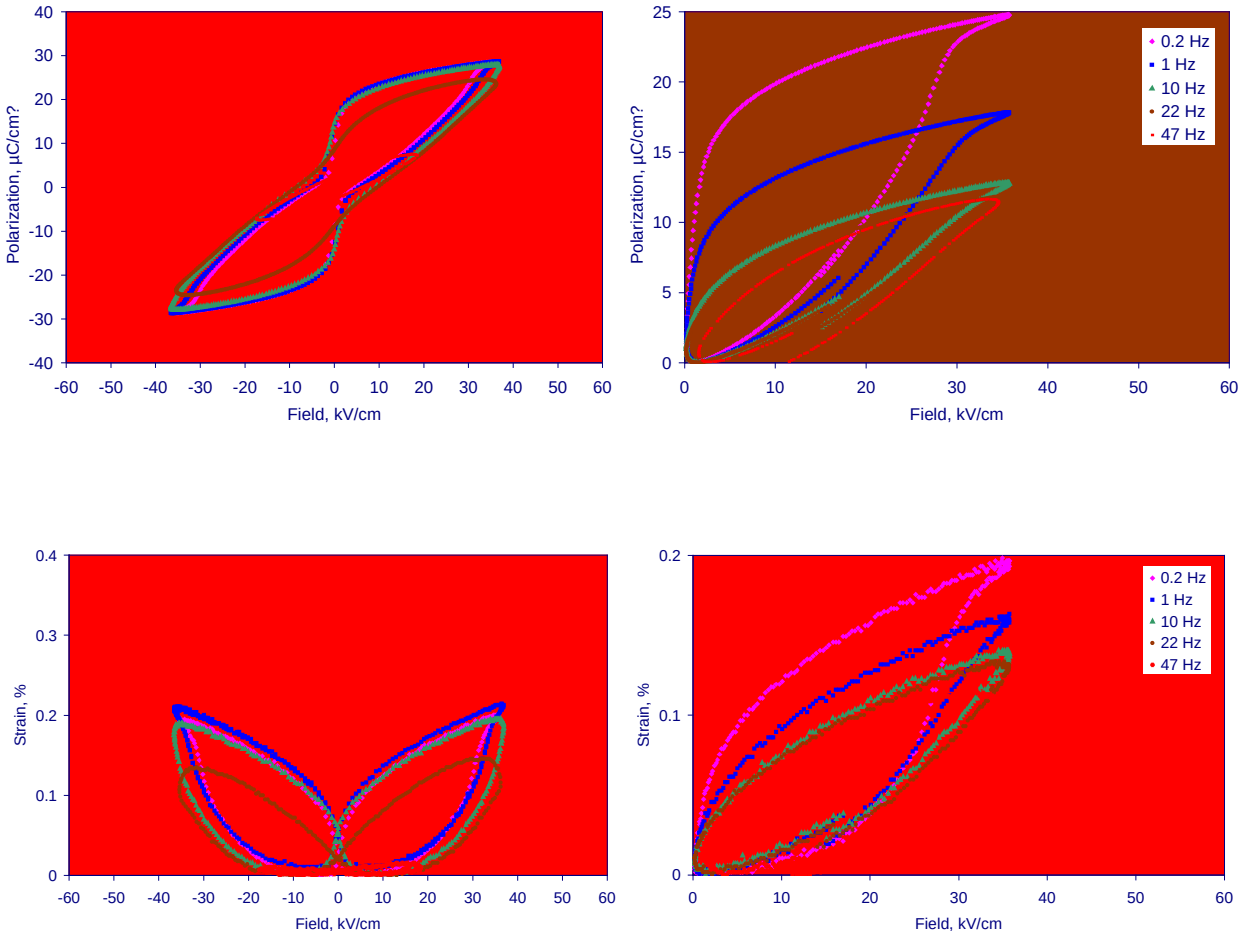

Figure 3.13. Electromechanical behavior of z4b16

The z4b16 sample shows high strain and high hysteresis. The shape of the hysteresis loop is “a pinched loop”—a sign of a field induced phase transition. Note four inflection points on the bipolar polarization loops.

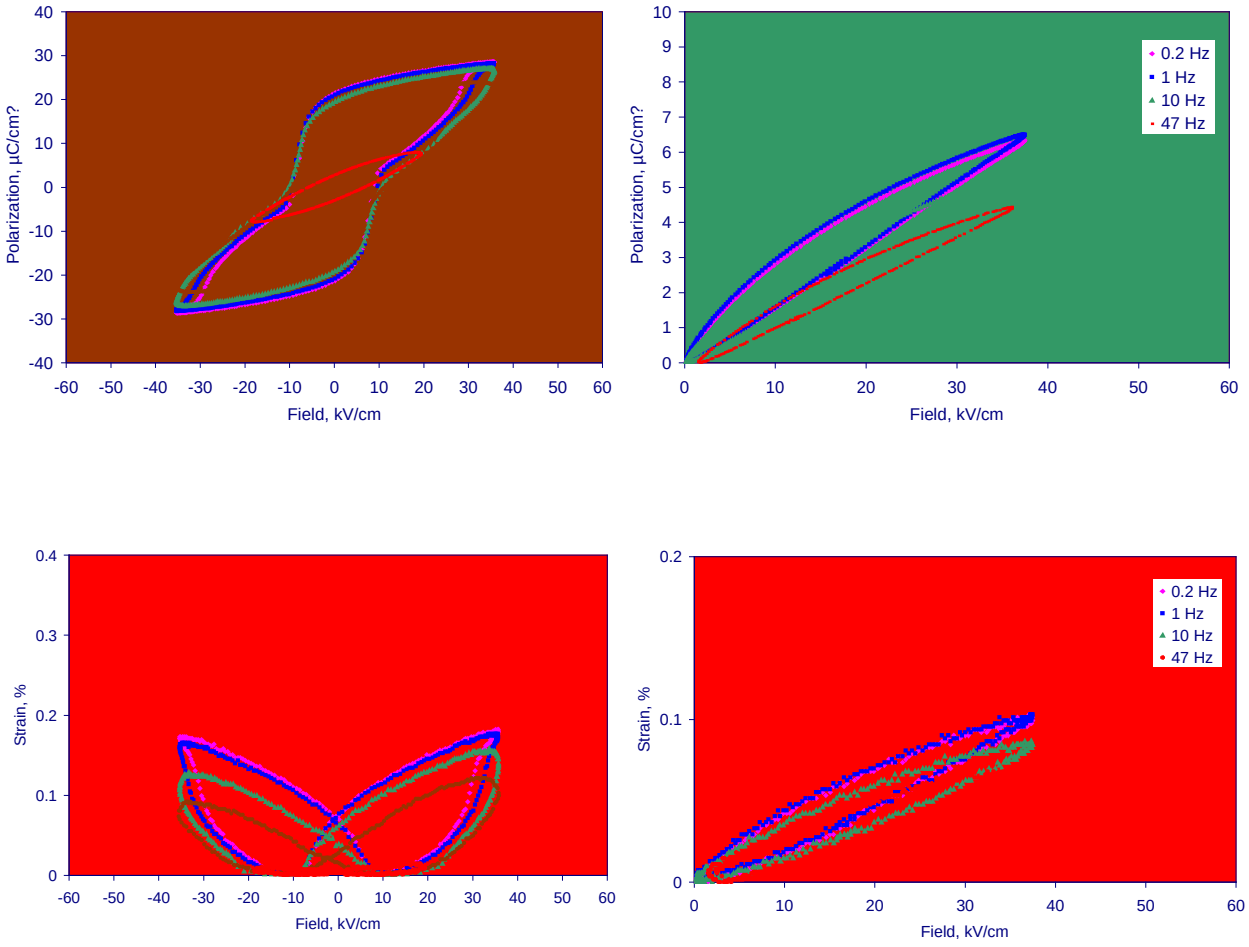

Figure 3.14. Electromechanical behavior of z4b18

The z4b18 sample exhibits substantial strain and hysteresis. The shape of the hysteresis loop is “a pinched loop”—a sign of a field induced phase transition. Note four inflection points on the bipolar polarization loops. Unipolar actuation exhibits relatively low hysteresis.

Compositional map of electrostrictive coefficient $Q = S / P^2$ and its 3D representation are given in Fig. 3.15. Note the peak at the z2b6.5 composition.

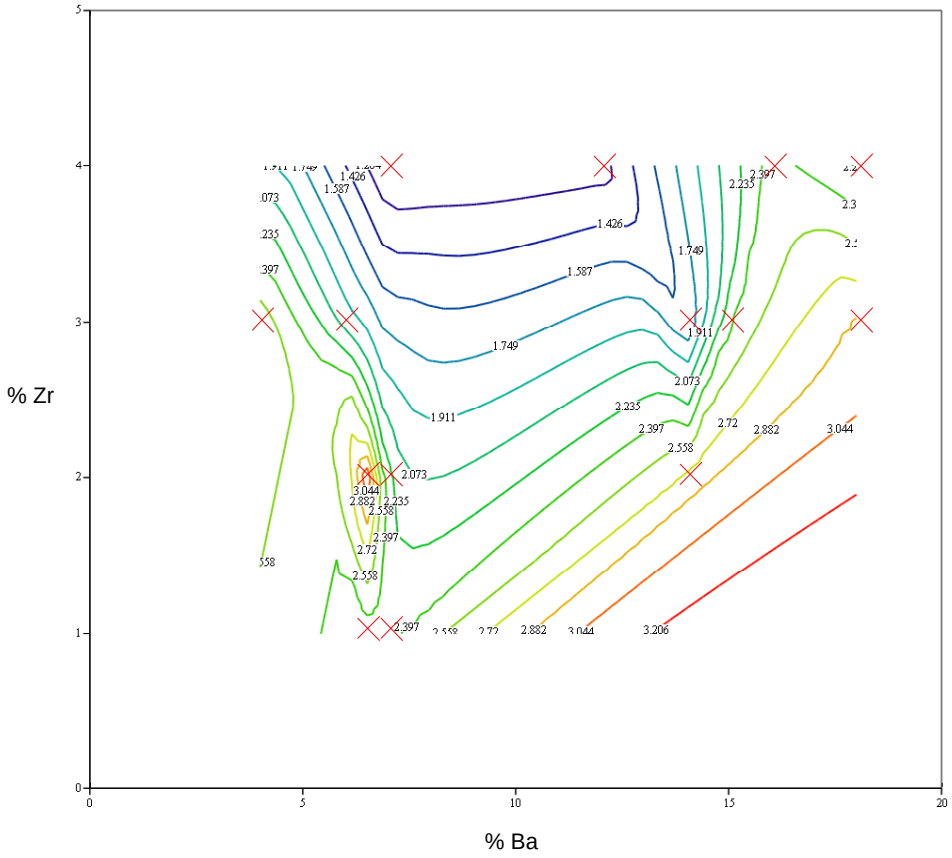

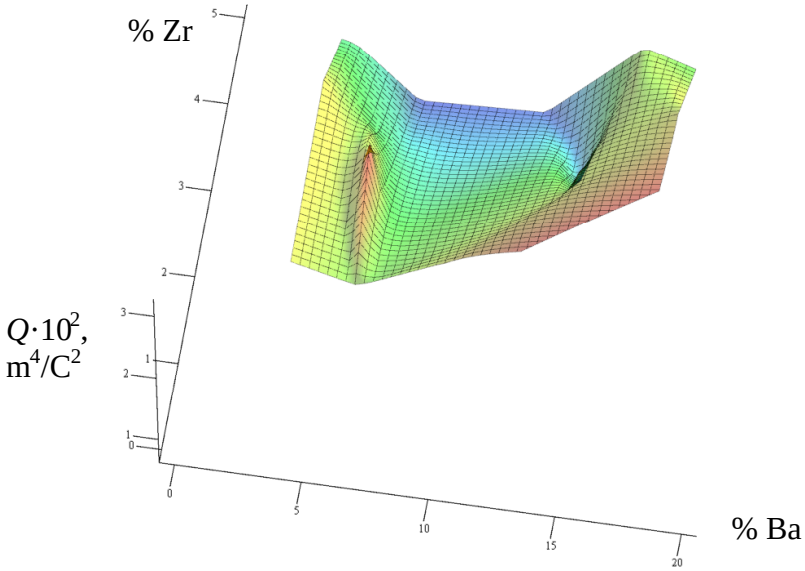

Figure 3.15. $Q \cdot 10^2$ (m^4/C^2) vs. Ba and Zr concentrations in BNBZT system. Studied compositions are shown by “x” marks.

Chapter 4

PHENOMENOLOGICAL MODELS AND COMPOSITIONAL EFFECTS

As one can see from the data presented in the previous chapter, the electromechanical response of polycrystalline samples in the BNBZT system is qualitatively diverse (depending on the composition), non-linear, hysteretic and frequency dependent. All this indicates a complicated shape of the profile of the free energy vs. polarization and its strong and complex dependence on the composition. Development of a phenomenological model capable of describing all types of time-dependent response in active materials is the main constituent of this work. In the first part of this chapter, a novel phenomenological model describing all aspects of the observed frequency dependent hysteretic electromechanical response is presented. In the second part, the compositional dependence of the polarization response to applied electric field will be analyzed by means of a free energy expansion with three composition dependent coefficients. This expansion provides the most compact description of the phase and dielectric properties dependence on applied field.

Electrorheological Model

Introduction

Hysteresis is the defining feature of ferroic materials. Thermodynamics does not allow any kind of hysteresis: the ultimate state of the system is the one with lowest free energy, regardless of any metastable minima. This fact urges us to use kinetics whenever we observe hysteresis. However, in the case of classical ferroic materials the hysteresis can be considered *static* in the sense that the potential barriers between free energy minima are high. On experimentally available time scales the static hysteresis is not time dependent. In contrast, relaxor materials [L. E. Cross, *Ferroelectrics* **151** 305 (1994)] have energy barriers that are comparable to k_BT and therefore can be traversed in observable times, spontaneously or under an applied field. This fact brings about *dynamic* hysteresis: there is a relaxation, i.e. non-instantaneous change of a material parameter

towards its equilibrium value in response to a change in an applied field. We believe that a broad distribution of potential barriers producing relaxation over many time scales can be represented by a mixture of static and dynamic hysteresis. As we show, the explicit inclusion of both is important for proper analysis and modeling of active materials behavior.

The theory of viscoelastic relaxation (strain vs. stress) is well-developed. Lakes has recently summarized the results of theoretical and experimental studies of viscoelastic solids, and describes relaxation time and its spectrum, mechanical loss tangent and its frequency dependence, and different mechanisms of viscoelastic behavior [R.S. Lakes, "Viscoelastic solids", *CRC Press*, Boca Raton (1999)]. In contrast, the time dependent response of active materials has received scarce coverage in literature: the description is usually limited to the dielectric loss factor tanδ, the main cause of which is assumed by Lakes to be a dc conductivity. Uchino separates losses in piezoelectric materials into interrelated dielectric, mechanical and piezoelectric ones [K. Uchino and S. Hirose, *IEEE UFFC Trans*., (accepted)]. This approach is valid only for small signal linear response and does not address the frequency dependence of the loss factors.

Many hysteresis models have been developed. The static hysteresis is well described by Preisach type models [D. Mayergoyz, "Mathematical models of hysteresis", *Springer-Verlag*, New York, (1991)]. These models do not cover dynamic response, therefore dynamic models of hysteresis have been suggested. Smith starts from unhysteretic response and adds terms reflecting resistance to the domain wall motion to obtain hysteresis [R. C. Smith. *Proc. SPIE – Internat. Soc. Optical Eng.* **3041**, 243 (1997)], whereas Piquette and Forsythe transform unhysteretic response to a hysteretic one by rotation of the response curve in an "inflated" space [J.C. Piquette and S.E. Forsythe, *J. Acoust. Soc. Am.* **106** 3317 (1999)]. In contrast, Chen and Montgomery developed a dynamic hysteresis model that assumes static hysteresis and obtains the dynamic response using a rate equation for the domain state parameter [P.J. Chen and S.T. Montgomery, *Ferroelectrics* **23**, 199 (1980)]. We expand the latter approach to incorporate also antiferroic and ferroelastic switching.

In order to be able to describe all conceivable time-dependent responses the present model generalizes rheology to describe relaxation in not only the viscoelastic response, but also: (1) polarization vs. electric field, (2) strain vs. polarization, (3) ferro- and antiferroelectric or ferroelastic domain switching under applied field and/or stress.

It should be noted that the present model does not follow a traditional equivalent-circuit approach. We believe this approach has substantial limitations in representing aspects of the electromechanical response. For example, it is quite problematic to represent a non-polar deformation that has orientation, but no unique direction, using only electrical parameters.

Assumptions and limitations

We assume electromechanical response to have in general both electrostrictive (ES) and ferroelectric/ferroelastic/antiferroelectric (FE/FEla/AFE) components. Materials parameters exist to describe each of these responses, and can be identified using experimental data and appropriate model.

For simplicity we consider excitation and response in one dimension only (along a single axis of interest), therefore all parameters are scalars. In addition:

- the material is idealized to have zero dc conductivity;
- the frequency of excitation is well below the resonant frequency;
- the temperature is constant;
- the piezoelectric strain is assumed to be instantaneous.

The last assumption is valid since the displacement of ions under an applied field without any structural rearrangement takes about 10^{-13} s, which is negligibly short compared to time constants of other responses. The piezoelectric response, however, does depend on the domain state. An unpoled (virgin) sample exhibits no piezoelectric effect, whereas a poled ferroelectric sample has a piezoelectric strain coefficient that depends on the degree of poling. Poling is quantifiable as the bias in the distribution of possible domain states.

To model time dependent responses, we use the simplest approach of rate equations with a single time constant as the kinetic parameter. To make the model more realistic (but more computationally intensive), a straightforward modification is to use a spectrum of time constants instead of a single value.

The time constants are as follows. Domain switching is known to be a relatively slow process. The model incorporates a switching time constant, τ_{sw}. Dielectric relaxation is characterized by a dielectric time constant, τ_d. The electrostrictive strain response in general can be

dynamically decoupled from (lag) dielectric polarization. To include the possibility of the strain lagging the polarization we introduce an electrostriction time constant, τ_{ES}. Finally, to describe the kinetics of stress-strain response in the absence of ferroelastic switching, we use elastic time constant, τ_{ela}.

Constitutive relations

First we develop constitutive relations for each of the relevant material responses. To denote equilibrium values we use the subscript *e*. Values corresponding to zero applied stress are marked with the superscript °.

Polarization

Equilibrium dielectric polarization is given by a non-linear odd function of the electric field *E:*

$$P_{d,e} = P_{satur} \tanh\left(\frac{E}{E_0}\right), \tag{4.1}$$

which becomes linear ($P_{d,e} = \chi E$, where $\chi = P_{satur} / E_0$ is the dielectric susceptibility) at low values of *E* compared to the normalization field (E_0) and saturates at the value of P_{satur} at high fields compared to E_0. Due to electrostriction, stress *T* affects E_0 according to the equation:

$$E_0 = E_0^\circ - 2QTP_{satur}, \tag{4.2}$$

where E_0° is E_0 at zero stress and *Q* is the electrostrictive coefficient.

The dielectric polarization current density is given by the kinetic equation:

$$i_d \equiv \frac{dP_d}{dt} = \frac{1}{\tau_d}\left(P_{d,e} - P_d\right), \tag{4.3}$$

where P_d is the instantaneous dielectric polarization.

In the presence of domain switching, the polarization is a function of the domain states. Chen and Montgomery described ferroelectric domain switching by *n*, the net fraction of dipoles pointing "up": $-1 \le n \le 1$. This parameter exhibits a static hysteresis, therefore we use a special form of the rate equation for *n*:

$$\frac{dn}{dt} = \frac{\beta - n|\beta|}{\tau_{sw}}, \tag{4.4}$$

where t is time and τ_{SW} is the switching time constant and $\beta(E, T)$ is the ferroelectric domain switching function that ranges from –1 to +1. A plot of β vs. E is given in Fig.4.1 and is analytically expressed by the following formula:

$$\beta = \tanh^3\left(\frac{E}{E_c}\right)^{2m-1}, \tag{4.5}$$

where E_c is the coercive field and m is a positive integer number that characterizes the abruptness of the switching function β in the vicinity of E_c. The coercive field in general depends on the stress. We use the simplest, yet physically plausible, form for this dependence

$$E_c = E_c^{\circ} \exp(T / T_{Ec}), \tag{4.6}$$

where T_{Ec} is the normalization stress and E_c° is the E_c at zero stress, therefore we can obtain indirectly (through E_c) the stress dependence of β.

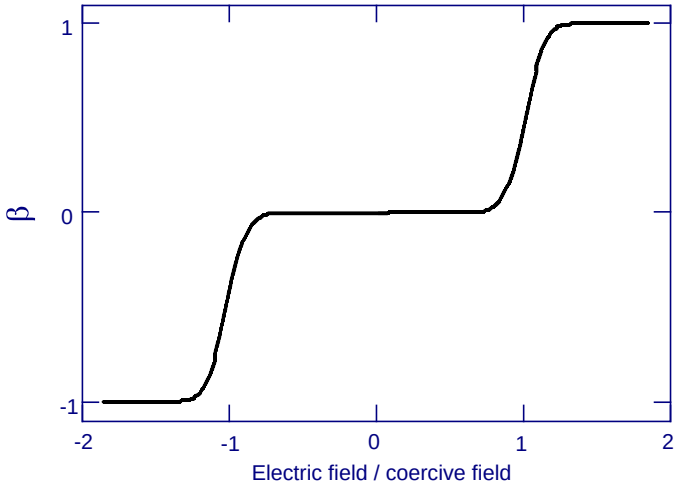

Figure 4.1 Ferroelectric domain switching function β. The electric field is given in the units of the coercive field

Using one domain state parameter n we can describe only 180° domain switching. In order to be able to describe also (1) non-180° domain switching, (2) ferroelastic domain switching and

(3) antiferroelectric behavior we introduce two domain state parameters of opposite sense n_p and n_n ("positive" and "negative"), that have correspondingly different switching functions

$$\beta_p(E) = \beta(E - E_t) \quad \text{and} \quad \beta_n(E) = -\beta(E + E_t). \tag{4.7}$$

These are obtained from the previously described $\beta(E)$ by the opposite shifts along the E-axis by E_t, the transition field, and changing the sign for the β_n. Evolution of n_p and n_n is described by equations analogous to Eq. 4.4. Again, to represent stress effects we assume the transition field E_t to depend exponentially on the stress T:

$$E_t = E_t^\circ \exp(T / T_{Et}), \tag{4.8}$$

where T_{Et} is the normalization stress and E_t° is the E_t at zero stress. By treating n_p and n_n separately we can calculate both the above-mentioned n and a new domain state parameter n_a, the fraction of material having zero polarization along the axis of interest:

$$n = (n_p - n_n) / 2 \quad \text{and} \quad n_a = -(n_p + n_n) / 2 . \tag{4.9}$$

The parameter n_a can represent the fraction of (1) the antiferroelectric phase, (2) ferroelectric domains with zero projection of polarization onto the axis of interest or (3) ferroelastic domains of one arbitrarily chosen configuration, e.g. those with shorter lattice parameter along the axis of interest. The use of both n and n_a expands the scope of the model. A ferroelectric material with only 180° domain switching or quasi-180° domain switching (e.g. a rhombohedrally distorted perovskite single crystal poled and actuated along the pseudocubic [001] direction [S.-E. Park and T.R. Shrout, *J. Appl. Phys.* **82** 1804 (1997)]) is just a special case with $E_t = 0$.

Polarization due to ferroelectric switching is given by:

$$P_F = nP_s , \tag{4.10}$$

where P_s is the spontaneous polarization. The total polarization is given by the sum: $P = P_F + P_d$ and the total current density is $i = dP / dt$.

Electrostriction

A well-known formula gives the equilibrium electrostrictive strain:

$$S_{ES,e} = QP_d^2 \tag{4.11}$$

and the following kinetic equation describes the instantaneous electrostrictive strain S_{ES} :

$$\frac{dS_{ES}}{dt} = \frac{1}{\tau_{ES}}(S_{ES,e} - S_{ES}), \tag{4.12}$$

where τ_{ES} is the electrostriction time constant.

Piezoelectric strain

The piezoelectric strain is proportional to the electric field E and the domain state parameter n, which can be considered also as the degree of poling with the sign indicating the poling direction:

$$S_p = ndE \tag{4.13}$$

where d is the piezoelectric strain coefficient of the fully poled material, equivalent to d_{33} in three dimensions. In general, d depends on the stress. Since actuators usually work under compressive stress, we have considered only compressive stress in this work. The compressive stress dependence of d is observed to (1) decrease monotonically with increasing compression or (2) show a maximum at a certain compression level [J. Zhao and Q. M. Zhang, *ISAF '96 Proc. Tenth IEEE Internat. Symp. App. Ferroelectrics.*, **2**, 971 (1996)]. A single equation giving both types of behavior is:

$$d = (d_{\max} - d_{\min}) \exp\left(-\left(\frac{T_{d\max} - T}{T_d} \right)^2 \right) + d_{\min}, \tag{4.14}$$

where $d_{\max}$ and $d_{\min}$ are maximum and minimum values of d ($d_{\min}$ is observed at high stresses), $T_{d\max}$ is the stress (positive or negative) at $d_{\max}$, and T_d is a normalization stress defining how fast d changes with increasing stress.

Elastic strain

Equilibrium elastic strain is given by Hooke's law:

$$S_{ela,e} = sT, \tag{4.15}$$

where s is the compliance, whereas the instantaneous elastic strain S_{ela} relaxes towards its equilibrium value according to the formula:

$$\frac{dS_{ela}}{dt} = \frac{1}{\tau_{ela}}(S_{ela,e} - S_{ela}), \quad (4.16)$$

where τ_{ela} is the elastic time constant. The compliance in general is anisotropic and depends on the n_a parameter, the simplest additive relation being $s = s_0 (1 - n_a) + s_1 n_a$, where s_0 and s_1 are compliances corresponding to $n_a = 0$ and $n_a = 1$ respectively.

Spontaneous strain

The following equation gives spontaneous strain S_{sp} due to non-180° switching of ferroelectric domains, AFE-FE phase transition or ferroelastic switching:

$$S_{sp} = n_a S_{cryst}, \quad (4.17)$$

where S_{cryst} is the crystallographic strain produced by complete switching from $n_a = 0$ to $n_a = 1$, which can be calculated from the appropriate lattice constants. For example, in a tetragonally distorted crystal with the axis of interest coinciding with the four-fold axis $S_{cryst} = 1 - a/c$, where a and c are the lattice constants.

The total strain has the four components described above:

$$S = S_{ES} + S_p + S_{sp} + S_{ela} \quad (4.18)$$

Simulations of pure cases of electromechanical response

The model is essentially a system of first order ordinary differential equations, therefore one needs to specify the initial conditions and integrate numerically the constitutive differential equations with the given material parameters in order to obtain a simulated response to applied electric field and stress.

We tested the model by simulating pure cases of known electromechanical responses and observing the effect of different time constants, all other parameters being held constant at values typical for electromechanically active perovskites. The general trend with increasing time constants was the inflation of hysteresis and “butterfly” loops indicative of the delayed response. The default conditions were: (1) 1 Hz frequency of an applied sinusoidal electric field, (2) no applied stress.

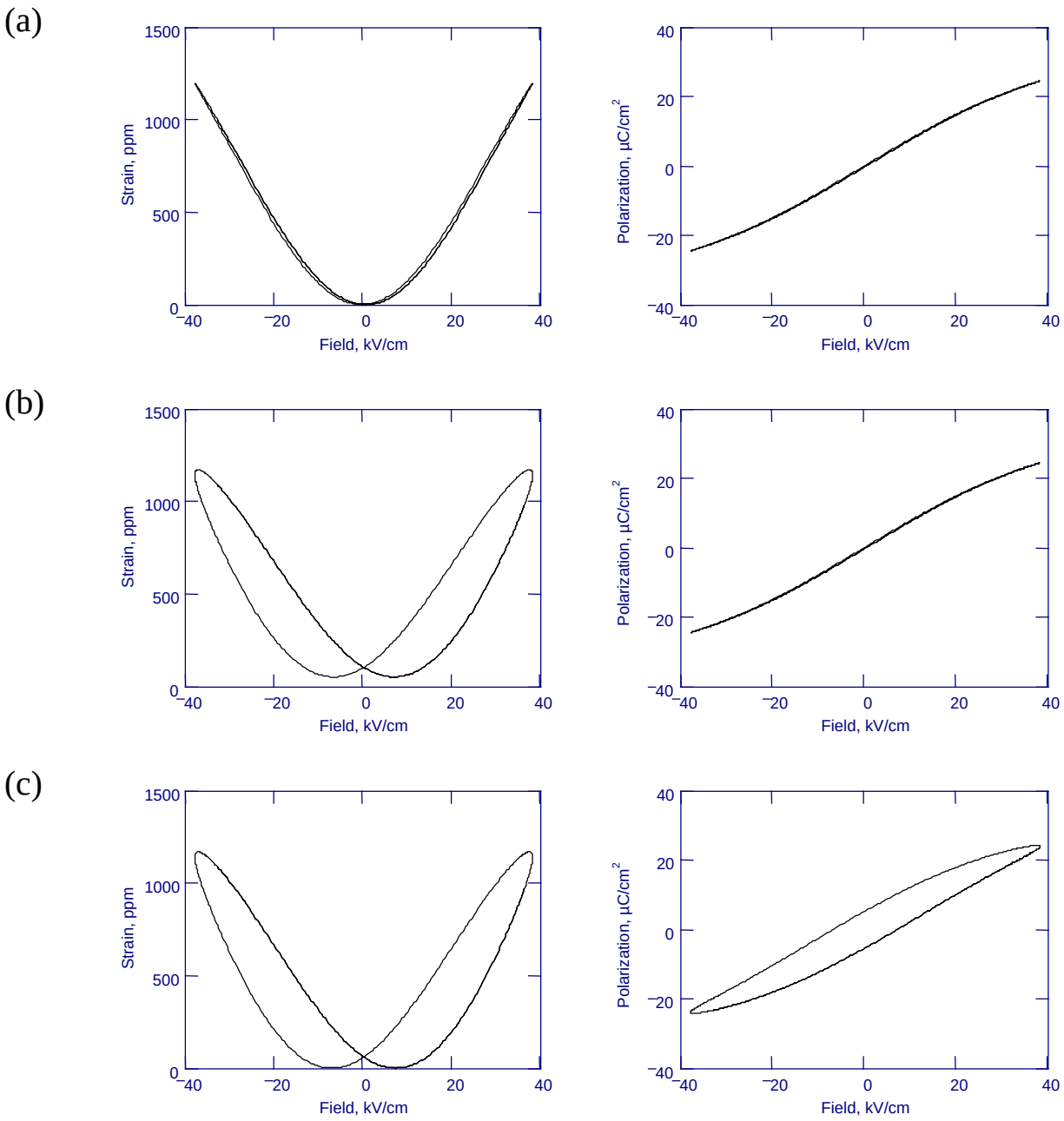

Figure 4.2. Simulated purely electrostrictive responses to 1 Hz sinusoidal electric field with different dielectric and electrostrictive time constants: (a) τ_d = 1 ms, τ_{ES} = 1 ms; (b) τ_d = 1 ms, τ_{ES} = 30 ms; (c) τ_d = 30 ms, τ_{ES} = 1 ms

Fig. 4.2 shows three examples of purely electrostrictive response with different τ_d and τ_{ES}. Note how the curves inflate as a result of increasing time constants: large τ_{ES} affects only the strain curve (Fig. 4.2b), whereas large τ_d affects both curves due to the polarization-strain coupling (Fig. 4.2c). It should also be noted that the inflated curves resemble ferroelectric behavior: the hysteresis loop has apparent remanent polarization and coercive field, and the strain curve has two distinct minima characteristic of a butterfly curve for a ferroelectric material. However, these features disappear at low frequencies. They could be easily confused with the static properties of a classical ferroelectric material if only limited (single frequency) data were available.

(a)

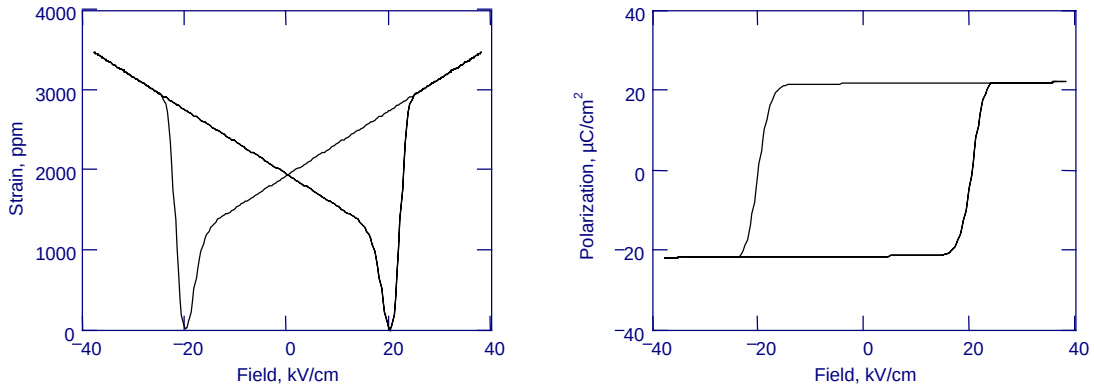

(b)

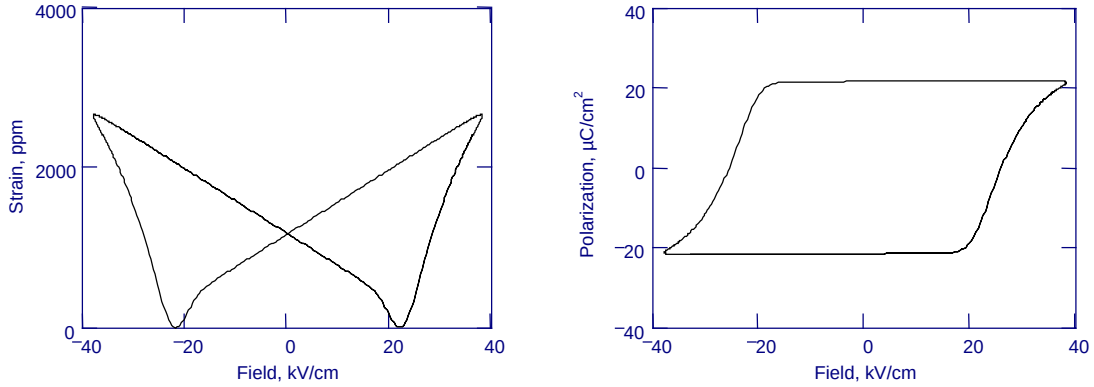

Figure 4.3. Simulated purely ferroelectric responses to 1 Hz sinusoidal electric field with different switching time constants: (a) τ_{sw} = 5 ms; (b) τ_{sw} = 40 ms.

Fig. 4.3 presents two examples of ferroelectric response with different τ_{sw}. When the switching time constant is large (Fig. 4.3b), the total strain is lower due to suppression of non-180° domain switching and the apparent coercive field is higher due to the slow switching kinetics. Simulations performed for different frequencies of the electric field and different time constants show that the effects of increasing time constants and increasing frequency are identical. In other words, the shape of the strain and polarization responses is determined by the dimensionless criterion $f\,\tau$, where f is the excitation frequency and τ is a time constant. The inflation of the hysteresis loops of a ferroelectric material as a result of increase in frequency of an applied ac electric field was also observed in Monte Carlo simulations [B. G. Potter et al., *J. Appl. Phys.* **87** 4415 (2000)].

(a)

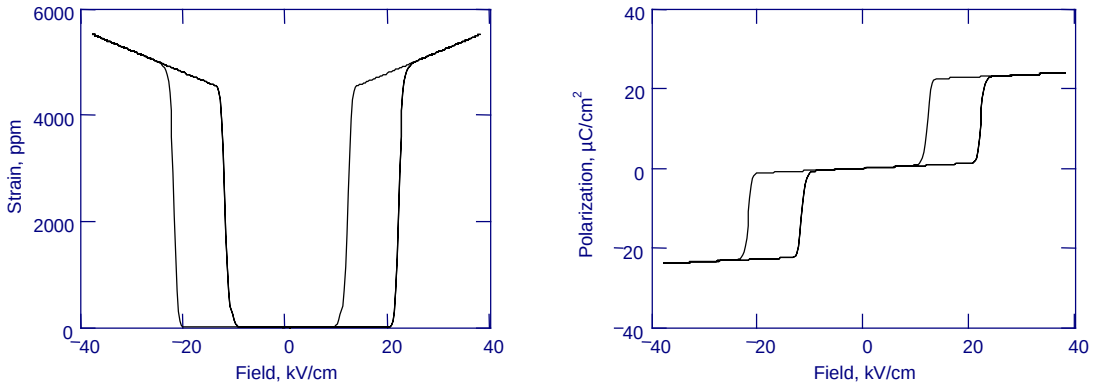

(b)

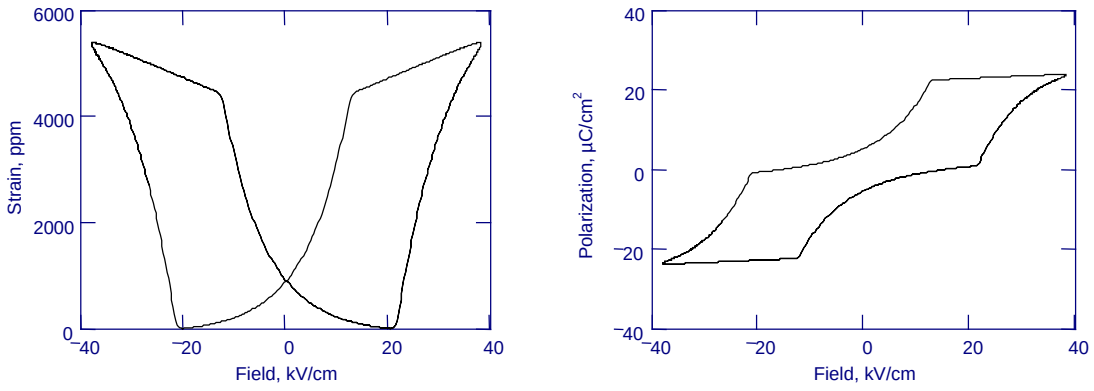

Figure 4.4. Simulated purely antiferroelectric responses to 1 Hz sinusoidal electric field with different switching time constants: (a) τ_{sw} = 5 ms; (b) τ_{sw} = 40 ms

Two examples of purely antiferroelectric response for different τ_{sw} are given in Fig. 4.4. It is clear from Fig. 4.4 that a large switching time constant (here, 40 ms) can convert classical antiferroelectric double hysteresis loop into a single pinched loop and make the strain curve resemble the butterfly curve of a ferroelectric material.

To demonstrate the effects of imposed stress on the electromechanical response of a ferroelectric material, observed in PLZT ceramics [C.S. Lynch, *Acta Mater.* **44** 4137 (1996)] we performed simulations for several levels of constant compressive stress (see Fig. 4.5). The simulated behavior was consistent with the experimental data of lynch for PLZT ceramics: increasing compression first increases the spontaneous strain due to enhanced non-180° domain switching and causes pinching of the hysteresis loop. At higher levels of compression the switching is completely suppressed and the material exhibits only electrostrictive behavior.

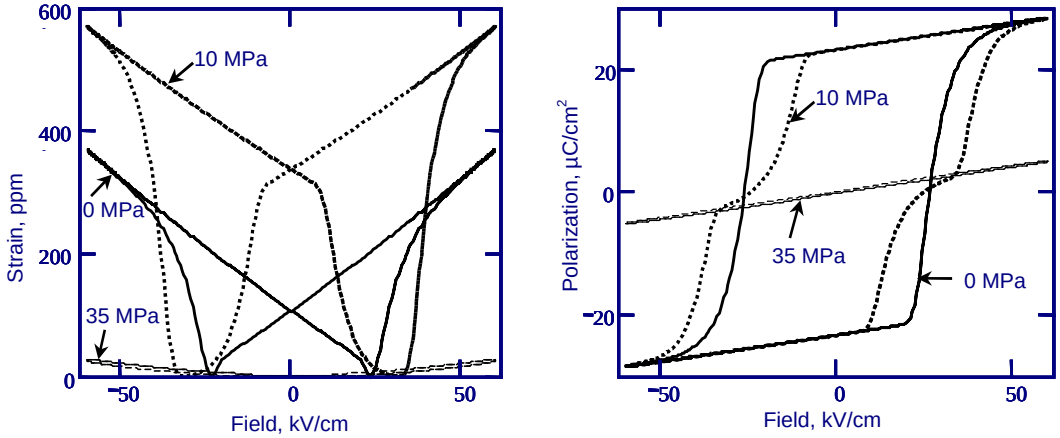

Figure 4.5. Simulated responses of a ferroelectric to 1 Hz sinusoidal electric field under 0, 10 and 35 MPa compressive constant stresses.

A common problem in modeling of hysteresis is the reproduction of minor loops (response to a small amplitude ac field applied in addition to a dc bias field). To test this ability of the presented model we combined two sinusoidal oscillations of the electric field: (1) low frequency, high amplitude and (2) high frequency, low amplitude. The response of a ferroelectric material is given in Fig. 4.6. The minor loops having realistic shape are present.

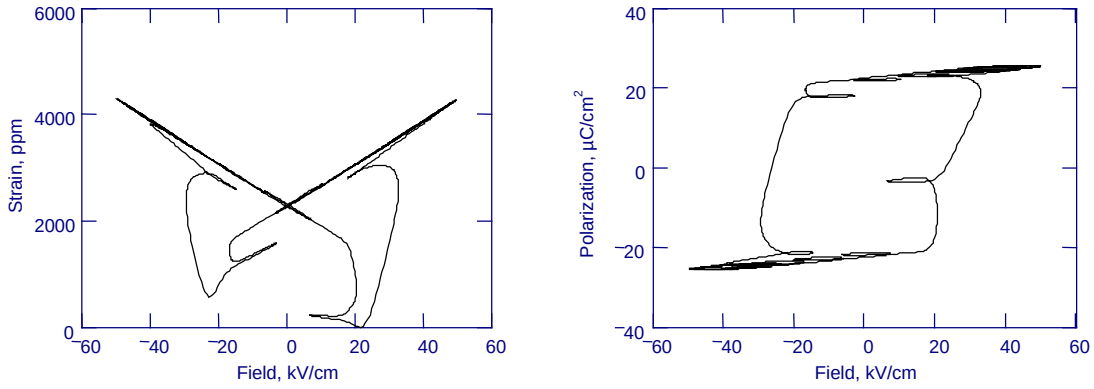

Figure 4.6. Simulated minor loops in the electromechanical response of a ferroelectric material.

Compositional Maps of Model Parameters

To identify the model parameters giving the best fit to the experimental data we used the following approach. Values of certain parameters (P_{satur}, P_s, E_0, E_c, E_t, Q, d) were first estimated graphically from the experimental plots. The initial estimate of crystallographic strain $S_{cryst,0}$ = 0.14% was obtained from the pseudocubic *c/a* ratio of the tetragonal phase of NBT [G.O. Jones and P.A. Thomas, *Acta Cryst.* **B58**, 168-178 (2002)]. The time constants were first taken to be zero and then increased if adjustment of other parameters was insufficient. The initial value of the abruptness parameter *m* was 3. All initial values were adjusted manually to give the best least squares match. While this procedure produced satisfactory results for Ba-doped NBT single crystals [A.N. Soukhojak and Y.-M. Chiang, *J. Appl. Phys*. **88** [11] 6902-6909 (2000)], for BNBZT polycrystals refinement of certain parameters had a very poor convergence: the goodness of fit was practically insensitive to changes in those parameters. Especially problematic was the separation of static and dynamic hysteresis: most of the tested BNBZT samples had both types of hysteresis present in comparable quantities. Another hampering factor was wide distribution of time constants: all simulated frequency dependencies were severely exaggerated by the limitation of the model to a single value of time constants. Below we present compositional maps of those parameters that had satisfactory convergence. Due to the above exaggeration of frequency dependence, we used the 0.2 Hz data as the fitting target.

% Zr

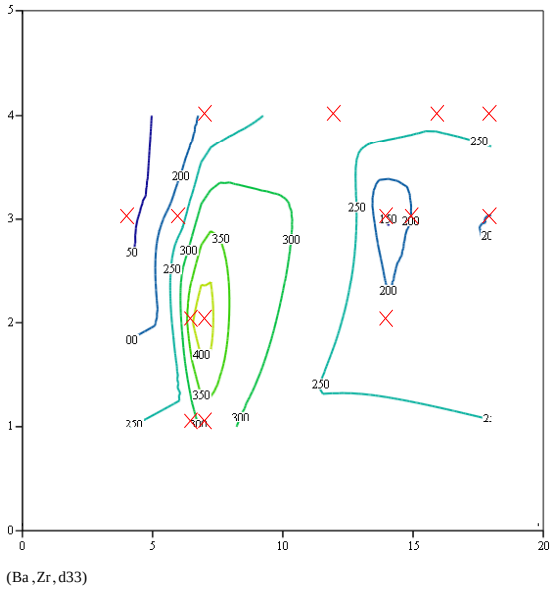

% Ba

Figure 4.7. Compositional map of piezoelectric strain coefficient d_{33}, pC/N. Studied compositions are shown by "x" marks. Conditions: room temperature, unipolar high field (>30 kV/cm) at 0.2 Hz, 1 MPa compressive prestress.

Piezoelectric strain coefficient d_{33} is one of the most important parameters of any electromechanically active material. Fig. 4.7 clearly demonstrates an elongated along MPB peak of d_{33} at the composition z2b7. Note that it almost coincides with the composition exhibiting peak electrostrictive coefficient (Fig. 3.15).

% Zr

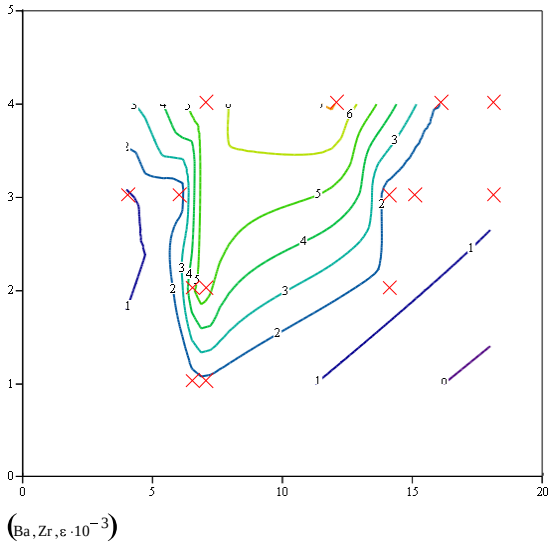

% Ba

Figure 4.10. Compositional map of permittivity, $\varepsilon \cdot 10^{-3}$. Studied compositions are shown by "x" marks. Conditions: room temperature, unipolar high field (>30 kV/cm) at 0.2 Hz, 1 MPa compressive prestress.

Permittivity (Fig. 4.10) has a ridge along 7 % Ba with highest values at high Zr concentrations. The ridge corresponds to the MPB.

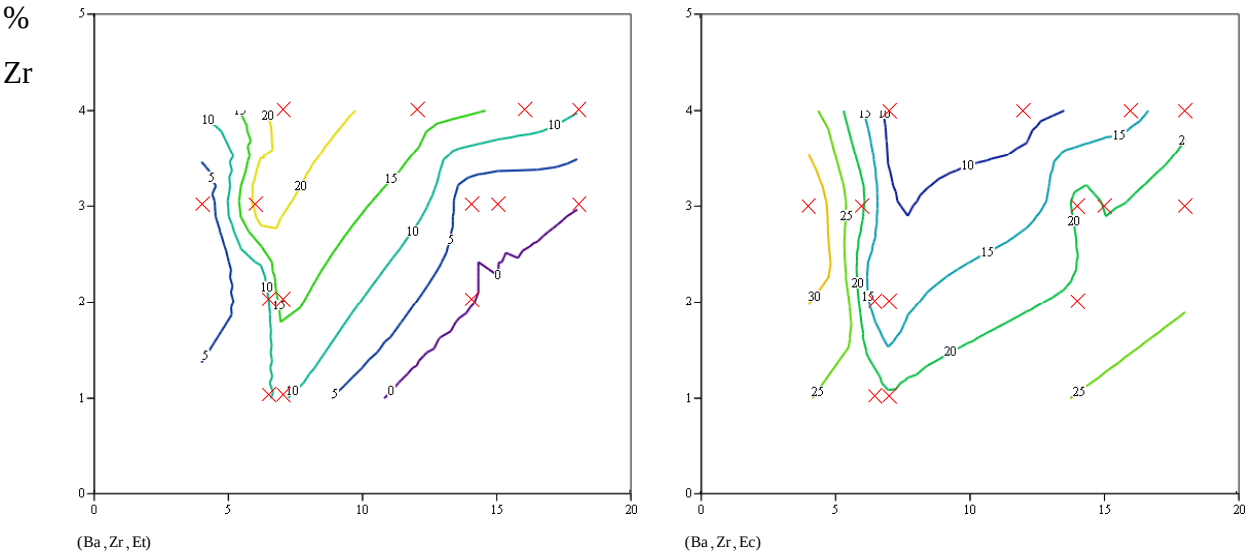

Figure 4.11. Compositional maps of transition field E_t (left) and coercive field E_c, kV/cm. Studied compositions are shown by "x" marks. Conditions: room temperature, bipolar high field (>30 kV/cm) at 0.2 Hz, 1 MPa compressive prestress.

Fig. 4.11 maps the compositional dependence of shape and width of the polarization hysteresis loop: higher E_t produces a more pinched loop, whereas higher E_c produces wider loops. These two parameters are related to well-pronounced and incipient minima on the free energy vs. polarization profiles. This will be shown in the second part of this chapter.

Presence of both dielectric and switching time constants complicates presentation of hysteresis during a unipolar actuation, a practically important characteristic describing heat generation during operation of an actuator. Therefore, we present the compositional dependence of strain and polarization hysteresis during a unipolar actuation by mapping dimensionless parameters called relative hysteresis of polarization and strain: $H_P = \Delta P / P_{max}$ and $H_S = \Delta S / S_{max}$, where ΔP and ΔS are the maximum differences between two branches of polarization and strain loops and P_{max} and S_{max} are the maximum values of polarization and strain during the unipolar cycle. Fig. 4.12 presents compositional dependences of relative hysteresis for 1 Hz.

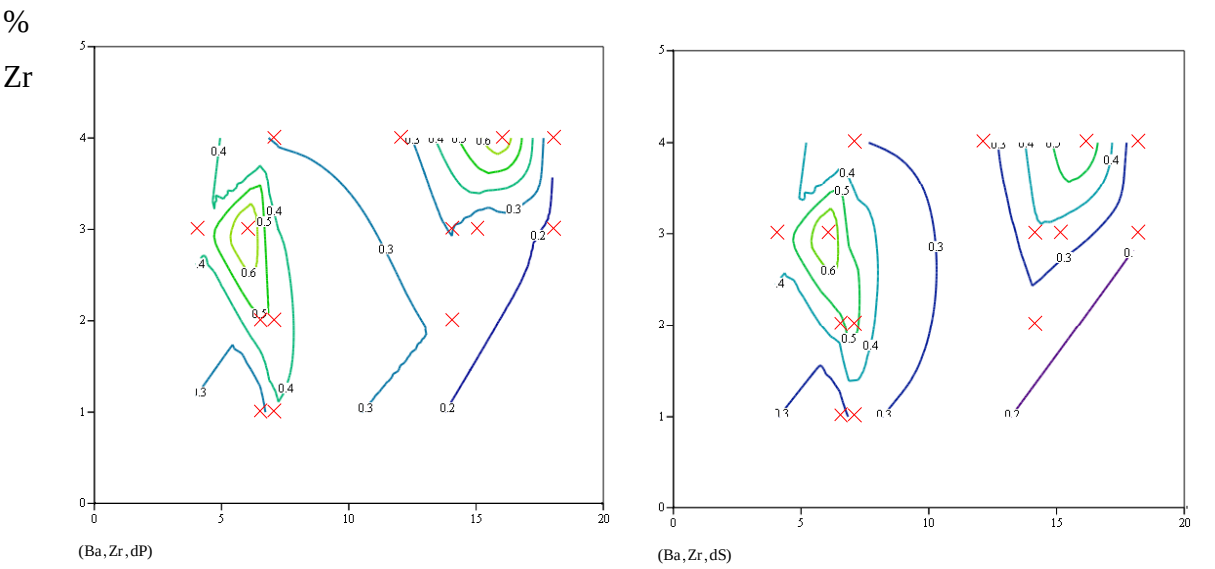

Figure 4.12. Compositional maps of relative hysteresis of polarization H_P (left) and strain H_S during 1 Hz unipolar actuation. Studied compositions are shown by "x" marks. Conditions: room temperature, bipolar high field (>30 kV/cm) at 0.2 Hz, 1 MPa compressive prestress.

Fig. 4.12 shows that hysteresis of polarization and strain is practically the same. This is consistent with our earlier observation that in the tested samples electrostrictive relation $S = QP^2$ holds at all frequencies, Q being frequency independent. Unfortunately, the peak of piezoelectric properties almost coincides with the peak of hysteresis. This indicates that the actuation mechanism of the highest strain compositions is not purely intrinsic and involves some sort of domain switching or a field forced phase transition. Both of them involve overcoming potential barriers, which inevitably causes hysteresis. The dependence of these barriers on composition is revealed in the following part.

Free Energy Expansion

Landau expansion of free energy in terms of order parameters have been successfully employed to describe multifarious phase transitions. In this part, we show how complex and diverse electromechanical behavior of the BNBZT system can be represented by three adjustable parameters, namely coefficients of the free energy expansion.

We follow classical route to describe ferroelectric 1st order phase transition and expand polarization dependent free energy in terms of even powers of polarization up to the 6th power:

$$U(P) = aP^2 + bP^4 + cP^6. \quad (4.19)$$

The 6th power polynomial is required to capture a field forced phase transition manifested by a pinched hysteresis loop since we need local minima at both zero and non-zero polarization in order to have a metastable polar phase that becomes stable only at high fields. If the hysteresis loop is not pinched it will suffice to have only two non-zero coefficients: *a* and *b*. In any case, the highest power term coefficient has to be positive to have a stable (bounded) polarization.

In order to find the electric field dependences of polarization, we need to perform the Legendre transformation and obtain the following expression for the field (E) dependent free energy:

$$G(E) = U(P) - EP \quad (4.20)$$

For any given value of E, equilibrium is characterized by the value P that minimizes G. The expression for G is too complex to find its minimizers analytically. Therefore, a numeric procedure has to be used to find field dependence of equilibrium polarization. Since there can be only one global minimum of G, no hysteresis can exist for the equilibrium value of P. In order to reproduce the observed hysteresis, we need to find P values of *local* minima of G as a function of E. Since the G function is a polynomial, this function can be multivalued. The easiest way to handle this complication is to use a necessary condition for a minimum, i.e. partial derivative of G with respect to P being zero. From this condition we immediately obtain:

$$E = 2aP + 4bP^3 + 6cP^5 \quad (4.21)$$

If we plot this equation as P vs. E we will get an envelope of the hysteresis loop (Fig. 4.12). All branches of this curve with positive slope will correspond to local minima. When a branch

bends and the slope changes its sign, the corresponding local minimum becomes an inflection point and the system jumps towards the closest local minimum of *G*.

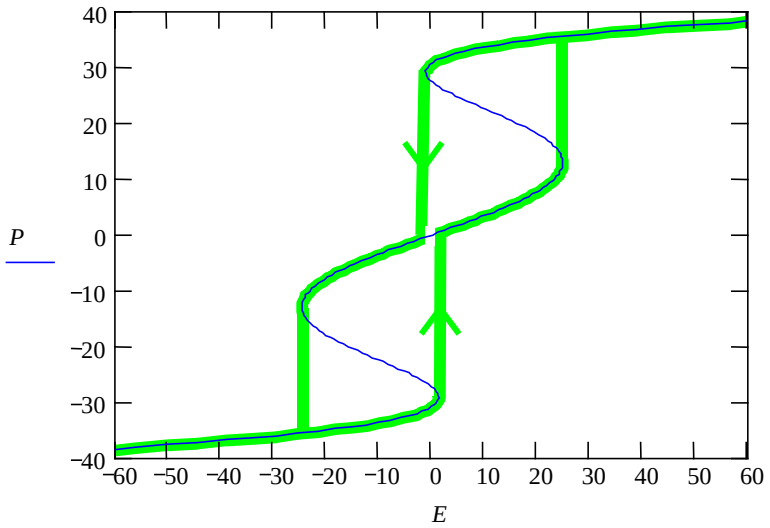

Figure 4.12. Construction of hysteresis loop (thick line) from the Eqn. 4.21 (thin line).

The strain is calculated using the electrostrictive relation $S = QP^2$. The hysteresis plot on Fig. 4.12 is, of course, ideal. In reality, transitions from one local minimum to another happen over a range of fields due to defects and inhomogeneities. Besides, grains in a polycrystal having different orientations switch at different fields. This spread of switching fields causes a smooth hysteresis loop with slopes much lower than those of an ideal single crystal.

By adjusting *a, b, c* and using the values of *Q* from the *S* vs. P^2 plots it was possible to adequately describe the electromechanical response of all tested samples except for z2b6.5, which did not reach saturation. In order to minimize kinetic effects we used the lowest frequency (0.2 Hz) data to perform the fitting. Below (Fig. 4.13-16) we present comparison of experimental data (points) and envelope curves obtained by plotting Eqn 4.21 for the adjusted values of *a*, *b*, and *c*.

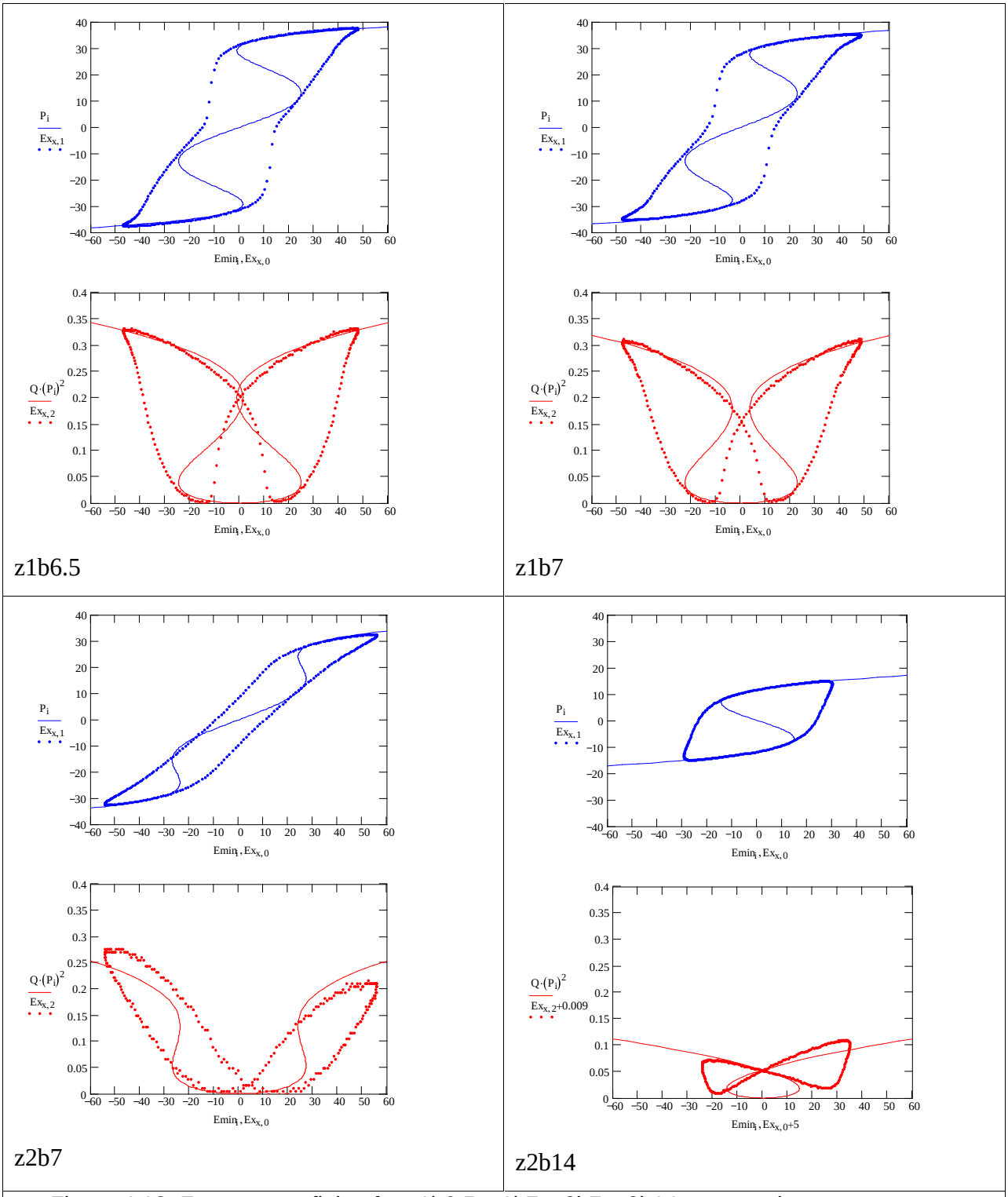

Figure 4.13. Free energy fitting for z1b6.5, z1b7, z2b7, z2b14: *P*-top, *S*-bottom

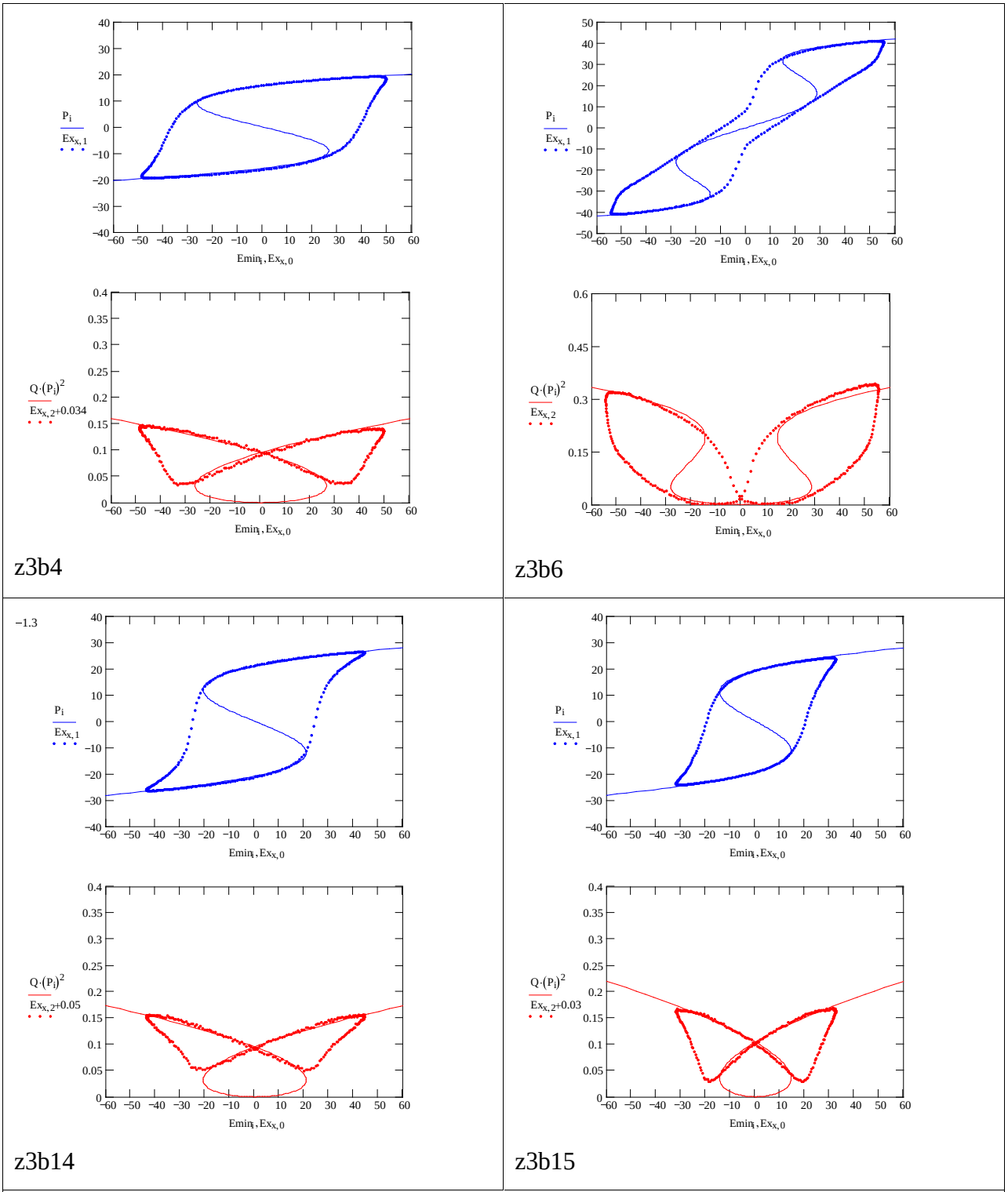

Figure 4.14. Free energy fitting for z3b4, z3b6, z3b14, z3b15: *P*-top, *S*-bottom

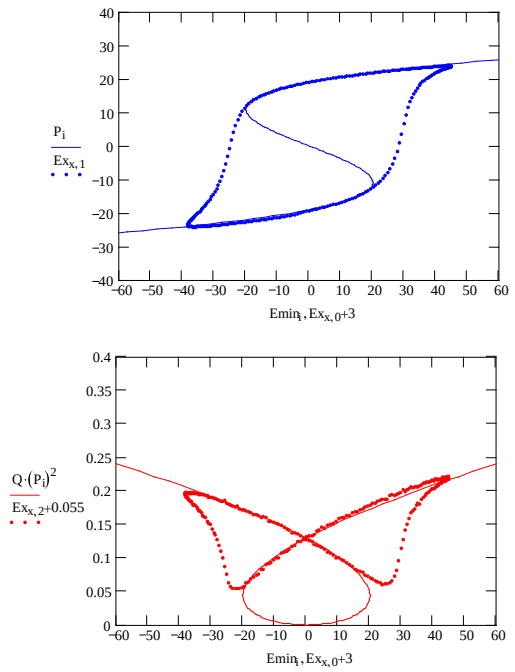

z3b18

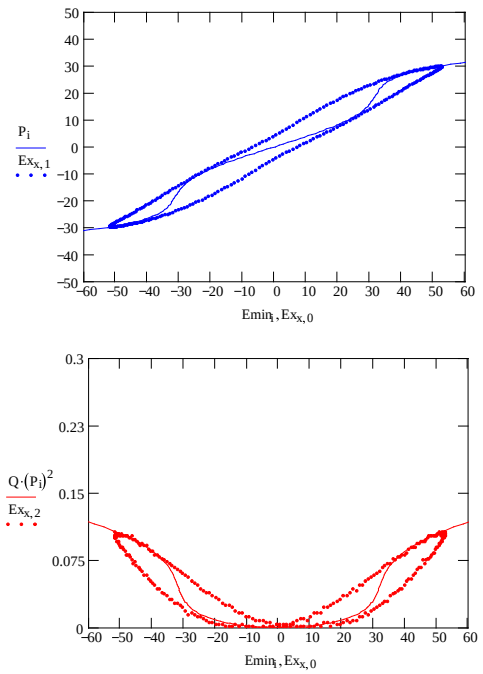

z4b7

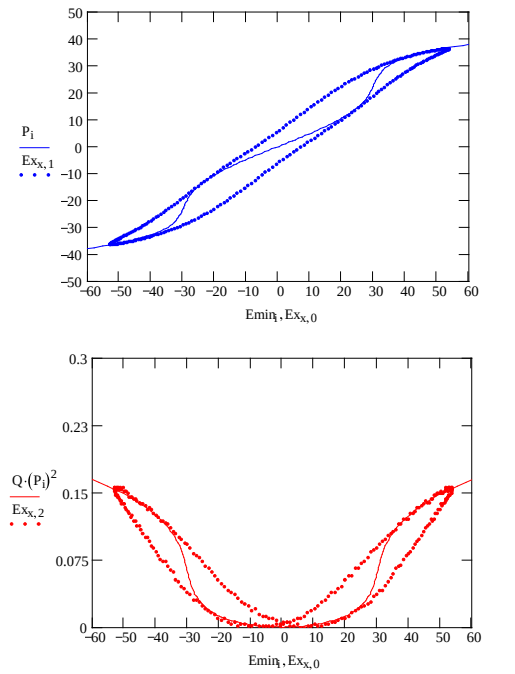

z4b12

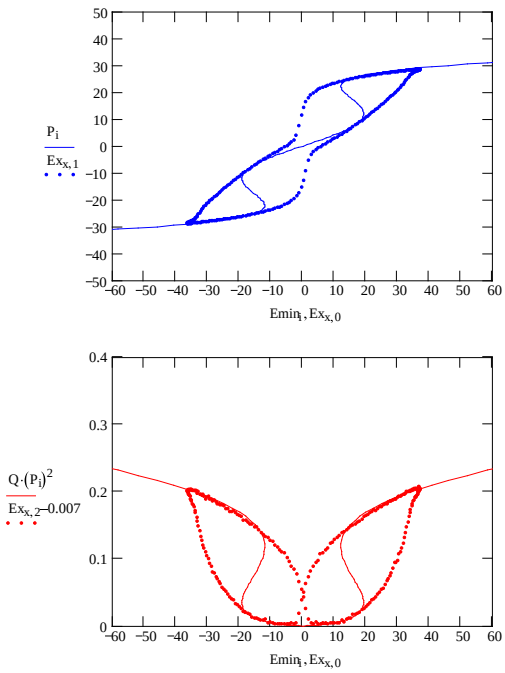

z4b16

Figure 4.15. Free energy fitting for z3b18, z4b7, z4b12, z4b16: *P*-top, *S*-bottom

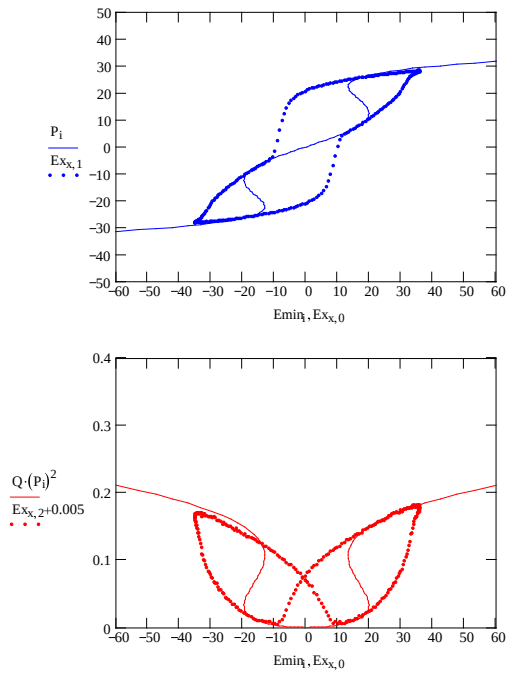

z4b18

Figure 4.16. Free energy fitting for z4b18: *P*-top, *S*-bottom

The free energy expansion coefficients are given in Table 4.1 and graphically presented in Fig. 4.17. The units of coefficients (hidden for clarity in this work) correspond to *P* values expressed in μC/cm^2 and *E* values expressed in kV/cm. The free energy units are kJ/m^3.

Table 4.1. Values of the free energy expansion coefficients

% Zr	**% Ba**	***a***	***b* · 10^3**	***c* · 10^7**
1	6.5	1.50	-1.80	7.10
1	7	1.38	-1.70	7.32
2	7	1.42	-1.38	6.70
2	14	-1.60	5.70	0
3	4	-2.20	4.50	0
3	6	1.37	-1.08	3.40
3	14	-1.30	1.50	0
3	15	-0.97	1.30	0
3	18	-1.37	1.90	0
4	7	1.34	-1.00	5.50
4	12	1.07	-0.57	2.20
4	16	1.27	-1.90	12.00
4	18	1.27	-1.80	11.00

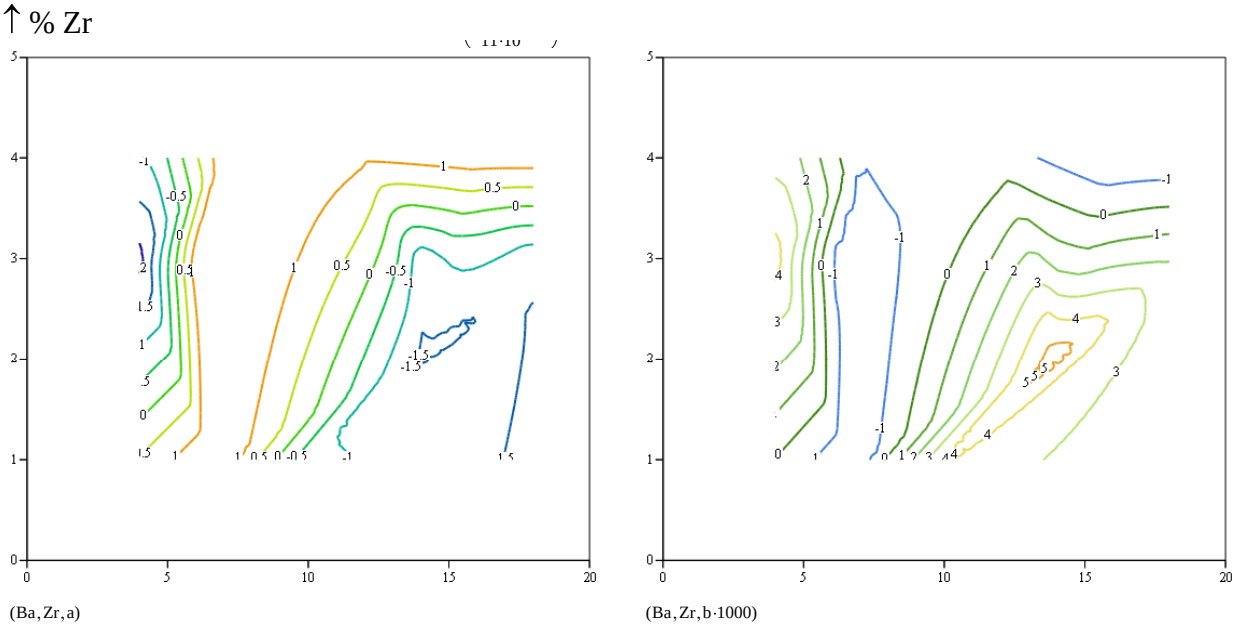

Figure 4.17. Compositional maps of free energy expansion coefficients: a (top left), $b \cdot 10^3$ (top right), $c \cdot 10^7$ (bottom left)

Analysis of compositional maps of the free energy coefficients in separation does not bear much meaning since it is the interplay of coefficients in the Eqn 4.19, not their separate values, that gives rise to “shoulders“ and minima on the free energy vs. polarization profiles. We have to analyze the dependence of entire profiles of the free energy vs. polarization on the composition.

There is no way to present on one plot dependence of the free energy profile on both Ba and Zr concentration, therefore Fig. 4.18 consists of four plots of the free energy U vs. % Ba and P for different % Zr. U is an even function of P, therefore only $P > 0$ half of profiles are plotted in Fig. 4.18.

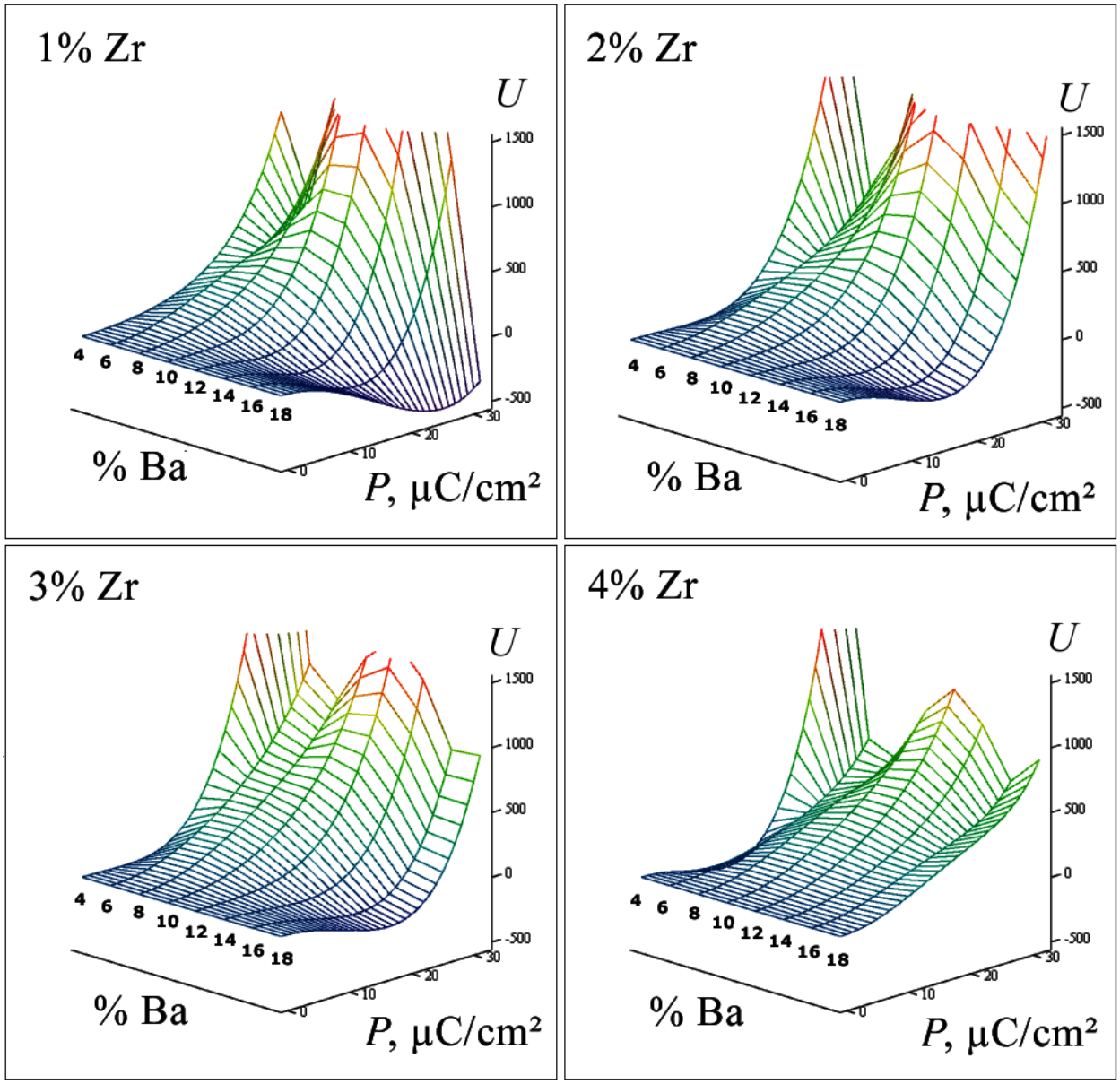

Figure 4.18. Compositional dependence of the free energy U [kJ/m^3] vs. polarization P profiles

"Shoulders" on the *U* vs. *P* profiles presented in Fig. 4.18 correspond to field forced phase transitions manifested as pinched loops, whereas minima of the profiles at non-zero *P* correspond to stable ferroelectric phases exhibiting classical hysteresis loops. MPB is manifested by anomalies (ridges at low *P*, which become troughs at high *P*) at about 6-8% Ba going almost parallel to the *P*-axis.

Analysis of Compositional Maps

All compositional maps in this work reveal the MPB between rhombohedral and tetragonal phases, which goes approximately along 7% Ba line and gradually vanishes when Zr concentration reaches 4%. The general trend at fixed Zr concentration is suppression of ferroelectric minimum at Ba concentrations around 6-7 %. This is explained by the peak of distortional frustration of the system around the MPB. The general trend at fixed Ba concentration is monotonic suppression of ferroelectric minima (up-lifting of the minima to be exact) by turning them first into "shoulders" and then elimination with increasing Zr concentration. This trend is explained by the fact that Zr^{4+} is significantly larger than Ti^{4+}, therefore the former suppresses the possibility of "rattling" of the B-cation in the octahedral cage of oxygen anions. This "rattling" is the classical cause of ferroelectricity in perovskites.

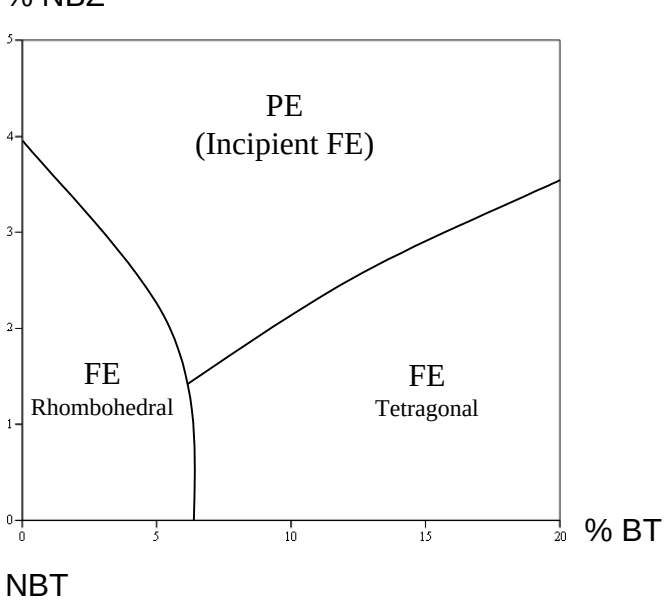

Figure 4.19. Phase diagram based on the electromechanical behavior of polycrystalline BNBZT samples. Phases: PE—paraelectric, FE—ferroelectric.

The best picture of the phases present in the studied part of the NBT-BT-NBZ quasi-ternary system can be obtained from Fig. 4.11. The latter clearly shows how paraelectric phase (high E_t, low E_c) field protrudes down along the MPB separating two ferroelectric phase (low E_t, high E_c) fields (see Fig. 4.19). It should be noted that the observed paraelectric phase has a complex free energy vs. polarization profile, which gives rise to pinched hysteresis loops. Due to the presence of "shoulders" on the free energy vs. polarization profiles this phase can be called "incipient ferroelectric": it displays static hysteresis, however the high polarization phase is not stable when no electric field is applied.

Phase diagram in Fig. 4.19 can also be obtained if we plot boundaries between compositions that exhibit global minima of the free energy U (Fig. 4.18) at non-zero values of polarization (ferroelectric phases) and those with global minimum of U at $P = 0$ (paraelectric phase). The equivalence of this approach to the above-described one using Fig. 4.11 comes from the fact that the transition field E_t is non-zero (pinched hysteresis loop) only if there is a local minimum or "shoulder" of the free energy U at non-zero polarization and also a minimum at $P = 0$. Ferroelectric phases have global minima at non-zero P and no local minima at $P = 0$.

A peculiar feature of MPB in the BNBZT system found in this work is that it does not just suppress the ferroelectric minima of U vs. P profile, but rather "redistributes" the free energy over a large range of polarizations so that the MPB U vs. P profile has lower curvature than neighboring compositions. Indeed, Fig. 4.18 illustrates how, with increasing P, the MPB U vs. P profile first "ridges up" above the neighboring compositions and then "digs through" the rising slopes of neighboring U vs. P profiles. The overall result is a flatter free energy profile over a large range of polarization.

We believe the flatness of U vs. P profile to be the primary reason for high electromechanical response of the MPB compositions. The most plausible structural origin of this flattening is the distortional frustration of the system between $<111>_{pseudocubic}$ and $<001>_{pseudocubic}$ directions for spontaneous polarization. When total energy minima along these directions in the polarization space are close, the barrier between them is low. This low barrier can be traversed by the system spontaneously by means of thermal fluctuations. As a result, the configurational entropy becomes a winning factor, individual displacements are not ordered and the total energy has to assume a

higher value due to the interaction term penalty (Eqn. 1.1). Additional flattening comes from the A-cation disorder creating strong internal random fields due to difference in charges of the A-cations. These random fields disrupt long range interaction and prevent deep total energy minima at any point in the polarization space. We believe this disruption to be the primary reason for enhanced electromechanical response of relaxors compared to classical ferroelectrics.

The tricritical point discussed in the first chapter is formed at the termination of the MPB, when Zr concentration is sufficient to suppress ferroelectric minima on both rhombohedral and tetragonal sides of the boundary and thus eliminate the qualitative difference between orientations of the polarization vector ($<111>_{pseudocubic}$ for rhombohedral and $<001>_{pseudocubic}$ for tetragonal) by reducing its magnitude to zero. At the tricritical point, when ferroelectric minima disappear, the free energy profile has the lowest curvature. This causes the electromechanical response to reach its maximum since the system is in the most susceptible to external fields state when its free energy vs. order parameter profile has the lowest curvature.

Chapter 5

MICROSCOPY AND MECHANISMS

Frequency dependence of electromechanical response of the tested BNBZT compositions should have a structural origin. Usually time dependent response is caused by a relaxation of metastable states into stable ones. In case of classical ferroelectrics, it has been known almost since the discovery of ferroelectricity that domain switching is not instantaneous due to limited mobility of domain walls. Ferroelectric domain walls cannot move with the velocity of sound because of defects that "pin" the domain walls by creating potential barriers for their motion. As a result, domain walls, experiencing driving force from an applied electric field that exceeds coercivity, have to wait for a large thermal fluctuation to overcome potential barriers created by the pinning sites. This waiting limits the macroscopic domain wall mobility.

We performed optical and transmission electron microscopy (TEM) on a number of BNBZT samples in order to elucidate the structural origin of the observed relaxation and shed some light on the mechanism of high strain actuation.

Optical Observations

A typical BNBZT single crystal after cutting and polishing is shown in Fig. 5.1.

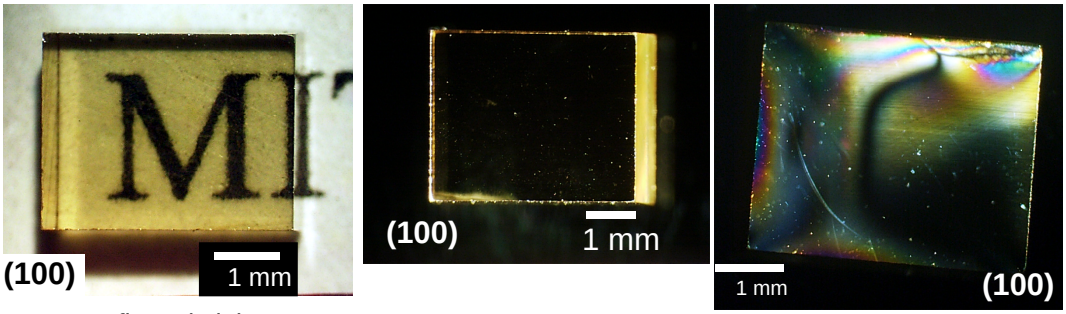

Fig. 5.1. Optical images of z3b6 single crystal

It should be noted that the domain structure of BNBZT single crystals or absence thereof are very sensitive to compositional variation. It will be illustrated by the following images. Sometimes in the same crystal clear and cloudy regions can be found (Fig. 5.2a). The cloudy regions under larger magnification reveal domain structure (Fig. 5.2b), whereas clear regions of that crystal have uniform extinction when rotated in cross-polarized light, which is a sign of a single domain state.

a) b)

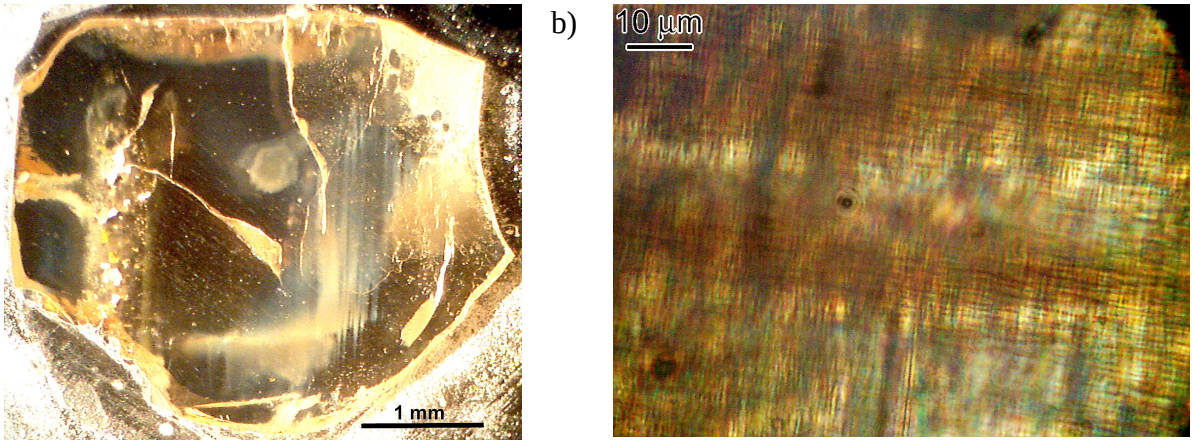

Figure 5.2. Optical images of (a) z0b6 single crystal; (b) one of its cloudy regions

A single crystal undoped NBT plate exhibited neighboring clear and opalescent regions (Fig. 5.3). By comparing two images of the same plate we can see that the opalescence is quite anisotropic. The origin of this anisotropic opalescence will be clear from the TEM images presented in the next part.

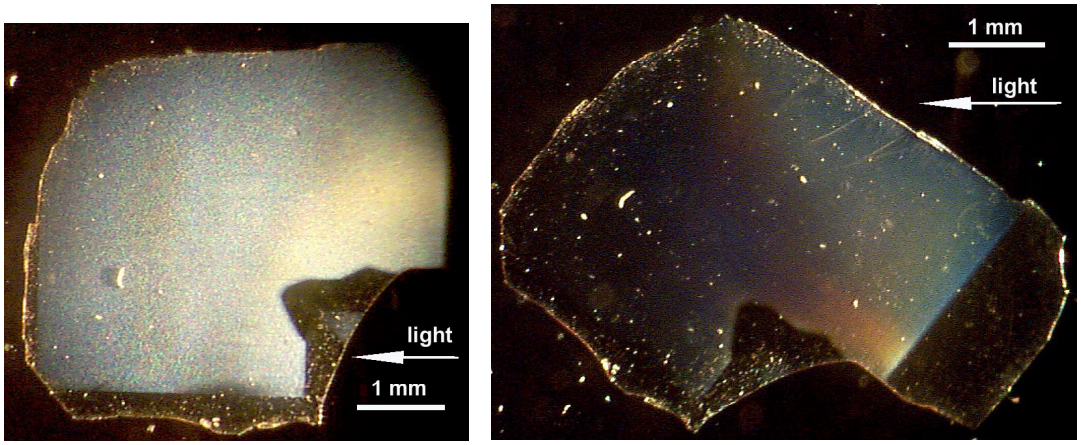

Figure 5.3. Optical images of two orientations of undoped NBT (001) plate with respect to incident light direction.

Another peculiar feature that has been observed in doped NBT single crystals is depolarization of polarized light. Fig. 5.4 presents three images of single crystal NBT doped with 3% Ba in cross polarized light at different angles of rotation. No extinction was observed in the clear top part of the plate at all angles of rotation. This indicates the presence of nano-scale inhomogeneities that are too small to scatter light but can retard the light beam by a randomly spatially distributed phase angle.

Figure 5.4. 3x3 mm z0b3 [110] oriented single crystal plate in cross-polarized light at different angles of rotation. Note the depolarization of light indicated by the absence of extinction.

The sample shown in Fig. 5.4 has a blue-looking layer, which is indistinguishable from the top part in ordinary transmitted light. The contrast appears only under a crossed polarized light due to the interference colors indicating presence of a complex pattern of residual stress. This complex pattern can be attributed to distortional frustration of the crystal: instead of forming a regular domain pattern the system is "frozen" in a state with randomly distributed distortion and stress. Apparent layered structure of this sample is a result of changing liquid composition during the flux growth. The structural features causing light depolarization without substantial scattering can only be seen using transmission electron microscopy. This is the subject of the next part.

Transmission Electron Microscopy

The cause of the anisotropic opalescence (Fig. 5.3) is easily seen on the transmission electron micrographs of the same sample (undoped NBT) presented on Fig. 5.5.

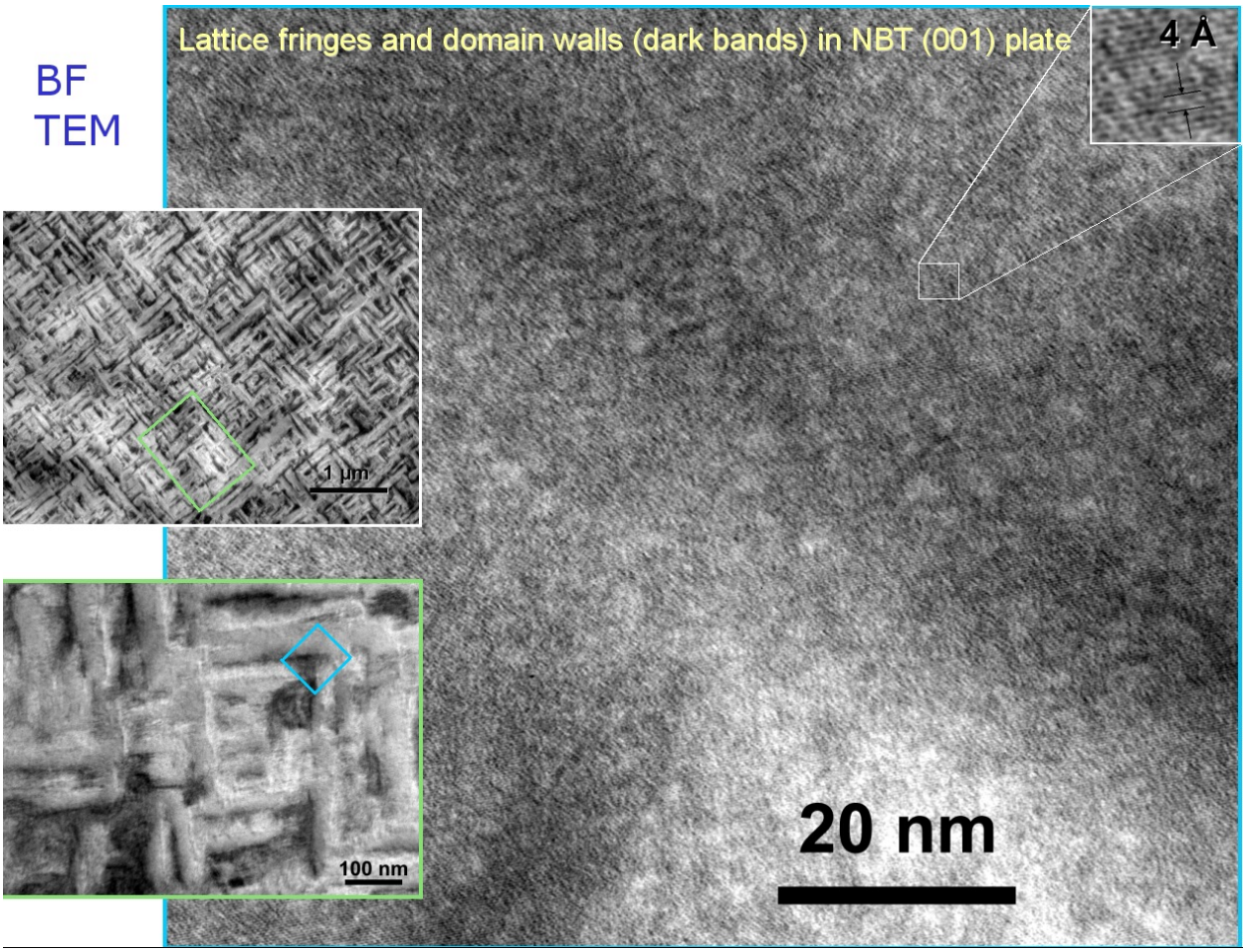

Figure 5.5. TEM bright field images of the domain pattern in NBT (001) oriented plate.

Small images on the left of Fig. 5.5 are low resolution images revealing highly textured but not periodic domain pattern. Note that the domains have varying thickness and that they intersect each other at right angle very often. The large image on Fig. 5.5 has an atomic resolution. From the large image we can see that the domain walls are very diffuse. Using HREM, from the mutual orientation of the lattice fringes and domain walls we determined that the domains were oriented along <110> directions.

Using a hot stage TEM we captured the thermal evolution of the domains in the same sample. It has been found to be gradual and reversible (Fig. 5.6). The temperature of appearance of domain during cooling is consistent with the temperature of appearance of the rhombohedral phase

identified by neutron diffraction [G.O. Jones and P.A. Thomas, *Acta Cryst.* **B58**, 168-178 (2002)]. We heated the sample up to 800°C. Surprisingly, we did not to see domains of the tetragonal phase that has been reported in the same paper to exist in the range of 400-500°C.

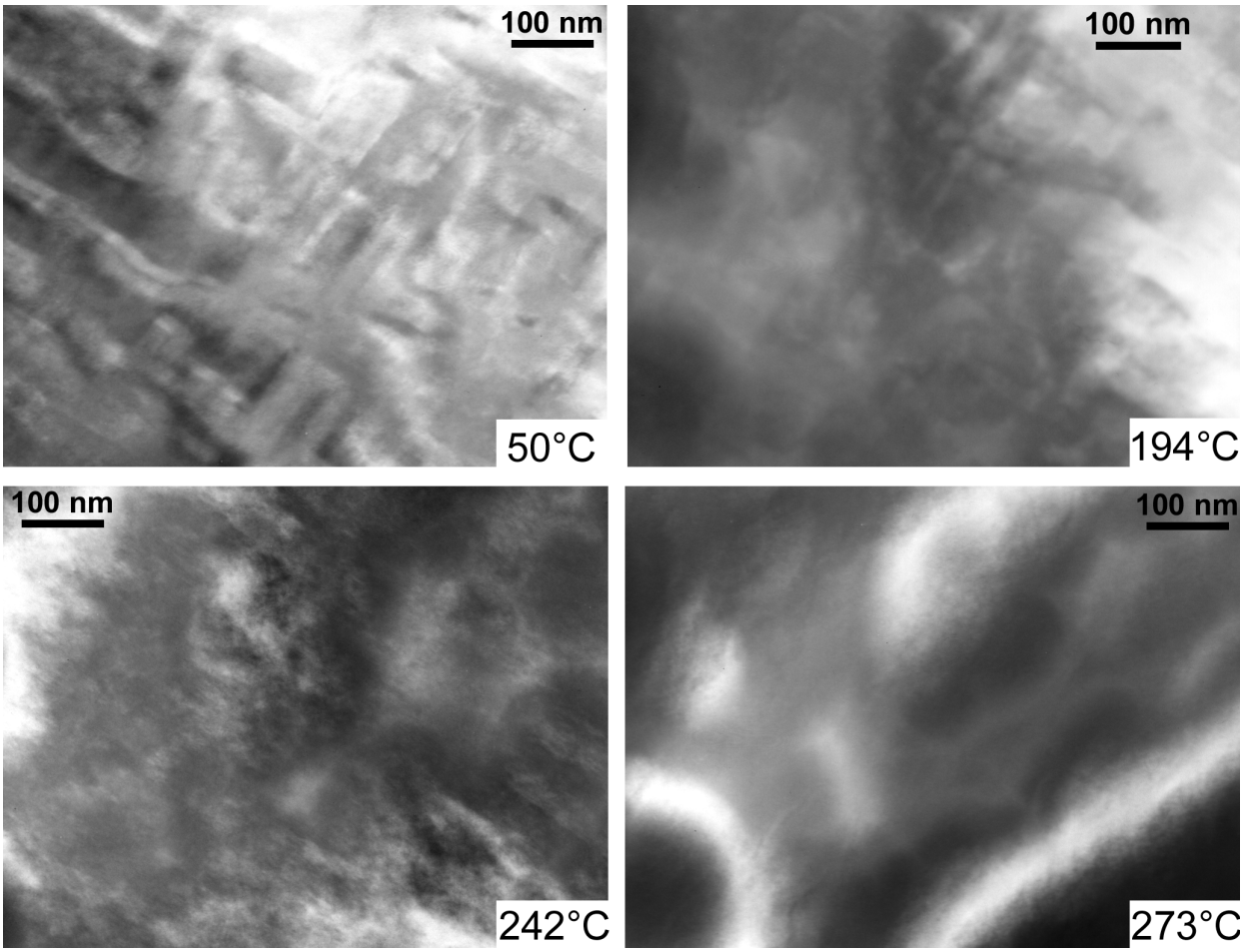

Figure 5.6. TEM bright field images of reversible thermoevolution of domains in NBT [001] oriented plate.

Besides undoped NBT, we performed hot stage TEM observations of [001] oriented single crystal plates of compositions z0b3 and z0b8. Neither optical not electron microscopy revealed any domain structure in these samples. Electron diffraction patterns of the three samples as a function of temperature are given in Fig. 5.7.

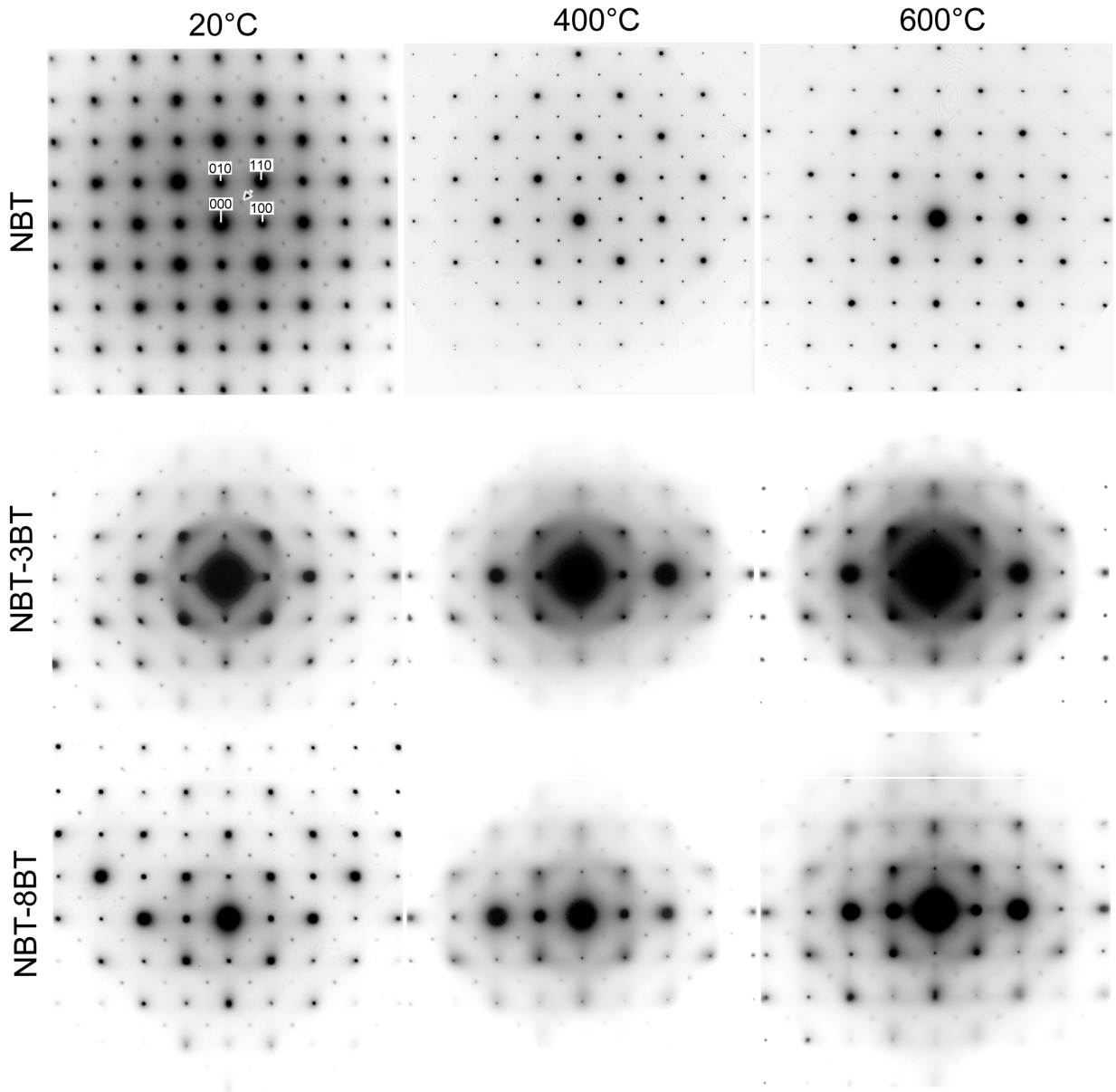

Figure 5.7. Electron diffraction patterns ([001] zone axis) in the range of Miller indices *h* and *k* from -4 to +4 for different compositions and temperatures. NBT – pure NBT, NBT-3BT – NBT doped with 3% BT, NBT-8BT – NBT doped with 8% BT. The arrow points to a superlattice reflection of (? ? 0) type

All patterns show superlattice reflections of (*h*+? *k*+? 0) type (indicated by the arrow in the first pattern). The intensity of these reflections varies with temperature: for NBT it reaches a strong maximum at ~400?C and almost completely vanishes by 700?C; for NBT-3BT and NBT-8BT samples it monotonically decreases on heating and by 400?C becomes very weak. The room

temperature intensity of the superlattice reflections increases with increasing BT content. The temperature dependence of the superlattice reflection intensity for NBT (maximum at 300-400°) resembles the behavior of the previously reported M_3 superlattice [S.B. Vakhrushev et al., *Ferroelectrics* **63** 153 (1985)]. However, in our case, forbidden for M_3 reflections (*h*+? *k*+? 0) appear on the diffractograms. We believe that these reflections are multiple scattering artifacts for the following two reasons: (1) they are weaker than the reflections, permitted for M_3 superlattice, e.g. (? ? 0) is weaker than (1? ? 0); (2) the samples were thick enough to produce substantial multiple scattering. The fact that superlattice reflections reappear instantaneously during cooling leaves no doubt that their origin is the octahedral tilt. In this experiment we have shown that octahedral tilt is present not only in undoped NBT, but also in Ba doped samples representing both sides of the rhombohedral-tetragonal MPB.

Careful observation of the large image in Fig. 5.5 leads one to notice “ripples” in the top center part having characteristic size of about 4 nm. These ripples are much more pronounced in the single crystal sample with highly nonstoichiometric composition $Na_{0.291}Bi_{0.445}Ba_{0.056}Ti_{1.065}O_3$ (EMPA data), which has shown the highest field induced strain ever reported for a lead free inorganic material—0.85 %. HREM image of this crystal is given in Fig. 5.8. Strong periodicity and anisotropy of the ripples is evidenced by the satellites around major spots on the Fourier transform of the HREM image (Fig. 5.8 bottom). The “ripples” are oriented along [001] and have an incommensurate with the lattice period of 3.4 nm. The Fourier transform also contains weak superlattice (? ? 0) spots caused by octahedral tilting. The structure of “ripples” is better revealed when we mask out the principal spots on the Fourier transform and transform back to produce direct space image (Fig. 5.9). Now we can see that the “ripples” have rather random shape and somewhat varying size. It is generally believed that incommensurate modulations occur as a result of competing lattice instabilities at the edge and at the center of the Brillouin zone [“Incommensurate phases in dielectrics” / ed. R. Blinc, A.P. Levanyuk, Elsevier (1986)]. In view of coexistence in a broad temperature interval of rhombohedral phase of NBT having parallel displacement of A- and B-cations with the tetragonal phase having antiparallel displacement of the same ions, it is not surprising that a soft mode can condense somewhere between the center and the edge of the Brillouin zone in a doped NBT.

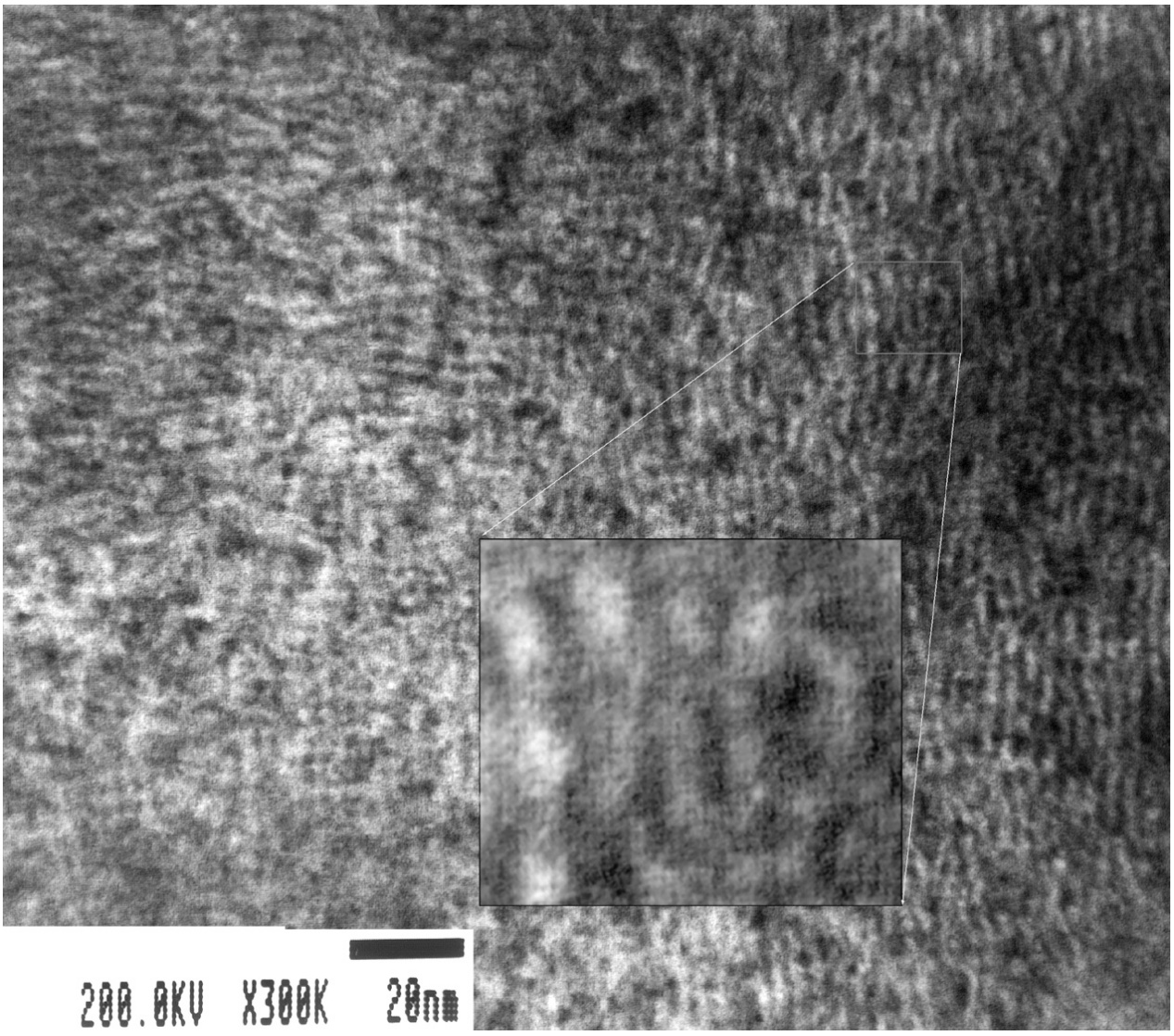

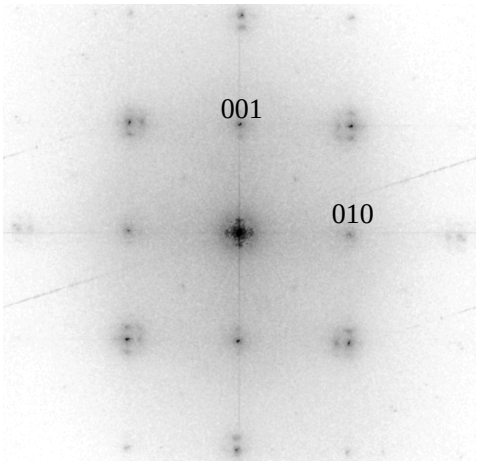

Figure 5.8. $Na_{0.291}Bi_{0.445}Ba_{0.056}Ti_{1.065}O_3$ Single crystal [001] oriented plate: TEM bright field image (top) and its Fourier transform

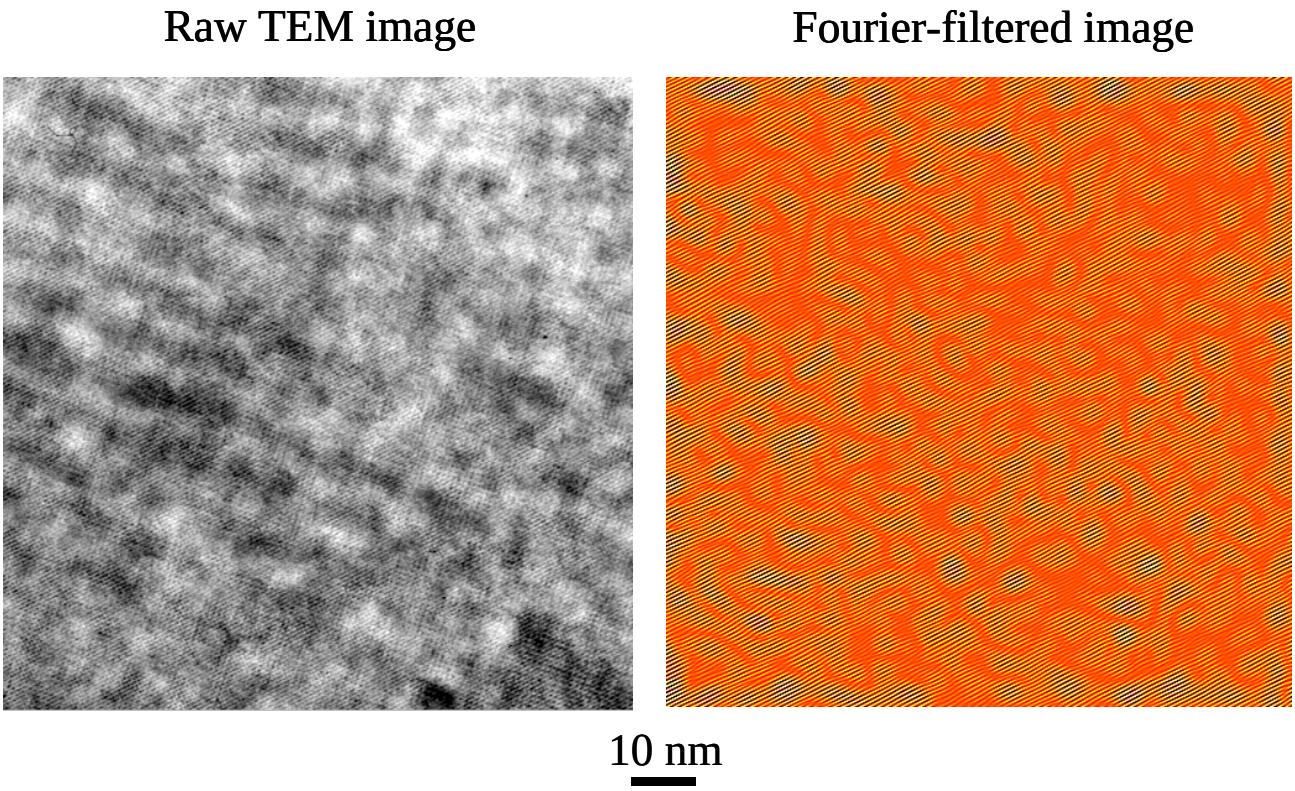

Figure 5.9. $Na_{0.291}Bi_{0.445}Ba_{0.056}Ti_{1.065}O_3$ Single crystal [001] oriented plate: TEM bright field image (left) and the same image with lattice fringes suppressed by Fourier filtering to enhance the contrast of nanoscale super-structure.

In any case, a distortional incommensurate modulation cannot correspond to a deep free energy minimum, therefore, the system must be highly susceptible to external forces, e.g. electric field. This can explain extremely high electric field induced strain exhibited by the nonstoichiometric crystal.

Finally, we performed TEM on a polycrystalline z3b6 sample (Fig. 5.10-11). [001] zone axis electron diffractograms clearly shows the presence of M_3 superlattice caused by $a^0a^0c^+$ tilt. No *Fm*3*m* cation ordering superlattice reflections are present. The direct space image shows a fairly complicated patchwork super-structure. The contrast of the latter is enhanced on the Fourier filtered image. It is hard to categorize this super-structure, but the nano-scale inhomegeneity is apparent. No larger scale structural features were detected in this sample. This fact makes the observed nano-domains the most plausible explanation of the relaxation of electric field induced polarization and strain.

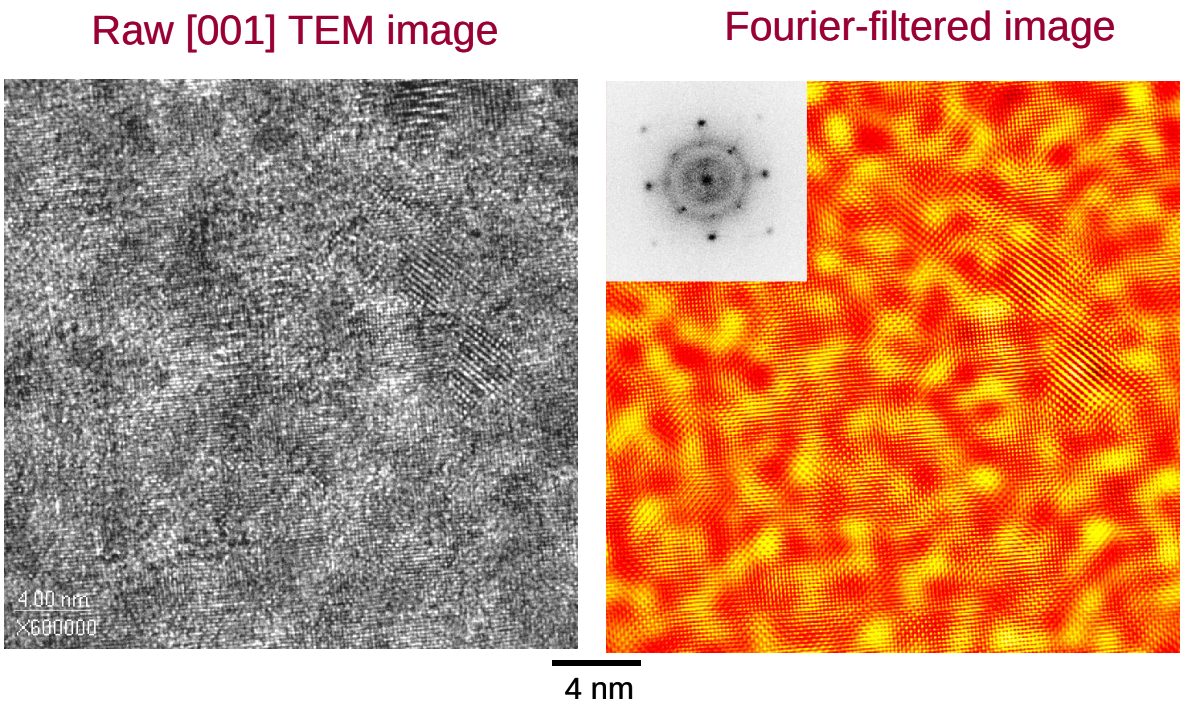

Figure 5.10. Polycrystal of NBT doped with 3% Zr and 6% Ba (z3b6): TEM [001] zone bright field image (left) and the same image with lattice fringes suppressed by Fourier filtering to enhance the contrast of nano-scale super-structure.

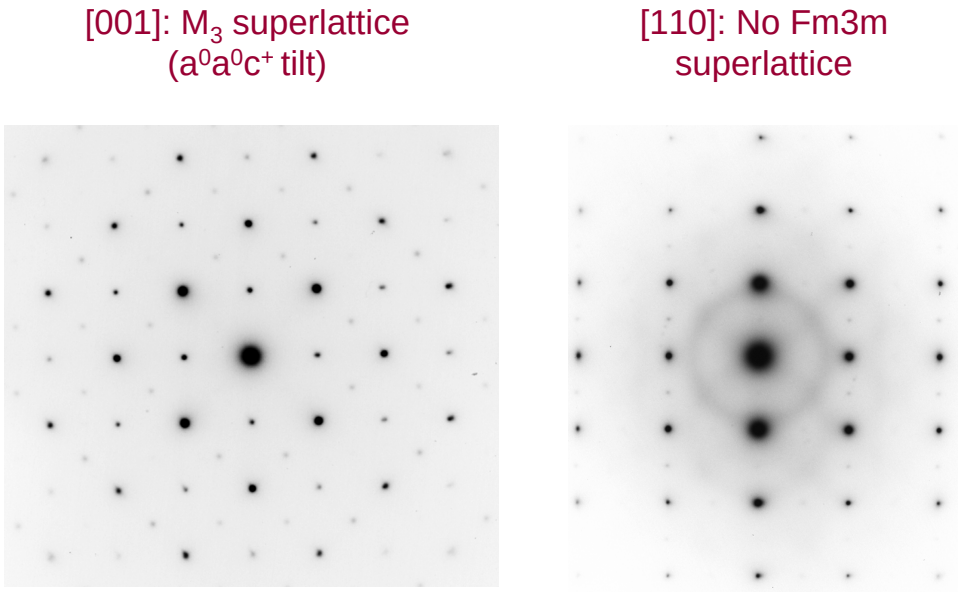

Figure 5.11. Polycrystal of NBT doped with 3% Zr and 6% Ba (z3b6): [001] zone (left) and [110] zone electron diffraction patterns. Note presense of tilt superlattice reflections and absence of cation ordering superlattice reflections.

Nanodomains and Relaxation

Let us know explain the connection between nanodomains and the time dependent electromechanical response. Fig. 5.12 illustrates the most general approach to the relaxation of domains from a metastable state to the stable state. The horizontal axis is an order parameter that characterizes the domain state, e.g. polarization for a ferroelectric domain.

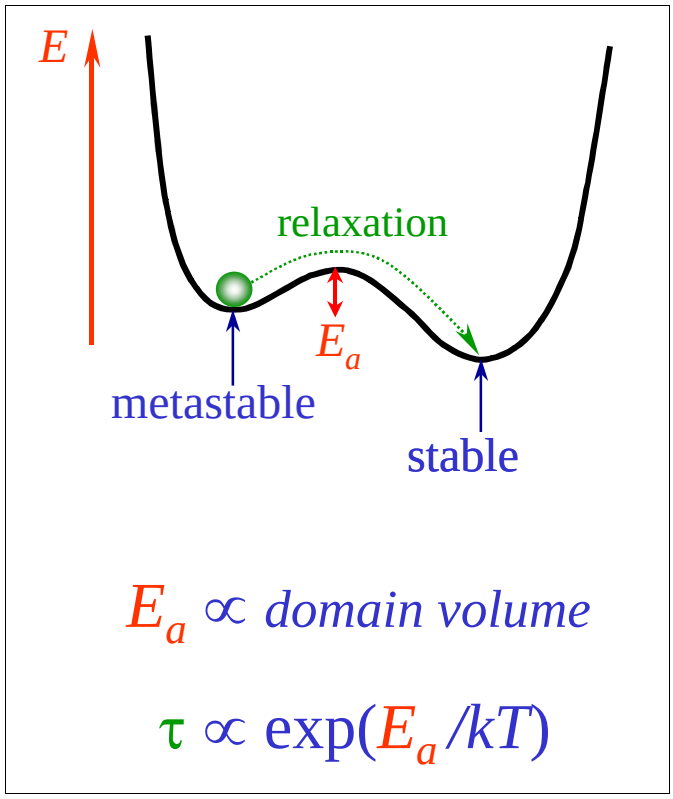

Figure 5.12. Schematic of the origin of domain relaxation. E_a is the activation energy (potential barrier height), τ is the relaxation time, a kinetic parameter in a rate of change equation

When, due to changes in external fields, a minimum energy configuration of a domain becomes a metastable one, the domain can overcome the barrier and switch to the stable state with the help of a large enough thermal fluctuation. The probability of such fluctuation is inversely proportional to the Boltzmann factor, therefore the relaxation time is proportional to the Boltzmann factor. The activation energy entering this factor is approximately proportional to the domain volume. In order for a relaxation to be observable the activation energy must be less than 30 k_BT (it is realistic to take the period of lattice vibration as the pre-exponential factor). This can be realized only for extremely small domains (few nm in size).

An ensemble of nanodomains behaves according to the laws of statistical mechanics with the only difference from molecular systems being much longer response time. When an external

field is absent, the ensemble average relaxes to zero to maximize entropy. When an external field is applied, the ensemble average starts to relax towards the value that minimizes the free energy of the system. If an external field changes fast enough, the ensemble average will lag the field with a certain phase shift depending on the field change rate. This lag looks like a hysteresis loop when we plot ensemble average vs. field.

Why do domains stay very small in relaxor ferroelectrics and do not grow similar to those of classical ferroelectrics? – Because the disordered cations of different charge inevitably create random fields inside the crystal. These random fields limit the domain size by their own scale. The long range interaction essential for the existence of macroscopic ferroelectric domains is disrupted by the fluctuations of local cation concentrations and corresponding local fields and stresses.

High strain actuation of relaxor ferroelectrics has a mechanism that is a hybrid of intrinsic and extrinsic electromechanical responses, which are clearly distinguishable in classical ferroelectrics. This mechanism combines high strain of extrinsic response with the absence of static hysteresis of intrinsic response. This combination has a down side too: higher dynamic hysteresis compared to intrinsic response. In this work, we have shown that in BNBZT system high electric field induced strain is coupled with high hysteresis.

CONCLUSIONS

This work has resulted in the following accomplishments.

1. High-field electromechanical behavior of polycrystalline samples in the Ba, Zr-codoped sodium bismuth titanate (BNBZT) system has been measured for a range of applied electric field frequencies (0.2-47 Hz).
2. A novel model of electromechanical response capable of describing both dynamic and static hysteresis for pure and mixed cases of ferroelectric, antiferroelectric, ferroelastic and paraelectric behavior has been developed.
3. Major electromechanical properties of polycrystalline BNBZT have been identified and compositionally mapped.
4. The peak of high-field piezoelectric strain coefficient has been found at the composition $(Bi_{1/2}Na_{1/2})_{0.93}Ba_{0.07}Zr_{0.02}Ti_{0.98}O_3$ (z2b7).
5. Compositional dependence of ferroelectric phase stability has been mapped by means of a Landau type free energy expansion.
6. Enhanced electromechanical response of BNBZT compositions close to morphotropic phase boundary has been explained by flattening of the free energy vs. polarization profile due to the distortional frustration of the system between rhombohedral and tetragonal symmetries.
7. Nanodomain relaxation mechanism of frequency dependent electromechanical response of BNBZT has been suggested and is supported by microscopic observations.

~